# VISUALIZING MEMBRANES

## 3D Electron Microscopic Imaging of Cellular Structures

Misjaël Nathanja Lebbink

*ISBN:* 987-90-393-5064-5

*Printed by:* ponsen & looijen b.v.

"Maak Mij indachtig, laat ons tezamen richten, spreek op, opdat gij in het gelijk gesteld moogt worden", יהוה door de profeet Jesaja *(Jesaja 43:26, NBG vertaling)*

The research described in this thesis was performed at Cellular Architecture & Dynamics, department of Biology, faculty of Science of Utrecht University. It was part of the Senter Novum IOP Genomics Project: *Electron Tomography, an indispensable step between Genomics and Cellular dynamics* (IGE03012).

# VISUALIZING MEMBRANES

## 3D Electron Microscopic Imaging of Cellular Structures

Visualiseren van Membranen
het 3D Elektronen Microscopisch Afbeelden van Cellulaire Structuren
(met een samenvatting in het Nederlands)

PROEFSCHRIFT

ter verkrijging van de graad van doctor aan de Universiteit Utrecht
op gezag van de rector magnificus, prof.dr. J.C. Stoof, ingevolge het
besluit van het college voor promoties in het openbaar te verdedigen op
dinsdag 9 juni 2009 des middags te 2.30 uur

door
Misjaël Nathanja Lebbink
geboren op 18 December 1977 te Arnhem

Promotor: Prof. dr. A.J. Verkleij
Co-promotor: Dr. J.A. Post

Dit proefschrift werd (mede) mogelijk gemaakt met financiële steun van:
*FEI Company, Eindhoven*
en
*de Stichting tot Bevordering van de Electronenmicroscopie in Nederland (SEN)*

Wetenschap – niet onderzoek - is een methode om op basis van objectieve waarnemingen de mechanismen van het universum te ontrafelen (niet meer en niet minder); en biologie is de wetenschap die zich bezig houdt met de mechanismen van het leven. Wat dit in werkelijkheid betekent, is, dat wetenschappers in de biologie proberen een puzzel op te lossen, waarvan niet alleen de plek, maar ook de vorm van de stukjes nog onbekend zijn. En om het allemaal nog een beetje extra interessant te houden, zijn alle stukjes dynamisch, kunnen de plek en de vorm van de stukjes continu veranderen, en lijken ze hierdoor soms niet binnen één plaatje te passen.

Om deze puzzel toch op te lossen hebben wetenschappers natuurlijk veel verschillende methoden tot hun beschikking, maar een van de meest fascinerende is – tenminste voor mij – toch wel elektronen microscopie: het bied je werkelijk de mogelijkheid om een reis door de wereld van de cel te maken. Je kunt zien wat er allemaal (op een stil gelegd moment) in de cel gebeurt. Je ziet dus hoe de puzzel er op dat moment echt uit zag.

Maar hoe mooi zo'n beeld van de cel ook is, als je wilt ontdekken hoe de puzzel opgebouwd is, kan het moeilijk zijn om de foto te interpreteren. Dit is een van de redenen waarom wetenschappers dan ook zo dol zijn op getallen: getallen stralen een vorm van zekerheid, een vorm van objectiviteit, een vorm van autoriteit uit. Je kunt je puzzel-stukje omschrijven in begrijpbare, hapklare brokken. Stel je spreekt over een toren van 112,32 meter hoog met een grondvlak van 19,30 bij 19,30 meter, dan is dit – als het je gaat om de grootte van deze toren – makkelijker en objectiever te interpreteren dan een foto van de Domtoren...zelfs al bevat die dezelfde informatie. Maar aan de andere kant mag ook niet vergeten worden, dat diezelfde foto van de Domtoren natuurlijk veel meer - en andere - waardevolle informatie bevat dan enkel deze drie getallen.

Een van de belangrijkste onderdelen van mijn project was dan ook om als bioloog - en vanuit vragen die wij biologen hebben – deze barrière tussen de steriele getallen en de subjectieve interpretatie van de foto te doorbreken, en interessante informatie op een objectieve(re) manier uit het plaatje te trekken. Nu lag de focus echter niet op het ontwikkelen van software hiervoor – ik ben bioloog en geen wiskundige, statisticus, of programmeur – maar om bestaande software vanuit een biologisch oogpunt toe te passen, en zo een meerwaarde uit de foto's te halen, die tot nu toe nog niet haalbaar was...niet de techniek-ontwikkeling, maar de toepassingen op vragen die biologen hebben bij het ontrafelen van de mechanismen van het leven staat centraal.

De belangrijkste toepassing binnen dit proefschrift is de mogelijkheid om een beter begrip te krijgen van de organisatie van de 'grens-muur' van de cel: het membraan. Deze muur is opgebouwd uit een zeep-achtig laagje, waarbinnen gebieden zitten met verschillende taken. Op sommige plekken moeten specifieke stoffen door de muur heen kunnen, en daar zitten dan eiwitten die als selectieve poorten werken. Op andere plekken zitten eiwitten het signalen opvangen van buiten (als een soort camera's op de muur), en dat signaal roept een bepaalde reactie op zowel bij de muur als dieper in de cel. Ook kunnen er detectoren in zitten, die bv in een bloedvat meten wat de bloeddruk is, of kan een bepaald stuk van de muur gestabiliseerd zijn met een stellage. Al deze verschillende taken maken dat de muur om de cel een sterk georganiseerd (maar ook weer dynamisch) geheel is. En het is dan natuurlijk ook niet vreemd, dat als er iets mis gaat in deze organisatie, dat dit dan grote gevolgen kan hebben voor het functioneren van de cel...en dat veel ziekten (waaronder diabetes, aderverkalking, en vormen van kanker) op een directe of indirecte manier te maken hebben met processen in deze muur – dit membraan – die niet, of niet correct verlopen.

Met het werk gepresenteerd in dit proefschrift probeer ik een (kleine) bijdrage te leveren aan de puzzel die biologen proberen op te lossen.

## Summary in English

Cells are organized in a highly complex manner. And while there are many different types of cells - each organized in a different manner according to their function - they do share certain commonalities. Among these commonalities are membranes that function not only as a barrier between the extra- and intra-cellular environment , but are also involved in many cell-biological processes like signalling and transport; and since each of these processes require a different set of components and organization, a large heterogeneity is expected within these membranes.

Electron microscopic techniques have been invaluable to our understanding of the complex cellular architecture (and the corresponding dynamics). In recent years, 3D electron microscopic techniques like electron tomography and the focussed ion-beam scanning electron microscope have emerged and provided us with an exciting new perspective of cellular structures and their inter- and intra-organellar relationships.

However, extracting relevant information from (3D) micrographs heavily relies on manual segmentation techniques and is therefore affected by the eye of the beholder. In the work presented in this thesis we have explored template matching as an approach to harvest biologically relevant information from tomographic volumes in a (semi-)objective manner. By using a stylized cuboid-shaped template we could extract membranes from the tomographic volumes and thus study the overall morphology of organelles. But more importantly, by comparing the matching results of slightly distinct templates, we were able to visualize ultra-structural details that are lost by manual segmentation.

By applying this approach we up the ante of electron tomographic approaches and were able to bring it into a new realm where we can study and visualize in three dimensions the membrane-organization of biologically functional and significant events like lipid- and protein-domains.

## Samenvatting in het Nederlands

Cellen hebben een heel complexe organisatie. Maar terwijl er veel verschillende type cellen zijn - welke allemaal net anders georganiseerd zijn - delen ze ook bepaalde overeenkomsten. Een van die overeenkomsten zijn membranen die niet alleen functioneren als een grens tussen de wereld binnen en buiten de cel, maar die ook betrokken zijn bij veel biologische processen, zoals het doorgeven van signalen, of het transporteren van stoffen. Omdat al deze processen een verschillende set van componenten en organisatie nodig hebben kan men een grote variëteit verwachten binnen deze membranen.

Elektronen microscopische technieken zijn bijzonder waardevol gebleken om beter te begrijpen hoe de complexe cellulaire architectuur (en de daar aan gekoppelde dynamiek) in elkaar zit. In de laatste jaren zijn nieuwe drie-dimensionale elektronen microscopische technieken ontwikkeld die ons een nieuw en boeiend beeld geven op cellulaire structuren en hun relaties tot andere structuren in de cel.

Echter, de relevante informatie wordt op dit ogenblik nog veelvuldig met de hand uit een elektronen microscopische opname gehaald, waardoor het beïnvloed wordt door de kennis en ervaring van de wetenschapper. In het werk dat in dit proefschrift gepresenteerd is, hebben we de mogelijkheid onderzocht om een techniek genaamd 'template matching' (sjabloon herkenning) te gebruiken om biologisch relevante informatie te 'oogsten' uit deze 3D volumes (tomogrammen) op een (semi-)objectieve manier. Door een stilistische representatie te gebruiken konden we membranen in het tomogram automatisch intekenen om zo de globale vorm van cel-compartimenten te bestuderen. Maar belangrijker nog, door verschillende sjablonen te gebruiken die een klein beetje van elkaar verschilden, waren we in staat om ultra-structurele details weer te geven, wat handmatig niet mogelijk is.

Op deze manier hebben we 3D elektronen microscopie naar een nieuw niveau gebracht, waar we het membraan ultra-structureel kunnen bestuderen.

# table of contents

# CHAPTER I

## introduction on biomembranes and visualization techniques

# introduction on biomembranes and visualization techniques

The constant dilemma of the information age is that our ability to gather a sea of data greatly exceeds the tools and techniques available to sort,extract, and apply the information we've collected.

*Jeff Davidson*

In 1665, the scientist Robert Hooke coined the term 'cells' to describe the structural building-blocks that he microscopically observed in the organization of cork. The term 'cell' is a reference to the chambers of monks, that bore similarity to these structures according to Hooke. But despite the name, a fundamental biological concept came into existence that day. A little over a decade later - in 1676 - Antoni van Leeuwenhoek was the first to see living microorganisms by means of an (for that time) enhanced light microscope. Now, 333 years later, we're still on a voyage of discovery in this fascinating world of the cell. We're still using microscopes to get a glimpse of all the marvels in that world. And it is still as captivating and enchanting as it was the first time men set foot in it.

The central theme in this thesis is the biological membrane, which is investigated within its cellular context by means of three-dimensional electron microscopy using either the focussed ion beam-scanning electron microscope (FIB-SEM), or Electron Tomography. I will present my work - as a cell-biologist - to enhance the visualization of the organization of membranous structures. The biological question that steered these developments was to unravel processes involved in the development and early stages of atherosclerosis; as part of the IOP genomics project electron tomography, an indispensable step between Genomics and Cellular dynamics *(IGE03012)*. During the formation of the atherosclerotic plague, the barrier function of the endothelial cell layer covering the blood vessel-wall is compromised, and one of the goals within this project was to uncover the nature of this malfunction, to identify which alterations in the cellular membranes were involved, and to develop tools to enhance the visualization of biomembranes in general.

## 1.1 Biomembranes

Biomembranes are complex structures that play a vital role in the organization and function of cells. In the first half of this chapter I will go into a number of key-concepts that play a fundamental role in my research. These concepts are presented within their historical context, to provide not only an overview of membranes, but also how our understanding of them came to be. This understanding of the membrane has been shaped by a variety of the techniques; but visual approaches - and especially electron microscopic techniques - have always had a special relationship with cell- and membrane-biology.

In 1839 - about 175 years after Hooke coined the term cell *(Hooke, 1665)* - Schleiden and Schwann proposed one of the most fundamental 'laws' in biology: the cell theory. They proposed a hypothesis stating that (1) the cell is the unit of structure, physiology, and organization in living things, (2) the cell retains a dual existence as a distinct entity and as a building block in the construction of organisms, and (3) cells form by (an intracellular variant of) generatio spontanae; similar to the formation of crystals. The latter of their ideas has been proven to be incorrect; and as early as the 1850's Virchow corrected the view of Schleiden and Schwann by proposing the hypothesis that every cell is derived from a (preexisting) cell *(omnis cellula e cellula)* *(Mazzarello, 1999)*. This adapted cell-theory still stands unchallenged today. There are a number of implications of the cell theory, which affect various fields of biology that I won't go into in this thesis. However, there is one point that I do want to stretch: the first rule of the cell theory places a specific role in the hands of cells: all life is contained within cells, and outside of cells there is no life. This implies - by definition - that a barrier must exist that keeps the extracellular and intracellular environment from mixing in order to maintain life. This barrier is called the (plasma) membrane.

One of the primary observations that stood at the basis of our understanding of the organization and operation of the membrane was by Overton in 1895 who was the first to notice that lipids were the general building-blocks of the barrier between the extra- and the intra-cellular environment *(Robertson, 1981; Overton, 1991)*. With the basic building-blocks - and some of their physical properties - known, the question arose as to whether these membranes were organized as a mono- or double-layer of

lipids. In 1925 Gorter and Grendel performed a classic experiment that would provide the answer this question. Their rationale was, that if one independently measured the surface of a large quantity of cells (that have a relatively homogeneous size) and the surface covered by a monolayer of lipids extracted from the plasma membrane of the same number of cells, the ratio between these two would provide a clear answer. They discovered that the monolayer of lipids covered about double the surface of the cell, and therefore concluded that the plasma membrane was bilayered; a conclusion that has since been found to be true *(Gorter & Grendel, 1925; Singer, 2004)*.

This bilayered organization was the foundation of the sandwich model which Davson and Danielli proposed in 1935 *(Danielli & Davson, 1935)* and which was adapted in 1959 into the Davson-Danielli-Robertson model after the first electron microscopic observations made by Robertson on thin sections *(Robertson, 1959, 1981)*. Within this model, the lipid-backbone of the membrane is arranged in such a way that the hydrophobic lipid-tails face each other, while the hydrophilic head-groups face the extramembranous environment. In addition, this lipid-bilayer was covered and stabilized by a coat of proteins layering the polar lipid-heads (figure 1.1). When biomembranes are stained with uranyl and lead salts, they appear as characteristic 'railway-tracks' under the electron microscope, where a clear core lies between two dense strata (figure 1.2). Robertson correlated this observation to the physical and chemical properties to the membrane components: the core represents the hydrophobic groups (the lipid-tails), and heavy metals are not taken up strongly by this layer. In contrast, the outer strata consist of the polar lipid-heads and proteins that are hydrophilic and take up the stain avidly *(Robertson, 1981)*.

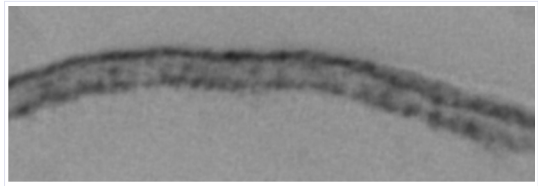

**Figure 1.2. Appearance of the stained bilayered membrane in an electron micrograph.** *The characteristic appearance of biomembranes stained with uranyl and lead salts under the electron microscope - where an electron sparse core lies between two dense strata - is related to the physical and chemical properties of the membrane components: the hydrophobic tail-groups of the lipid are less heavily stained than the hydrophilic lipid-heads.*

The Davson-Danielli-Robertson membrane model provided many correct ideas and functional hypotheses; however additional observations seemed in disagreement with the model. One of the major observations that disagreed with the model was made was by means of the electron microscopical technique of freeze-fracturing, where it was found

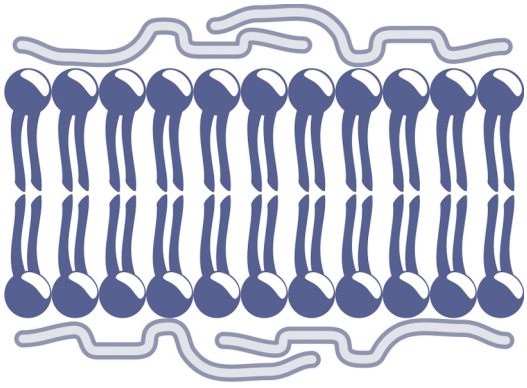

**Figure 1.1. The Davson-Danielli-Robertson sandwich-model of the bilayered membrane.** *Lipids are organized in a bilayered fashion with hydrophobic tails directed towards each other, and the hydrophilic head-groups pointed outwards. Lipids are sandwiched between two layers of stabilizing protein-coats.*

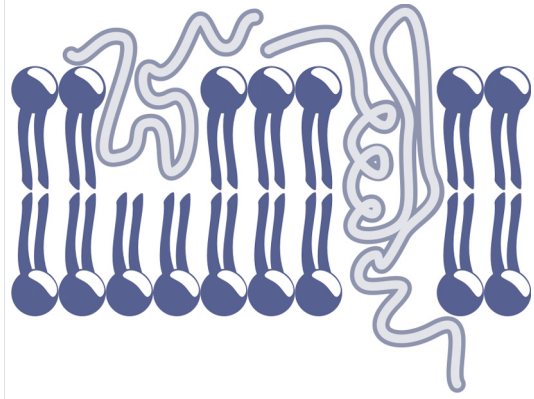

**Figure 1.3. The Fluid-Mosaic membrane model of Singer and Nicolson.** *Lipids are organized in a bilayered fashion with hydrophobic tails directed towards each other, and the hydrophilic head-groups pointed outwards. In addition, proteins attach, penetrate, and span the bilayer.*

that a substantial amount of proteins associated with the membrane were embedded within the lipid-bilayer. These observations were the basis for the fluid-mosaic model proposed by Singer and Nicholson in 1972 *(Singer & Nicolson, 1972)*. The fluid-mosaic model tried to bring a number of observations and concepts together and presented a model that - like the Davson-Danielli model - had a bilayered lipid-membrane as its backbone. However, unlike the existing model, proteins anchor, penetrate, and even span the bilayer (figure 1.3). Spanning of the bilayer, and the alphahelical nature of such proteins was later shown by means of electron diffraction *(Henderson & Unwin, 1975)*. Another important characteristic property of the model is, that the lipid bilayer is highly dynamic (as opposed to the previous model which is far more rigid); allowing 'free' movement of lipids and proteins within this layer.

Fluidity and dynamics have since become major concepts in membrane biology. It should, however, be noted, that the free-floating aspect of the fluid-mosaic model does not imply that a biomembrane is an unorganized soup of lipids and proteins; the opposite is true. The chemical and physical properties of the membrane components result in a high degree of organization that is affected by changes in the chemical or physical environment. Freeze fracture has revealed, for example, that - due to the diversity of lipids in biomembranes - upon changes in temperature, pH, or the concentration of divalent cations, lipids of similar solidification properties cluster together into domains; a phenomenon called lipid phase separation *(Verkleij et al., 1972; Verkleij & Ververgaert, 1975)*.

Our understanding of the complexity of membrane organization in biological systems advanced another step, when, in 1973, Verkleij et al. found that the inner- and outer-leaflet of the bilayered plasma membrane were asymmetrical: certain lipids are predominately (or exclusively) in one layer, while others are present in both *(Verkleij et al., 1973; Post et al., 1995; Verkleij & Post, 2000)*. Additional studies revealed that lipid phase separation can also occur within a single lipid-leaflet *(Post et al., 1995)*.

Domain-formation is not controlled by environmental factors alone; the chemical and physical properties of lipids, cholesterol, and proteins themselves also form the basis for 'capturing' certain membrane components into biologically functional domains and clusters such as bacteriorhodopsin, cell-junctions, and protein coats *(Mouritsen & Bloom, 1984; Simons & van Meer, 1988; Bretscher & Munro, 1993; London & Brown, 2000)*. Most of these domains - with the exceptions of protein coats *(Munro, 1995)* - are not easily visible by conventional transmission

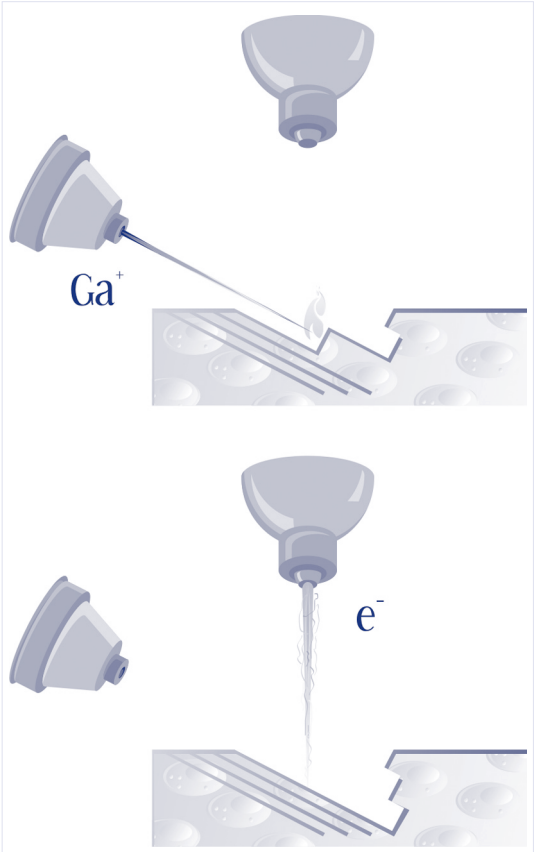


**Figure 1.4. General overview of the FIB-SEM method to acquire a three-dimensional representation of a structure.** *By shooting gallium-ions at the sample, the focussed ion beam (FIB) can be used to mill away a small (or large) stratum from the surface of a sample. The new surface that is revealed can subsequently be imaged by a scanning electron microscope (SEM). By repeating this process several times, the same structure is imaged at multiple depths thus providing its three-dimensional architecture. A three-dimensional model can be obtained by tracing the structure of interest in every slice.*

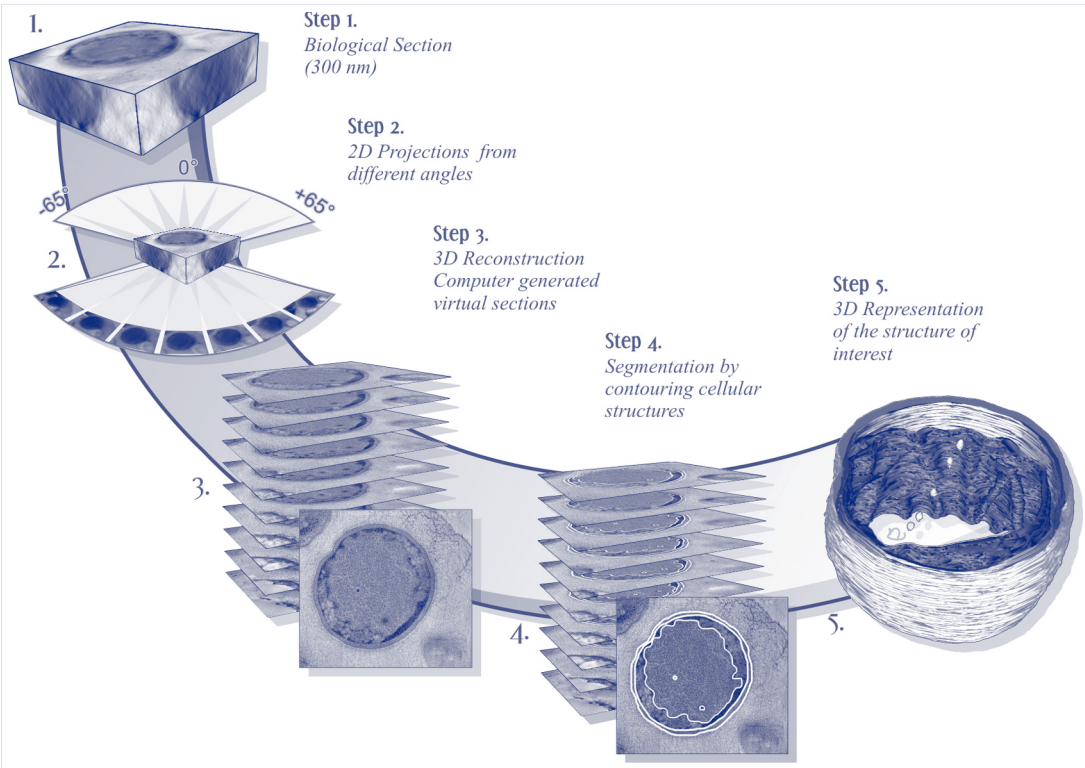


**Figure 1.5. General overview of the electron tomographic method to acquire a three-dimensional representation of a structure.** *Electron tomography in cell biology is a five-step process: (1) a semi-thick specimen of approximately 300 nm is placed within an electron microscope, and micrographs are obtained over a range of multiple angles (2), these two-dimensional projections are mathematically combined into a single three-dimensional model (3). To highlight the structure of interest the volume is annotated (4), and a three-dimensional representation of the structure is created (5).* *Scheme created for and used with permission of Laura van Niftrik.*

electron microscopy on sections; although antibodies against specific components can be used for localization studies. One of the goals of the research presented in this thesis was to overcome this limitation and to visualize the organization of membrane domains by means of three-dimensional electron microscopy without the need for additional processing-steps prior to the acquisition of the image.

## 1.2 Connections and Continuity

One of the major questions in cell biology concerns the inter-relationships between membrane compartments. Cellular organization and function are tightly regulated and closely intertwined. Conventional electron microscopy has always been - and still is - a valuable tool for exploring cellular morphology and organization. However, connections and continuities between cellular components and organelles are rarely captured within a single two-dimensional plane and to investigate these - or many other localized biological events - an additional dimension is often required.

Throughout this thesis two three-dimensional (3D) electron microscopic techniques have been applied that have arisen relatively recent, and which use an entirely different approach in obtaining a three-dimensional representation of the structure of interest. The FIB-SEM uses the 'direct' approach by combining a focussed ion beam (FIB) with a scanning electron microscope (SEM) *(Inkson et al., 2001; Kubis et al., 2004)*. At a relatively low magnification, the SEM mode can be used to navigate large areas of a sample, and zoom in on the area of interest. The FIB can than subsequently be used to mill away a small

stratum from the surface - ranging from tens of cubic nanometres to thousands of cubic micrometers - and thus reveal a new surface. By obtaining images of each of the new surfaces, the three-dimensional cellular architecture of the specimen can be acquired (figure 1.4). Consequently, the FIB-SEM - in biology - can be particularly valuable for unravelling the three-dimensional organization of structures within a large field of view. However, when a cell-biological question asks for a higher resolution, like for example when membrane connections and continuities are to be studied, the indirect approach for obtaining a three-dimensional volume by electron tomography is particularly useful.

Electron tomographic sections - as used in this thesis - are approximately 300 nm thick and covered with small non-specific gold beads (of five or ten nanometre in diameter). These beads are visible in the micrograph as electron dense dots, that are used as fiducial markers that mark the same spot in 3D-space throughout the acquired tomographic tilt-series. In electron tomography, a series of micrographs is taken from a set of different angles; which thus contain slightly different perspectives of the 3D structure and relationship of the section's content. It is therefore possible to combine the additional information of each of these images, and mathematically reconstruct the 3D position of the section's content; thereby creating a 3D volume (figure 1.5). Based on the three-dimensional relationship of the fiducial markers, it is possible to determine the 3D-position of each pixel (or its density) in the series; thus reconstructing a three-dimensional image/volume of the original structure acquired *(De Rosier & Klug, 1968; Gilbert, 1972; Koster et al., 1997)*. Throughout this thesis, the weighted back-projections algorithm as implemented in the Imod-package was used *(Kremer et al., 1996)*. This use of fiducial markers - of course - implies that if its centre is not correctly localized in every micrograph of the tilt-series, their 3D-position is slightly off, thus resulting in a 'slightly off' back-projected tomogram. Common artefacts caused by incorrect 3D-spacing of the fiducial markers are displacements and shadowing of objects; the majority of biological research is, however, not hampered by a small degree of such artefacts (as long as only details are blurred and not the overall volume). Another artefact in electron tomography is the missing wedge *(Koster et al., 1997; McEwen & Heagle, 1998)*. The missing wedge is caused by a technical limitation of the apparatus and sample-thickness, whereby the limit of angles at which micrographs are taken is limited from -70 to +70 degrees. As a result, forty degrees that contain additional and unique information about the three-dimensional relationship of structures within the sample are not taken into account in the reconstruction resulting is a direction-dependant blur. When a perpendicular tilt-series of the same sample is created, it can be combined with the original tomogram to significantly reduce this artefact

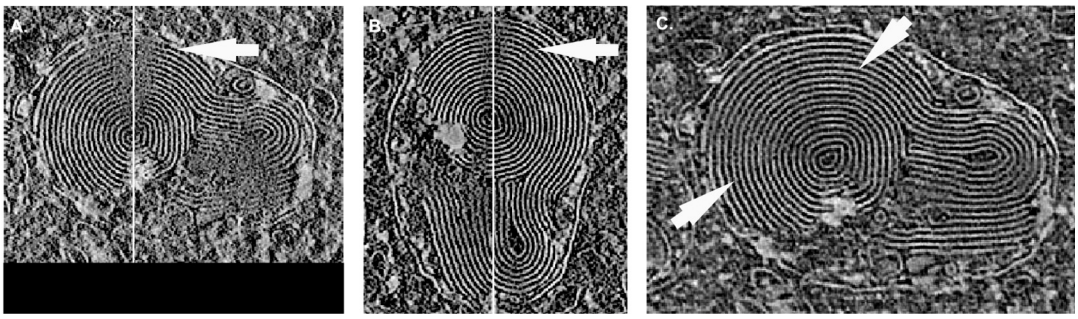


**Figure 1.6. Double-tilted reconstructions improve the three-dimensional tomographic reconstruction of biological specimens.** *A tomographic reconstruction was made from two perpendicular tilt-series of the same multilaminar lysosome (A and B). The white lines in panel A and B indicate the axis of rotation. Perpendicular to the axis of rotation resolution is lost due to the missing wedge, which is visible in the tomographic volume as a direction specific blurring of the structure (indicated by the arrows). By combining both tilt-series into a single double-tilted tomogram, such artefacts are significantly reduced, and the reconstruction is greatly improved (C). Image courtesy of JLAN Murk (Murk, 2004)*

(figure 1.6). The resulting tomogram is referred to as a double tilt tomogram *(Penczek et al., 1995; Mastronarde, 1997; Arslan et al., 2006)*.

Even though electron tomography - like all electron microscopic techniques - provides a snapshot of a cellular event, it has in recent years provided many new insights into the cellular architecture and dynamics *(Murk et al., 2004; Marsh et al., 2005)*. As an example the idea that organelles are static and isolated compartments has been challenged by three-dimensional electron microscopic findings *(Mannella et al., 1998; Gueze et al., 2003; Marsh et al., 2004; Trucco et al., 2004)*.

## 1.3 Template Matching

One of the huge limitations of electron tomography derived three-dimensional models of cellular organelles has always been of a subjective nature: membranes are traced manually in each tomographic slice to produce a 3D representation of the organelle. The disadvantage of this is, that certain tracing decisions are in the eye of the beholder; some connections or continuities are difficult to interpret, and the value of the corresponding model may be largely affected by the experience of the investigator. This does of course not imply that all manually segmented tomographic models are of little to no value to the scientific community, but it has always been one of the major matters of concern when such a model provides evidence for a novel idea. Therefore there is a need for more objective manners of interpretation of electron tomographic data. In the remainder of this chapter I will address the basic ideas of three-dimensional template matching for annotation of biological structures; an approach to increase objectivity in the analysis of electron tomograms. The technique plays a prominent role is the majority of chapters in this thesis. I will not explore the technique - as developed in the group of Wolfgang Baumeister *(Böhm et al., 2000; Frangakis et al., 2002)* - from a mathematics's or programmer's point of view, but rather from the point of its application within a biological question. We applied this methodology on samples that were prepared under (currently available) optimal conditions for these samples and our biological questions (high-pressure freezing and freeze substitution for cultured cells, and chemical fixation for tissue). In addition, our templates were defined based on the visual appearance of structures within their cellular context as observed in the tomographic volume, rather than by crystallography or single-particle analysis.

## 1.4 When the Shoe Fits

To me, the best allegory to explain what template matching is all about is the story of Cinderella: when the prince finds Cinderella's slipper, he has a template that helps him identify the girl of his dreams. So using this template he tries to match is to every (left) foot of every girl in the country until he finds Cinderella, swoops her of her feet, and carries her off to his castle. In the case of template matching, each location of the tomographic volume is compared to the small three-dimensional object described within the template file. Depending on the statistical similarity between the tomogram and the template, a correlation-value is assigned that is continuous and lies between zero (not likely to be the same) and one (most likely to be the same). This is an important notion, which has several implications throughout this thesis.

When localizing a specific structure you prefer the algorithm to provide a boolean result of true or false; does the shoe fit or not? - To convert a continuous value into a boolean value, a threshold is used: if the likelihood of similarity is lower than a given value it is regarded as false (the shoe does not fit this foot), and if the likelihood is above the given value it is regarded as true (the shoe may very well fit). If this value is set too low, false positives will be included (and you might end up with the angry stepsister), or false negatives may be caused (where you missed Cinderella altogether, because here foot had swolen up a little). This threshold-value is set subjectively to include as many of the objects of interest while excluding as much of the background as possible. When multiple templates containing variations of the same structure are compared to each other, the threshold-value is decided upon for the whole series, and not for the individual calculations.

However, by converting a continuous distribution to a boolean distribution, information is lost. In some chapters of this thesis, when only a single template is investigated, this loss of information does not have a great impact. However, in later chapters, when the matching values of multiple templates are related to each other, using a boolean distribution over a continuous distribution would render the investigation impossible: imagine you have two glass slippers, and the first belongs to Cinderella, while the second is the angry stepsister's. Now if both girls exceed the threshold value for both slippers, then it is impossible to define which slipper belongs to whom...and this is hardly the best ending of the fairytale. In this case categorical data would be required: the question is changed from 'which slipper fits' to 'which slipper fits better', and the assumption is made that the shoe that fits better belongs to the girl in question. This comparison is achieved by means of a maximum operation: the matching values of both calculations are compared, and for each location (where the threshold is exceeded in either calculation) the template with the best fit (that is having the highest correlation value) is regarded to describe the structure most likely present at that location. This results in the following categories: (0) the structure described in either template is not likely to be present at this location, (1) the structure described in the first template is most likely to be present here, or (2) the structure described in the second template is most likely to be present here. It is obvious that the number of categories is derived from the number of templates.

## 1.5 Aim and Outine

In this thesis I present my work on enhancing the visualization of membranous biological structures within their cellular context by three-dimensional electron microscopy, and approaches to automate this visualization process, make the annotation of electron tomographic volumes more objective, as well as to extract additional information from tomographic volumes beyond the capacity of conventional manual annotation.

Many cell-biological questions concern intra- and inter-cellular relationships of a biological system. It is known, that organization and function are closely intertwined, and even the slightest disruption of the organization can have major implications for the function of a cell, organ, or organism. However, to observe and identify such a disruption can require the analysis of a large area within a biological sample. In chapter two we investigate the FIB-SEM as an approach to study both the cellular and the multi-cellular organization at an electron microscopic level in three dimensions, and take a first look at the kind of biological questions that can either benefit highly from this approach, or are impossible to investigate by any other.

As described throughout this introduction, electron microscopy has had a great impact on our understanding of the organization of biological membranes, and electron tomography has granted us a three-dimensional view of membranous compartments within the cell. Electron tomography has been particularly valuable for the investigation of connections and continuities between these compartments, and provided new insights into cellular organization. One of the major limitations of electron tomography is though, that it relies on manual annotation. In chapter three and four we present the semi-objective approach of template matching to annotate membranes acquired by means of two different electron tomographic techniques to provide the basis for an objective analysis of electron tomographic data.

Membrane dynamics, fluidity, and domain formation, are major characteristics of the fluid-mosaic model by Singer and Nicolson. It has been observed by a variety of techniques, but has also been beyond the reach of electron tomography. In chapter 5 we induce lipid-phase separation - a well defined dynamic property of mixed lipid-membranes - in the *Escherichia coli* outer membrane to seize the challenge to localize and visualize membrane domains in three dimensions by electron tomography in combination with template matching. The combination of these techniques provide a robust approach to investigate existing cell-biological questions in a new dimension.

Besides lipid domains, there are many biologically functional protein domains that play a role in the structure, organization, and function of biomembranes. In chapter six we take yet another step that raises the bar for electron tomographic studies in cell- and membrane-biological questions: template matching provides a tool to localize and visualize membrane attached protein-coats, and presents us with the opportunity to investigate the protein-coat organization on these membrane-structures.

Throughout this thesis we present - in small but relevant steps - three-dimensional electron microscopical approaches to investigate cell- and membrane-biological questions within their cellular context from a micrometre to a nanometre scale.

# CHAPTER II

# FIB-SEM: an in-depth study of atherosclerotic tissue

# FIB-SEM: an in-depth study of atherosclerotic tissue

L.H.P. Hekking • M.N. Lebbink • D.A.M. de Winter • C.T.W.M. Schneijdenberg
C.M. Brand • B.M. Humbel • A.J. Verkleij • J.A. Post

*Cellular Architecture and Dynamics, University of Utrecht, the Netherlands*

Drama is life with the dull bits cut out.
*Alfred Hitchcock*

Submitted in revised form

Atherogenesis is a pathological condition in which changes in the (ultra)structure and in the localisation of proteins take place within the vasculature during all stages of the disease. To gain insight in those changes, high resolution imaging is necessary. However, some of these changes will only be present in a small number of cells, positioned in a "sea" of non-affected cells. To localize this relatively small number of cells there is a need to first navigate through a large area of the sample and subsequently zoom in onto the area of interest; a process called "correlative microscopy". This approach also enables the study of specific cells within their in vivo environment, and enables the study of (possible) interactions of these cells with their surrounding cells/environment. The study of a sample in a correlative way using light and electron microscope is a promising approach to achieve this, however, it is very laborious and additional ultrastructural techniques might be very valuable to find the places of interest.

In this report we show that the focussed ion beam-scanning electron microscope is a powerful tool to study biological specimen in a correlative way. With this microscope one can scan for the area of interest at low magnification, in this case the atherosclerotic plaque, and subsequently zoom in, for further analysis on an ultrastructural level; rendering valuable and detailed 2D and 3D information of, in this case, the endothelial cells and the vessel wall. Moreover, in combination with pre-embedment labelling of surface exposed antigens, the method allows insight into the 3D distribution of these (bio)markers.

## 2.1 Introduction

In the Western society, cardiovascular diseases, amongst which atherosclerosis, are the leading causes of mortality and morbidity. A disturbed laminar blood flow, hypercholesterolemia and provoked inflammation contribute to atherogenesis at plaque prone areas. Lipid lowering diets and anti-inflammatory therapies will thicken the fibrous cap by inducing the migration and proliferation of smooth muscle cells and triggering the synthesis of extra cellular matrix synthesis. However, as inflammation persists in the plaque the collagenous matrix will be degraded and new collagen synthesis by smooth muscle cells is inhibited, resulting in a so called vulnerable plaque. The vulnerable plaque is a lipid filled plaque with a thin fibrous cap; these plaques are prone to rupture and are responsible for fatal acute thrombosis *(Libby, 2002)*.

To gain further insight in (sub)cellular changes during atherogenesis, and thereby in the pathogenesis of atherosclerosis, the cellular architecture of plaques and healthy regions of arteries need to be studied in greater detail. To be able to navigate to the areas(s) of interest and subsequently zoom in onto this area to detect, for instance, minor morphological changes or changes in protein localisation and/or expression in specific cell types, high resolution imaging is a necessity. This limits the use of the light microscope and can only be achieved by electron microscopic techniques. However, conventional transmission electron microscope (TEM) is not very well suitable to locate areas of interest in a biological sample. Therefore, in cellular studies correlative microscopy is often used to locate regions of interest at relative low magnification with the light microscope combined with ultrastructural analysis and protein localisation using the electron microscope. Although correlative microscopy protocols have been optimized *(Oorschot et al., 2002; Schwartz et al., 2007; Van Driel et al., 2008; Verkade, 2008; Wilke et al., 2008)* and new probes have been developed *(Giepmans, 2008)*, which can be detected both in the fluorescent microscope and in the electron microscope, it is still very laborious. Furthermore, acquiring 3D information will be even more tedious, if possible at all. Therefore new approaches have to be explored to meet these needs.

Such a new approach might be the Integrated Light Electron Microscope (ILEM), recently described and developed in our group *(Agronskaia et al., 2008; Karreman et al., 12009)*. In addition the Focused Ion Beam – Scanning Electron Microscope (FIB-SEM) might be a suitable microscope to study biological samples in a correlative way. This microscope has been mostly used on non-biological samples, although recently the FIB-SEM has also been used to study biological samples *(Heymann et al., 2006; Knott et al., 2008; De Winter*

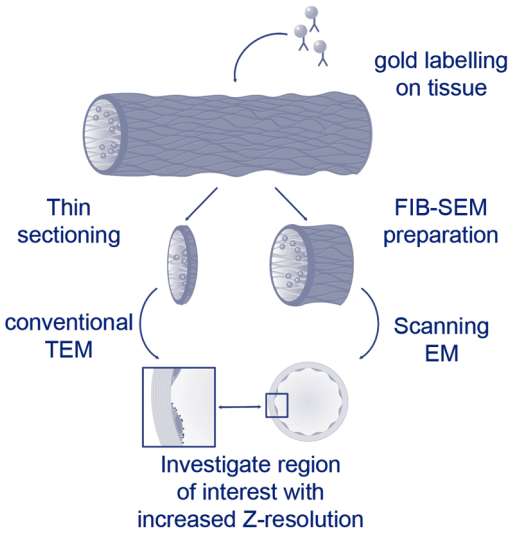


**Figure 2.1. Schematic representation of the followed approach:** *pieces of arteries obtained from ApoE-/- mice were, after being fixed, immunogold-labelled for ICAM-1. The tissue was embedded in Epon and thin sections were prepared. The remaining sample was used for FIB-SEM examination. Conventional TEM was used to examine the thin sections and compared with the micrographs obtained with the FIB-SEM.*

*et al., 2009]*. The FIB-SEM combines a scanning electron microscope with a focused ion beam. At relative low magnifications the SEM mode can be used to study/image a large area of the sample. In addition, in scanning mode we can navigate to and zoom in onto the areas of interest. The FIB can subsequently be used to remove small volumes of material, a process called milling or sputtering, ranging from tens of cubic nanometer up to thousands of cubic micrometers at the areas of interest. The sidewalls of the milled trenches reveal a cross section of the sample and can be visualized in the SEM mode, thereby acquiring 3D information of the (cellular) architecture of the specimen.

To identify the area of interest one can either use morphological markers and/or specific (bio)markers. In the case of atherosclerosis the gross morphology of the plaque might serve as a navigation landmark. Identification and visualisation of different stages of atherogenesis might be achieved by means of specific (bio)markers, which then will be helpful to identify the areas of interest in the artery. For instance, CD81, a tetraspanin family member, was recently shown to be upregulated in endothelium overlying early atheroma and thus can be used to recognize early events of atherogenesis *[Rohlena et al., 2008]*. Another family of proteins that is involved in the atherogenic process, and which might be applied for navigating to the area of interest, is the Cell Adhesion Molecules, of which ICAM is an example *[Libby, 2002]*.

We explored the possibilities of the FIB-SEM to study the (3D) ultrastructure of the atherosclerotic plaque and to visualize the distribution of an endothelial cell surface expressed protein involved in this process. After location of the areas of interest, three different approaches were used to zoom in and visualize the endothelium, the underlying tissue, and the surface exposed protein, at nanoscale resolution. In this report we show that the FIB-SEM is a valuable and straightforward approach to gain insight in the cell biology of the atherosclerotic plaque at high resolution in vascular tissue.

## 2.2 Material and Methods

ApoE deficient mice (kindly provided by dr Th J C van Berkel) were maintained on a chow diet for 10-15 months and subsequently anaesthetised and perfusion fixed with 4% formaldehyde (FA) in PHEM buffer (60 mM Pipes, 25 mM HEPES, 2 mM $MgCl_2$ and 10 mM EGTA). Animal work was approved by the regulatory authority of Leiden University and performed in compliance with the Dutch government guidelines.

Aortas were dissected after the fixation. Some of the aortas were directly postfixed with 2% $OsO_4$ and 1.5% $K_4Fe(CN)_6$ for 2 hours at 4°C, dehydrated through a series of ethanol and embedded in Epon; whereas others were pre-embedment labelled with an anti-mouse ICAM-1 (MALA-2 (clone YN1/1.7; Takei), a kind gift from Prof. Mebius). For detection of ICAM-1 a bridging antibody was used (Rabbit anti Rat; Dako) and protein A gold 10 nm (UMC, Utrecht, the Netherlands). After labelling, the tissue was fixed with a mixture of 2% FA, 2.5% glutaraldehyde (GA), 0.025%

$CaCl_2 \cdot 2H_2O$, 0.05% $MgCl_2 \cdot 6H_2O$ and 0.1M Na-cacodylate pH 7.4 (adapted from Karnovsky) and treated as described above.

In order to compare the images obtained with the FIB-SEM to conventional TEM, ultra-thin sections (60 nm) were cut prior to using the embedded artery for FIB-SEM examination (figure 2.1). The sections were stained in an over-saturated solution of uranyl acetate in 70% methanol with Reynold's lead citrate and examined using a Technai 12 (FEI, Eindhoven, the Netherlands) at 80 kV.

After sectioning the embedded artery was cut with a glass knife into a small block and the surrounding Epon was largely removed to reduce the risk of charging. The sample was glued on a stub with carbon paint, giving special attention to the electrical connectivity between the stub and the osmicated artery. Subsequently a Pt/Pd coating of 3 nm was applied using a sputter coating (Cressington, HQ280). The sample was then transferred to the FEI Nova Nanolab600 Dualbeam™ (FEI, Eindhoven, the Netherlands). To protect the area of interest from the ion beam and to prevent curtaining, a local Pt-layer with a thickness of about 1 micron was deposited in-situ on top of the Epon block. Subsequently the cross section was milled at 0 degrees stage tilt, with the ion beam coming in at 52 degrees to the sample *(De Winter et al., 2009)*. This prevents contrast gradients, shadowing and focus differences in the y-direction when tilted towards the electron beam. The milling starts with a coarse milling step with a large current (20 nA), followed by a polishing step with a smaller current (0.1 nA-1 nA) called a cleaning cross section. The cross sections were imaged in back scatter electron (BSE) mode using a 2 kV beam (0.21 nA).

The stack of SEM images created in the FIB-SEM were combined into a single 3D volume using the Amira software package (Mercury, France) and subsequently converted (into an .MRC file) and manually aligned using the tools available in the IMOD package *(Kremer et al., 1996)*. Thereafter a three dimensional representation was created by manually tracing the structures of interest in Amira.

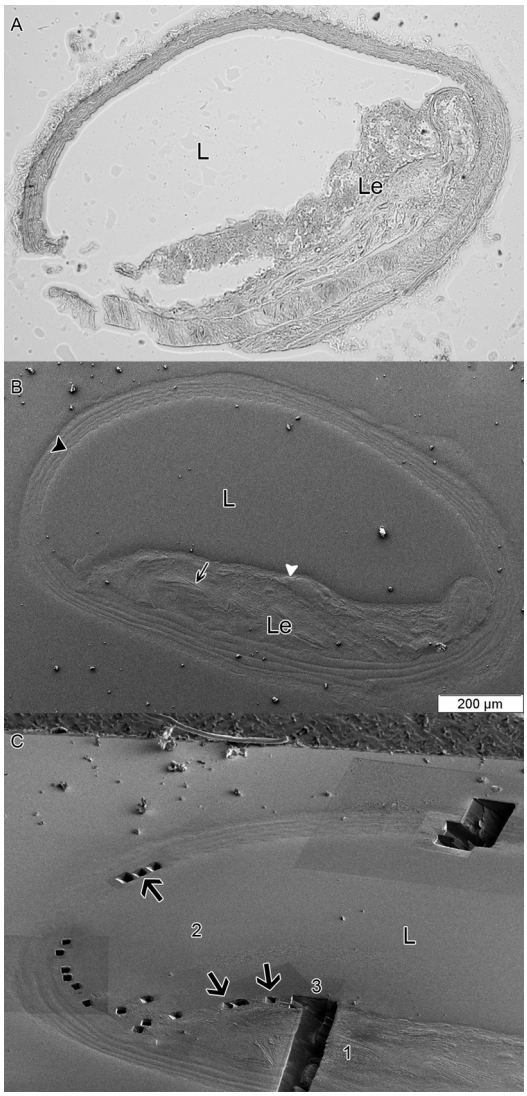


**Figure 2.2. FIB-SEM examination of atherosclerotic tissue of ApoE-/- mice.** *A Overview of the artery as observed in light microscope. The lumen of the artery is depicted with "L" and the plaque with "Le". B. Overview of the artery as observed in scanning mode. The white arrowhead indicates at lipid filled cells; the black arrowhead points at the elastic lamina; the black arrow points at calcified material. Le=plaque. C. Overview of the three different approaches to study the artery. The numbers correspond to the approach used. Approach 1: milling a large cross section; approach 2: milling several small cross sections; approach 3: a slice and view series. The black arrows in figure C indicate the locations of the sections imaged for figure 2.4.*

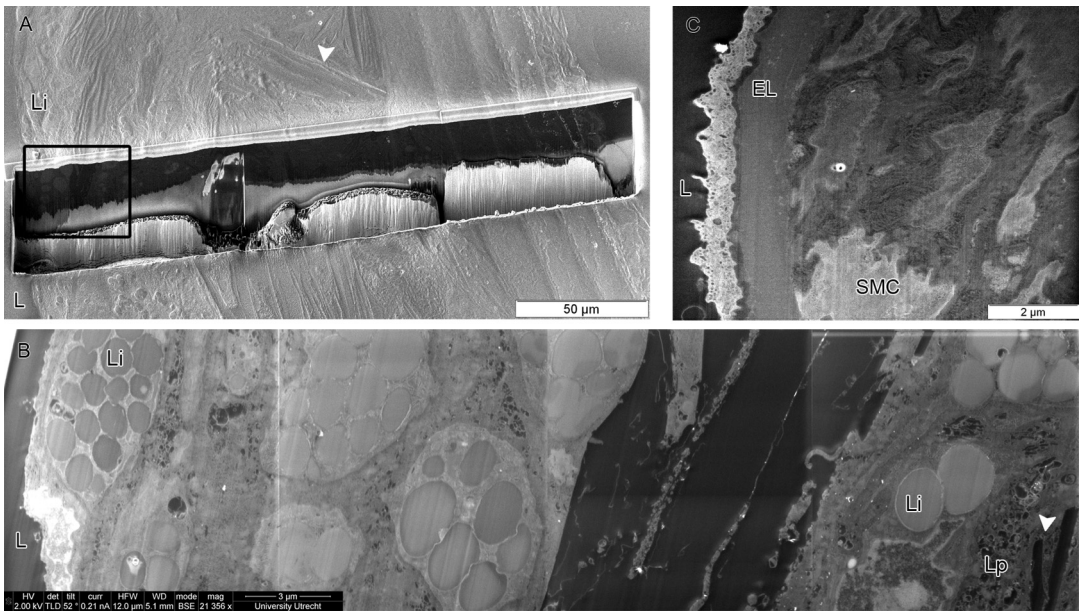


**Figure 2.3. Approach 1.** *A. High magnification of the large cross section, shown in figure 2.2.C, through the plaque area. The black box indicates the area of which the panorama in figure 2.3.C is imaged. B and C. Panorama of multiple high resolution images of the plaque area (B) and the healthy area (C) taken of the large cross sections shown in figure 2.2.C. The white arrow head indicates cholesterol needles; L=lumen; Li=lipid; Lp=lipoprotein particles; EL=elastic lamina; SMC=smooth muscle cell.*

## 2.3 Results

To be able to study the atherosclerotic plaque in a correlative way the most straightforward approach is to image a cross section of the complete artery, and to use morphological landmarks to identify the location of the plaque areas at low magnification and then zoom in onto the areas of interest. Using the light microscope the initial imaging can be performed rather easy, however, so far the preparation methods limit the success of subsequent high resolution analysis at the same area. Since with light microscopy it is possible to image a cross section of a complete mouse artery (figure 2.2.A) we wondered whether we could visualize the plaque areas also with the FIB-SEM. The advantage of this microscope is that one can image at relative low magnification large areas of the sample and zoom in onto areas of interest using the ion beam.

To test the feasibility of this approach and to validate whether the resolution obtained with the FIB-SEM is comparable to conventional TEM, arteries of ApoE-/- mice were embedded in Epon. The surface of the Epon block was smoothed by cutting ultrathin (60 nm) sections. Figure 2.2.B shows a SEM micrograph obtained in the FIB-SEM of the artery at low magnification. Indeed the complete artery can be imaged, and the plaque and healthy areas of the artery are clearly distinguishable. In this cross section through the vessel wall, lipid loaded cells (white arrowhead) and calcified cholesterol crystals (black arrow) are observed in the plaque area. The elastic lamina is visible throughout the entire vessel wall.

To study the areas of interest at higher resolution three different approaches were used to obtain information on (1) the vessel wall composition/morphology going from the lumen to outside of the vessel wall; (2) the endothelial lining of the vessel at different sites of the vessel lumen and (3) the 3D morphology at the site of the plaque (all three approaches are shown in figure 2.2.C). The first approach (figure 2.2.C[1] and figure 2.3) was to investigate the morphology of the vessel wall by milling a large area cross section through the

plaque (approximately 242 µm length; figure 2.3.A) and through a healthy area (approximately 50 µm length; figure 2.3.C). Starting at the lumen, when migrating into the plaque, an endothelial cell, overlying a lipid loaded cell, is imaged. The nucleus of the endothelial cell is clearly visible; for further detailed morphological information the cells have to be studied at higher magnification, as shown later. The lipid loaded cell represents a foam cell, which arises when macrophages scavenge Low Density Lipoprotein (LDL) particles accumulated in the extra cellular matrix of the vessel wall [Libby, 2002]. In the foam cells underneath the endothelial cell, multi lamellar structures and large lipid droplets (figure 2.3.B) are present. Between the foam cells, accumulated lipoprotein particles (Lp) can be recognized. Furthermore, calcified cholesterol needles (white arrowheads) are present in the matrix between the foam cells. No elastic lamina was observed in the approximately 50 µm we imaged of the plaque, indicating a large increase in volume of the area of the vessel wall between the elastic lamina and the lumen. In contrast, when migrating into the healthy areas, the endothelial cells are located on a basal lamina, over the elastic lamina, which is clearly visible in

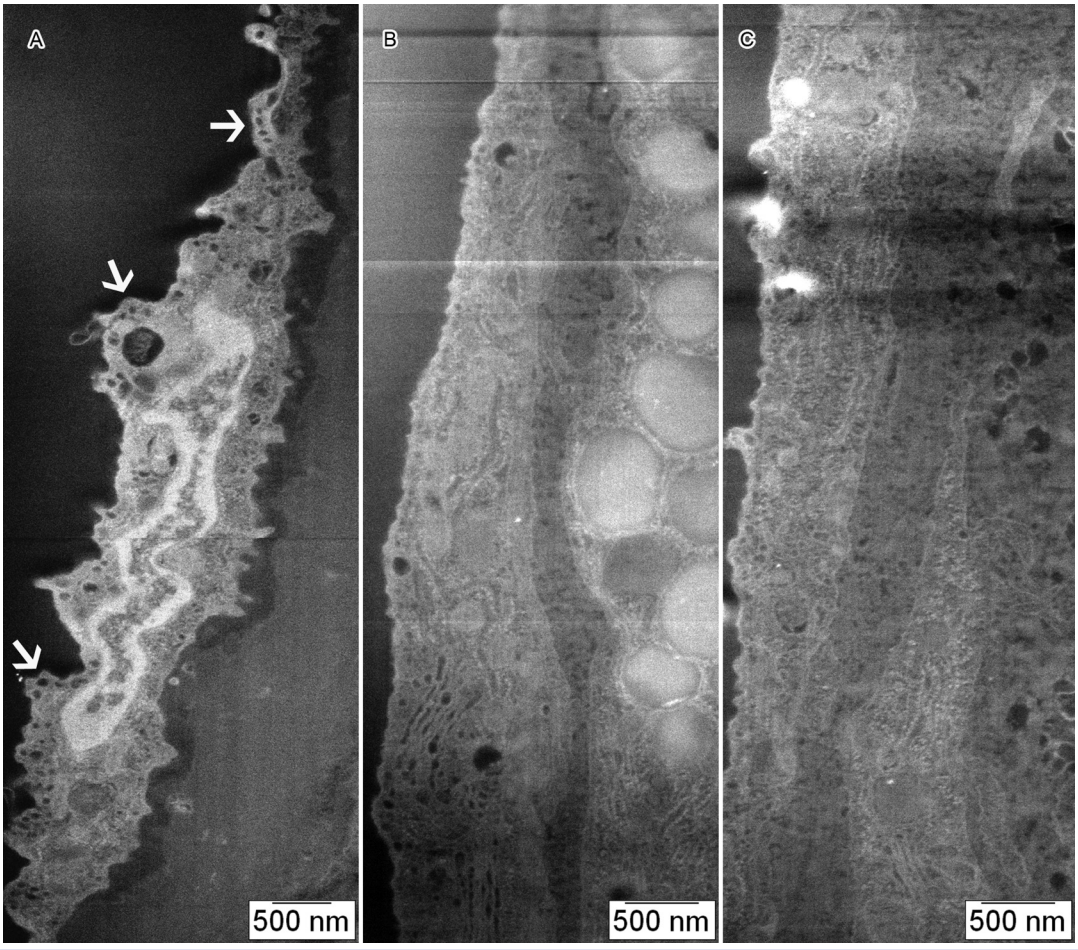


**Figure 2.4. Approach 2.** *BSE images taken from small local cross sections in a healthy (A) and a plaque region (B and C). The cross sections are indicated in figure 2.2C by black arrows. In the image of the healthy regions, the elastic lamina is clearly visible underneath the endothelial cells, whereas underneath the endothelial cell located on the plaque a lipid filled cell (B) and accumulated lipoprotein particles (C) are observed. Multiple caveolae structures are observed in the endothelial cells located in the healthy region, indicated by the white arrows.*

figure 2.3.C. Underneath the elastic lamina, collagen vessels and smooth muscle cells are present. No lipoprotein particles or lipid loaded cells can be observed. Using this approach the tissue can be screened for the presence of a plaque. The plaque itself can be screened for the presence of specific morphological parameters, such as collagen bundles, cholesterol crystals or foam cells, to give a first indication about the nature and state of the plaque.

The second approach was to do a rapid investigation of large areas by milling a number of small local cross sections (figure 2.4.A-C); giving a representative picture of a location. Figure 2.2.C[2] shows a low magnification image of the areas investigated, indicated by the white arrows. Using this approach, we milled at 12 different locations cross sections of the endothelial cells to compare the morphology of these cells located on the plaque and at the healthy regions of the artery. Again, underneath the endothelial cells at the healthy regions an elastic lamina was recognized (figure 2.4.A). Foam cells and accumulated lipoproteins were present underneath the plaque endothelial cells (figure 2.4.B and 2.4.C), as also described above. Furthermore, at these higher magnifications differences seemed to be present in the caveolar system: the plaque endothelial cells appeared to contain less surface bound caveolae compared to healthy endothelial cells. This difference might be of interest in view of endothelial cell function and is currently under further investigation. So with this approach one can study ultrastructural changes in cells/tissue of interest in relation to the location within the vessel wall.

Both approaches show that the resolution obtained with the FIB-SEM is sufficient to visualize membranes, as is shown in figure 2.3 and 2.4. However, a clear lipid bilayer, which can be imaged using the same sample preparation methods and conventional TEM (see for instance figure 2.6.E), is not observed in the micrographs, implying a slightly less X-Y resolution when using the FIB-SEM.

To gain insight in the 3D configuration of the plaque and to study whether we could visualize various membrane compartments, approach 3 was performing a slice and view™ (FEI, Eindhoven,

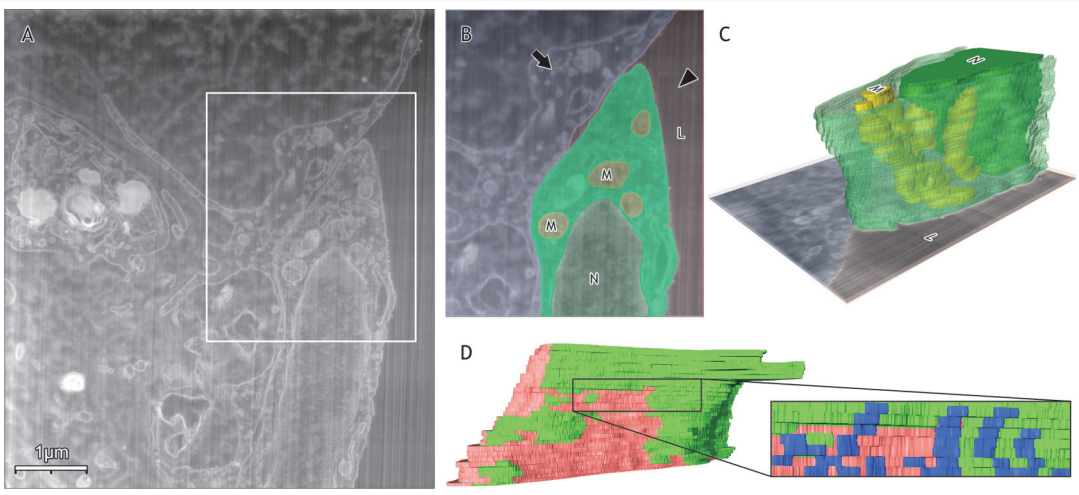


**Figure 2.5. Approach 3.** *3D reconstruction of a slice and view series made from the plaque endothelial cells towards the shoulder of the plaque. A. a slice of the series showing two endothelial cells overlying a plaque. The area indicated with the box was manually annotated in every slide as indicated in B. Figure C shows a three dimensional reconstruction of part of the endothelial cell. The 3D organization of the mitochondria (yellow/M) and nucleus (green/N) can be clearly investigated using this approach. D. Cell-cell contact is visualized in 3D. Contact points of the cells are shown in green, while pink indicates where the neighbouring cells do not make contact. In a small area of the membrane (D, right panel), caveolar invaginations are indicated in blue. L=lumen of the blood-vessel; N=nucleus; M=mitochondria. The arrowhead and the arrow indicate the camera-positions for figure C and D respectively.*

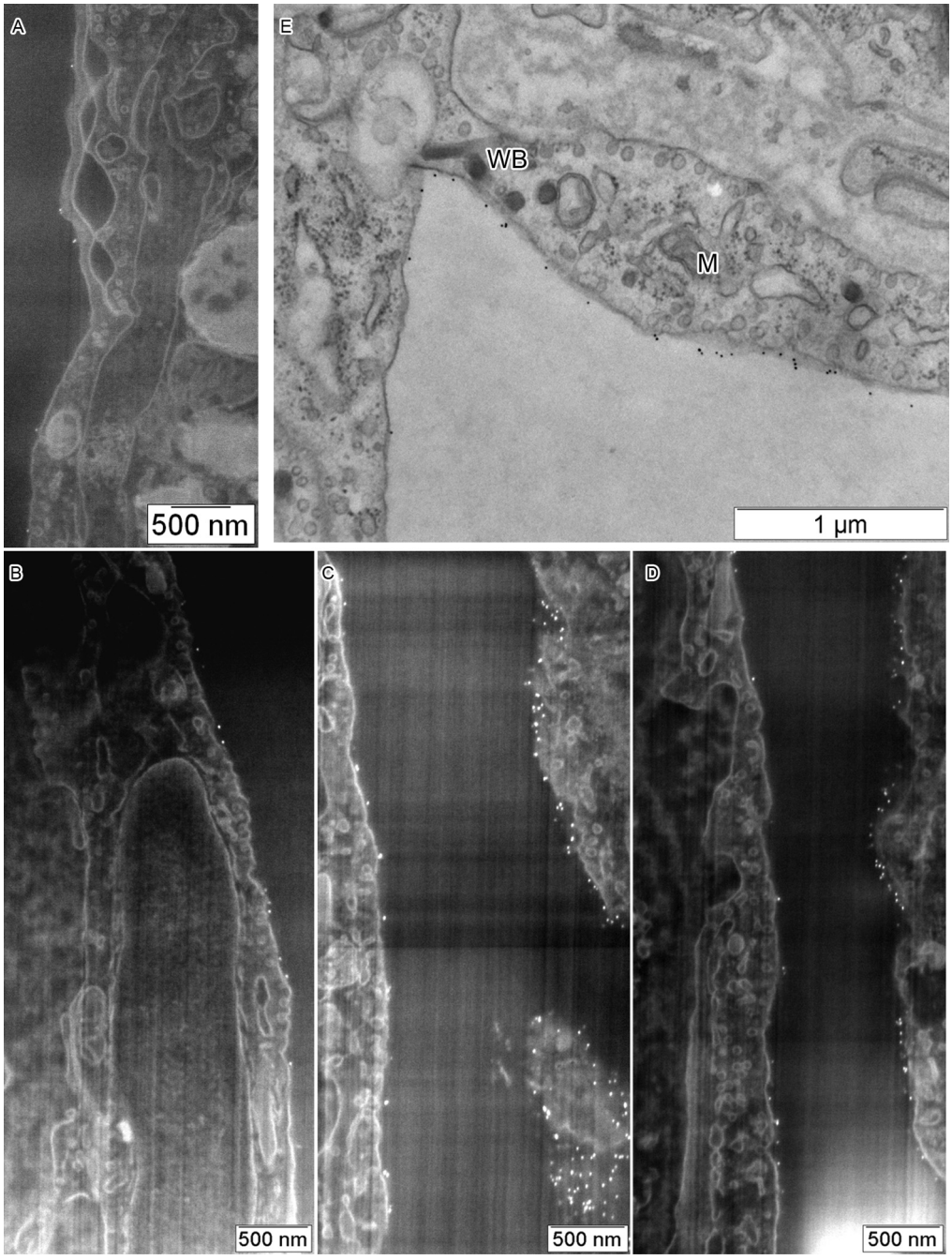


**Figure 2.6. ICAM-1 expression in atherosclerotic tissue of ApoE-/- mice visualized by FIB-SEM.** *A. back scatter electron image taken from an endothelial cell located on the plaque. Hardly any ICAM gold particles are present. B, C and D. BSE images from a slice and view series made from the plaque towards the shoulder region. More ICAM-1 gold particles are observed on the surface of the non-plaque endothelial cells. This is in agreement with figure 2.6.E. in which a conventional TEM image of a 60 nm section of the same sample is shown. In this section more ICAM-1 gold particles are present on the non-plaque endothelial cells. WB=Weibel Palade Bodies; M=mitochondrion.*

the Netherlands) at a specific area. A slice and view series involves automated serial sectioning with the FIB and subsequent imaging with the SEM; producing a 3D image-sequence of the cells/tissue of interest that can be reconstructed into a 3D model (De Winter et al., 2009).

Two areas were investigated: the area indicated in figure 2.2.C[3] and an area surrounding the shoulder of the lesion (performed on a second specimen). In the movie of images acquired during the slice and view series at the plaque area (figure 2.2.C[3]), the intracellular distribution of the lipid droplets within the foam cell located underneath the endothelium can be clearly distinguished (supplementary movie 2.1). It can be seen that the lipid droplets are present within the nuclear plane and thus cause deformations of the nucleus.

A second tomographic volume, obtained by alignment of the images in the slice and view series, around the shoulder area of the plaque, was represented in a 3D model by annotation of the membrane structures in every slice (figure 2.5). This analysis focussed on the contact between two endothelial cells and on the distribution of intracellular membrane systems of the endothelial cell. Panels 2.5.A,B show the area of the vessel wall where slice and view was performed and the two areas of interest: part of the intracellular membranes/organelles of the endothelial cell and the area of interaction between two endothelial cells. The membranes/organelles were annotated and a 3D model of part of the intracellular membranes is shown in figure 2.5.C, highlighting the possibilities of this approach and indicating that indeed membrane compartments can be recognized. An area of specific interest is the connection between two endothelial cells. This area is of interest since it plays a major role in the barrier function of the endothelial monolayer and decreased cell-cell interaction might be involved in the deposition of LDL in the aortic wall (Libby, 2002). In the single slice (figure 2.5.A) it is indicated that at certain areas the cells deviate from each other, resulting in the creation of gaps between the cells, which might hamper the endothelial barrier function. The 3D model (figure 2.5.D; pink colour) shows that indeed

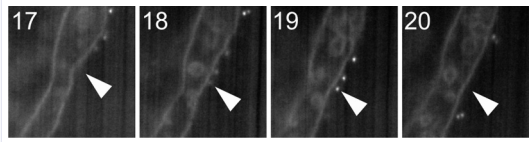


**Figure 2.7. Close up of ICAM-1 gold particles in four successive slices of a slice and view series.** *Gold particles (10 nm) are observed in multiple slices (of approximately 50 nm) indicating that the back scatter electrons penetrate deeper in the tissue than the thickness of these slices; resulting in a slight overlap of information among the slices. Slice number 19 is the real position of the gold particle indicated by the white arrow, since it is lost in the subsequent slice (20); indicating that the particle was milled of the sample, and was thus within 50 nm of the surface.*

within the reconstructed volume the cell-cell contacts are loosened in a relatively large area. Not only is a cell-cell contact modelled, but using this approach it is also possible to model the localization of the caveolae as is shown in figure 2.5.D. No clear differences in caveolae number are observed at this time between the areas with close cell-cell contacts and loose cell-cell contacts.

The approaches described above clearly show the advantage: the increase in *Z*-resolution, and the disadvantage: the slight decrease in *X-Y* resolution, of the FIB-SEM in studying (3D) tissue/cell/organelle configuration/morphology in the areas of interest. However, it does not give insight in the presence and/or distribution of specific molecules. To address the question whether the FIB-SEM can be used to visualize (bio)markers, we labelled a similar piece of artery for Inter Cellular Adhesion Molecule-1 (ICAM-1). ICAM-1 is an adhesion molecule constitutively expressed on endothelial cells and increased upon activation (van Buul et al., 2007). Moreover, it is reported to be involved in the development of atherosclerosis in mice (von der Thüsen et al., 2001). After labelling, the artery was embedded in Epon and examined using the FIB-SEM. Again in SEM mode the architecture of the artery was studied to navigate to the place of interest. We zoomed in on the endothelial cells lining the plaque, since activated endothelial cells are expected in that region. The sample shown in figure 2.5 represents part of this area. Imaging of this region, after milling a small cross section, indeed showed ICAM-1 gold particles on plaque endothelial cells

visualized by Back Scattered Electrons (figure 2.6.A). The expression of ICAM-1in this area, however, was relatively low. Therefore, of this region, a slice and view series at high resolution was performed, imaging towards the shoulder of the plaque.

Since the goal of the approach is to determine potential differences in ICAM expression on the surface of the endothelial cells it is important to know how quantitative the detection is and thus also how far into the specimen gold particles are detected. In figure 2.7 a close up of gold particles are shown in several slices of the slice and view series. Since the gold particles used are 10 nm one would expect to observe the image of a single gold particle in only one slice (one slice is 50 nm). However, it can be clearly seen that specific gold particles can be observed in more than one slice. This is most likely due to the penetration of the BSE, resulting in detection of gold particles up to 100 nm into the material. These images clearly demonstrate the *Z*-direction of the gold particles in this sample and indicate that the FIB-SEM slices can be used to quantify, in this case, ICAM gold particles, however one should keep in mind that the acceleration voltage is kept constant.

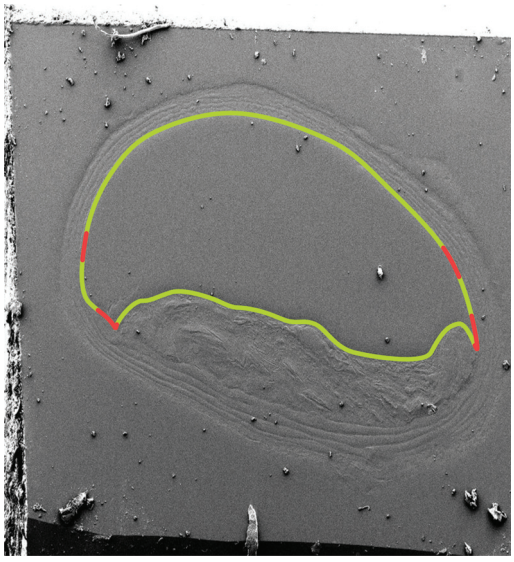

**Figure 2.8. Schematic representation of ICAM-1 expression as an overlay over the SEM image of the artery.** *In red the ICAM-1 high areas are shown and in green the ICAM-1 low areas.*

Focussing mainly on the immunogold labelling, three images of this slice and view series are shown in figure 2.6.B-D. As is shown in figure 2.6.B (and also in figure 2.5.A) hardly any ICAM-1 specific gold particles were present in the plaque area, however, when reaching the shoulder of the plaque more ICAM-1 specific gold particles were observed (figure 2.6.C and 2.6.D). This indicates that indeed the distribution of ICAM-1 is heterogeneous on the luminal surface of the vessel wall.

We wanted to compare the resolution of the slice and view series with conventional 60 nm sections and Transmission EM (TEM). Although the resolution of the slice and view series is reasonable high, compared to the resolution of the 60 nm sections (figure 2.6.E), made before processing the sample for the FIB-SEM, it may be clear that the resolution of conventional TEM is superior. In the conventional TEM section the cellular architecture was clearly visible showing mitochondria, and Weibel Palade bodies. In the slice and view series these organelles were clearly recognizable, however less details were distinguishable. Indeed, it should be noted that, as is observed in figure 2.6.A, the resolution of the FIB-SEM is high enough to detect junctions between endothelial cells and to discern intracellular membrane systems.

The expression pattern of ICAM-1, observed in the conventional TEM section, is similar to the slice and view series: ICAM-1 gold particles are observed on the shoulder region rather than on the plaque endothelial cells. Figure 2.8 shows a schematic representation of the distribution of ICAM-1 gold particles in the artery, indicating the strength of the combination of the FIB-SEM with conventional TEM. From this schematic representation it is clear that ICAM-1 is particularly highly expressed at the shoulder region of the plaque. The presence of ICAM-1 on the plaque endothelial cells is comparable to the presence of ICAM-1 on the endothelial cells in the healthy areas, although some endothelial cells in this area do have a high ICAM-1 expression. With the FIB-SEM these locations of high ICAM-1 expression in healthy endothelial cells can be studied in depth, in greater detail.

## 2.4 Discussion

To gain insight in (sub)cellular changes during physiological and pathological conditions, like atherosclerosis, it will be of eminent importance to study these changes in a correlative way: locate cells/regions of interest at low magnification and study these cells/regions in their environment at ultrastructural level. The drawback of this approach is the use of two separate microscopes. Although the cells/regions of interest are identified rapidly in the light/fluorescent microscope, the sample has to be prepared for EM, transferred to the EM and the same region in 2D but also in *Z* direction has to be located. Furthermore, unless serial sections or thick sections are obtained, it is not possible to get insight into the 3D distribution of organelles or proteins.

Using the FIB-SEM, samples can be studied already at relative low magnification in SEM mode. The regions/cells of interest can be identified at this low magnification and by using the ion beam and BSE, these regions/cells can be further studied in 3D at high resolution *(Knott et al., 2008)*. Relative large cross sections can be milled, imaged and studied (approach 1). In addition, by milling multiple small area cross sections, a specific cell type can be investigated at various locations in the sample (approach 2). Slice and view series performed at specific regions/cells can give insight in the 3D architecture in these regions/cells (approach 3).

As said, one of the advantages/properties of the FIB-SEM is to be able to image at rather low magnification large areas in scanning mode. Since at light microscopical level a cross section of the whole mouse artery can be imaged and the atherosclerotic plaque, which might serve as a morphological landmark, can be identified, we investigated whether we could use the FIB-SEM in a correlative way.

Arteries of ApoE-/- mice, which develop atherosclerotic lesions, were used to study the pathogenesis of atherosclerosis. In SEM mode we were able to image a cross section of the whole mouse aorta at 150x magnification (figure 2.2). An atherosclerotic plaque was clearly visible in the sample, as well as lipid droplets and crystalline cholesterol needles in the plaque. Elastic lamina was visible in the entire sample. At higher magnification, in SEM mode, single foam cells and endothelial cells could be identified. In addition, the membranes in single cells were clearly recognized, although not as a lipid bilayer but as one thick layer, indicating that the X-Y resolution is slightly less compared to conventional TEM.

Navigating through the aorta using the above mentioned approaches, we compared the composition of the atherosclerotic plaque and the healthy region at high resolution. In addition, the (3D) architecture of vascular endothelial cells was studied in relation to their location relative to the atherosclerotic plaque. Zooming in onto the endothelial cells lining the plaque at higher magnification, membrane compartments, like mitochondria and caveolae, could be recognized. At the level of the plasma membrane of the endothelial cells, less luminal surface bound caveolae were observed in the endothelial cells lining the plaque. However, multiple caveolae were located at the cell-cell contacts between two plaque endothelial cells, as was observed in the slice and view series. This observation is the start of a current study to determine in further detail whether indeed the location of caveolae is changed in plaque endothelial cells compared to healthy endothelial cells, and/or whether there is a substantial difference in number of caveolae. The possible importance of this finding is suggested by Rodriguez-Fuo et al. *(Rodriguez-Fuo et al., 2008)* who identified caveolin-1 as a possible biomarker for plaque vulnerability. A decreased expression of caveolin-1 correlated with atherosclerotic plaque destabilisation and rupture. Caveolin-1 is involved in the formation and maintenance of caveolae and the observed decrease in surface bound caveolae in plaque endothelial cells in the present paper might be related to the reported decrease in caveolin-1 in the atherosclerotic plaque.

Study of the 3D model reconstructed from the slice and view series revealed a disturbed interaction between two adjacent endothelial cells. This could

indicate a loosening of cell-cell contact between endothelial cells overlying the plaque and thereby a hampered endothelial barrier function might be induced. Indeed, an increase in vascular permeability has been reported in atherosclerotic patients (Lusis, 2000). This shows that using the FIB-SEM to study cells/tissue provides high resolution information about regions of interest. The slice and view approach can clearly give information on the 3D distribution of membranes and organelles, however, as mentioned above, its *X-Y* resolution is not as high as TEM (see for instance figure 2.6). This means that depending on the questions to be addressed, a decision has to be made between the ability of the FIB-SEM to study relatively large volumes, or the better lateral resolution of other EM techniques. For instance, to study membrane continuities and organelle biogenesis, FIB-SEM might not be the appropriate method to use. However, as we present in the current paper, the method is very valuable for studies regarding 3D distribution of, for instance, organelles in cells present at specific sites of interest. In addition, using the FIB it is possible to prepare a lamella at the site of interest, and transfer it to the TEM for electron tomography.

Labelling the tissue for a specific (bio)marker will provide the necessary information for the location/validation of the (bio)marker. In this paper, we did a pre-embedment labelling of the adhesion molecule ICAM-1, as proof of principle. ICAM-1 is constitutively expressed at the surface of endothelial cells and upregulated upon activation (Van Buul et al., 2007). The expression pattern of ICAM-1 in atherosclerotic tissue is studied previously (Nakashima et al., 1998; Zibara et al., 2000). Its expression was increased at lesion prone sites and at the shoulder of atherosclerotic plaques, as shown by immunohistochemistry. SEM showed a localization of ICAM-1 at the surface of endothelial cells at the lesion prone sites (Nakashima et al. 1998), however at the EM level no information on the distribution of ICAM-1 over the entire endothelial lining of the vessel wall was obtained. ICAM-1 is therefore a suitable protein to confirm the feasibility of the FIB-SEM to locate proteins of interest. Using pre-embedment of the artery and subsequent milling and viewing in the FIB-SEM we were indeed able to visualize ICAM-1 at the surface of endothelial cells, proving the feasibility of using the FIB-SEM in protein localisation studies. As expected based on the histochemistry, ICAM-1 high areas were observed especially on the shoulder region of the plaque using the FIB-SEM. This was confirmed by analysis of the thin sections made of the same sample before preparation for the FIB-SEM. On the surface of the plaque endothelial cells hardly any ICAM-1 gold particles were observed. Also at some areas of the healthy parts of the vessel wall highly ICAM-1 positive cells were observed. Further investigations showed that these endothelial cells were overlying a macrophage, indicating very early stages of inflammation, possibly resulting in the start of an atherosclerotic plaque (data not shown).

Besides obtaining information regarding the 3D localisation of ICAM-1, the gold particles in the slice and view series illustrate that the back scatter electrons penetrate deeper into the tissue than the thickness of in the consecutive slice (figure 2.7). This implies that there is no loss of information due to the slice process. It also means that, provided that the acceleration voltage is kept constant, quantification of the gold particles is possible using the FIB-SEM.

By combining FIB-SEM and conventional TEM, we are able to visualize the quantification the number of specific gold particles on the vascular endothelial cells, in our case ICAM-1 gold particles. A schematic impression can then be prepared of the expression of the biomarker of interest as a layer over the SEM image of the artery (figure 2.8) showing the distribution of the biomarker.

At this moment a drawback of the FIB-SEM as a correlative microscope is that the region of interest must be distinguishable at low magnification, based on its morphology in SEM images. To identify specific (bio)markers expressed by only a small number of cells and thus present in only a small part of the tissue, and to study these specific cells at higher resolution, new approaches will have to be developed to specifically recognize and

navigate towards these areas. However, to locate surface (bio)markers for either early atherosclerosis or for identification of the vulnerable plaque, finding the plaque at low magnification is sufficient to be able to find the (bio)markers at high resolution.

In conclusion, in this paper we clearly show the advantage of the ability of the FIB-SEM to navigate in a large sample at low magnification to places of interest and, in addition, to zoom in onto these places to visualize the (3D) architecture of the cells of interest. In addition, the distribution of proteins of interest at high resolution, as described in this paper, makes the FIB-SEM a valuable tool for correlative microscopy in biology.



## Acknowledgements

This work was supported by a grant from Senter Novum, IOP Genomics (IGE03012), a grant of FEI, NWO Groot (175.010.2005.007), and the Dutch Cyttron project. We thank Dr. V. de Waard for helping with the mouse material, Prof. R.E. Mebius for kindly providing the ICAM antibody and E.D. Keuning for assistance with the tissues.

# CHAPTER III

## template matching as a tool for annotation of tomograms of stained biological structures

# template matching as a tool for annotation of tomograms of stained biological structures

M.N. Lebbink[◎] • W.J.C. Geerts[◎] • T.P. van der Krift[◎] • M. Bouwhuis[◢]
L.O. Hertzberger[⁞] • A.J. Verkleij[◎] • A.J. Koster[▪▪]

[◎] *Cellular Architecture and Dynamics, University of Utrecht, the Netherlands*
[◢] *SARA Computing and Networking Services, Amsterdam, the Netherlands*
[⁞] *Department of Computer Science, University of Amsterdam, the Netherlands*
[▪▪] *Molecular Cell Biology - Electron Microscopy, Leiden University Medical Center, the Netherlands*

Everyone is a prisoner of his own experiences. No one can eliminate prejudices - just recognize them.

*Edward R. Murrow*

Published in *Journal of Structural Biology*
**158**: 327-335 *(2007)*

In recent years electron tomography has improved our three-dimensional (3D) insight in the structural architecture of cells and organelles. For studies that involve the 3D imaging of stained sections, manual annotation of tomographic data has been an important method to help understand the overall 3D morphology of cellular compartments. Here we postulate that template matching can provide a tool for more objective annotation and contouring of cellular structures. Also, this technique can extract information hitherto unharvested in tomographic studies. To evaluate the performance of template matching on tomograms of stained sections, we generated several templates representing a piece of microtubule or patches of membranes of different staining-thicknesses. These templates were matched to tomograms of stained electron microscopy sections. Both microtubules and ER-Golgi membranes could be detected using this method. By matching cuboids of different thicknesses, we were able to distinguish between coated and non-coated endosomal membrane-domains. Finally, heterogeneity in staining-thickness of endosomes could be observed. Template matching can be a useful addition to existing annotation-methods, and provide additional insights in cellular architecture.

## 3.1. Introduction

Electron tomography is an imaging technique, using transmission electron microscopy (TEM), to explore the structural architecture of cells and organelles in three dimensions (3D). This is achieved by recording two-dimensional (2D) images of a specimen at different tilt angles. A 3D reconstruction (tomogram) is calculated from the 2D projections by a computational method (e.g. back-projection), resulting in a digital 3D representation of the specimen. Typically, for those applications where stained sections are imaged, digital slices with a *Z*-resolution of two to five nanometers are visualized (Kremer et al., 1996; Koster et al., 1997). These digital slices are then used to generate 3D contours of the structure. Electron tomography has become an indispensable tool in morphological studies concerning 3D structural analysis and membrane connectivity; providing additional insight into cellular organization (Murk et al., 2004; Mogelsvang et al., 2004; Lucic et al., 2005; Frey et al., 2006).

Among others, the resolution in a tomogram depends on the number of angles at which 2D projections were taken. This number is limited by several technical restrictions. First, at high tilt angles, e.g. higher than 65 degrees, the sample holder and the thickness of the sample will provide a limit. Second, exposure to the electron beam has to be limited to prevent specimen changes (Bennett, 1974; Egerton et al., 2004). The missing projections at high tilt angles will result in a direction-dependent loss of resolution in the tomogram (McEwen et al., 1996; Koster et al., 1997). This artefact (missing wedge) can be reduced by combining two perpendicular tomograms of the same area, resulting in clearer and sharper cellular structures with more isotropic resolution (Penczek et al., 1995; Mastronarde, 1997).

Electron tomograms show an overwhelming amount of structural detail. To better understand a particular arrangement within a tomogram, a segmentation step is performed to highlight the structure of interest and to remove unrelated information. In electron tomography of stained sections this is often done in a manual fashion by computer assisted drawing of membrane-structures in each digital slice throughout the tomogram. These traced contours are combined into a 3D model used for further analysis. Due to the manual nature of this annotation-step, some degree of subjectivity cannot be prevented.

During the last decade several powerful methods became available for the 3D segmentation of structures within tomograms. Some of these methods focused on improving the signal-to-noise ratio within tomograms (e.g. anisotropic diffusion filtering by Frangakis & Hegerl, 2001), on careful analysis of texture and contrast (e.g. watershed by Volkmann, 2002) or on development of wavelet filtering (Frangakis et al., 2001; Moss et al., 2005). A limitation of these approaches is that no special means are taken to avoid misinterpretation, or mis-segmentation, due to the missing wedge in tomograms, a characteristic phenomenon in electron tomography.

Another approach to highlight structures of interest is template matching, as described by Böhm and Frangakis (Böhm et al., 2000; Frangakis et al., 2002). With template matching, a small 3D volume containing the structure (the template) to be detected is matched to every location within the tomographic reconstruction. The computer determines the maximal cross-correlation value based upon the similarity between the normalized template and tomogram, at every location within the tomogram and for all (predefined) angular orientations. The correlation coefficient indicates how similar the matched template and the structure in the tomogram are. This approach has proven to work well for cryo-applications to localize macromolecular complexes in cells, or to localize, and average, repetitive features in parts of tomograms with templates obtained with higher resolution techniques.

We propose to use template matching as a reasonably objective method to detect and annotate a wide range of cellular structures in cryo-fixed, freeze substituted and plastic embedded sections. It should be noted that while the matching is an automated and objective process, the determination of the optimal threshold of correlation still occurs manually on visual criteria. The optimal threshold of correlation is defined as the lowest cross-correlation value at which no false positive matches could be observed (and thus a maximum of exclusively correctly matched structures was segmented). Segmentation based on template matching allows relatively low resolution morphological information, such as membrane-bound organelles, to be contoured and annotated in a semi-automatic fashion. In addition, by zooming in at the automatically annotated structures, morphological features that were possibly otherwise missed by the human eye, due to the overwhelming amount of stained features in a cell section, might become available. We have chosen to create simplified artificial templates to segment the morphological feature of interest computationally. An advantage of these simple templates is that, depending on the feature of interest, templates can be generated based upon general 3D shapes like cylinders, cubes, spheres, or cuboids. In this manuscript, for the relatively low-resolution requirements of the template-matching application, we build cylinders to mimic microtubules and cuboids (solid rectangular boxes) to mimic patches of membrane. The computer generated templates allow for simple controlled manipulation of a single property of the structure contained therein. That way, this property can be investigated by comparing how well each template fits. For this we compared the matching patterns of the different cross-correlations at the same manually defined threshold. To exemplify this, we used cuboid-shaped templates of different voxel-thicknesses to investigate inhomogenously stained membranes.

Variations in membrane staining may indicate differences in localization of receptor proteins and signal transduction molecules. For instance, in stained sections, membrane-coats, such as clathrin, usually appear darker and thicker than (surrounding) non-coated membranes (Ladinsky et al., 1999). Furthermore, biochemical studies have shown membrane composition to be inhomogeneous throughout the cell. For example, throughout the secretory pathway, the concentrations of cholesterol per phospholipid and especially sphingomyelin increase (Yunghans et al., 1970; Zambrano et al., 1975; Moreau & Cassagne, 1994), and thereby induce thickening of the membrane (Nezil & Bloom, 1992; Smondyrev & Berkowitz, 1999). In addition lipid-composition might cause a depletion or accumulation of certain proteins in membrane domains (Simons & Ikonen, 1997; Killian, 1998). Each of these events can have an influence on staining efficiency/capability; indirectly indicating differences in biological functions. It must however be noted, that staining can also be the source for artefacts and misinterpretation. Therefore, it can be difficult – and often impossible – to compare different sections if the correct controls are not included; even when they are obtained under the same experimental conditions. Even a comparison between two (distant) regions of the same section should be avoided because of an inhomogeneous penetration of the staining liquids. Nevertheless, if differences in staining between neighbouring regions of the same membrane can be observed, then this can be considered an indication for differences in biological composition.

## 3.2. Material and Methods

### 3.2.1 Sample Preparation and Electron Tomography

Human dendritic cells were grown and prepared as described by Murk et al. (2003). TEM tomography was performed with a Tecnai 20 microscope (200 kV) by taking two perpendicular tilt series of angular projections starting at -65º with an increment of 1º. These series were reconstructed and combined into a double tilt electron tomographic reconstruction using IMOD (Kremer et al., 1996).The areas of interest were cropped from the double tilted tomographic images. The template matching approach was evaluated on three tomograms. The sizes of the tomograms were 528x256x544 voxels with a voxel-size of 1.34x1.34x1.34 nm, 1024x88x1024 voxels with a voxel-size of 1.68x1.68x1.68 nm, and 1024x128x1024 voxels with a voxel-size of 1.68x1.68x1.68 nm; respectively for the endosome, and two tomograms containing cellular structures including the ER and Golgi-apparatus. The tomogram of the endosome was binned to dimensions of 264x128x272 voxels.

### 3.2.2 Template Matching

For the template matching algorithm we used the Omnimatch program, kindly provided by the Baumeister group at the Max-Planck-Institute for Biochemistry, Martinsried. The OmniMatch software was implemented on a computer-cluster at the SARA high performance computing facilities in Amsterdam, the Netherlands. Matlab (Mathworks Inc.) was used in combination with the TOM-toolbox scripts (Nickell et al. 2005) to create the templates, masks, and convert the datatypes. Amira (TGS) was used for volume visualization and surface rendering.

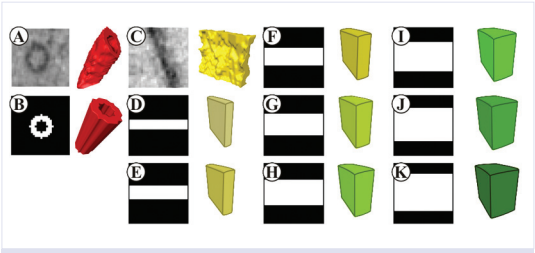


**Figure 3.1. Templates used for matching.** *In the tomograms, microtubules (A) and membrane (C) were matched using computationally generated 3D templates (B; D-K). As a template for the microtubules, an open cylinder with an inner radius of 3 voxels and an outer radius of 6 voxels was created (B). For the membrane, a cuboid-shaped templates were created (D-K) with a thickness of 4, 6, 8, 10, 12, 14, 16, and 18 voxels. The pseudo-colours in the 3D representations of the templates are assigned from light yellow for a low template thickness to dark green for a high template thickness.*

First, to be compatible with Omnimatch software, the grey-scale tomograms as produced by IMOD were inverted, such that the stained membranes appear bright on a dark background. Two types of templates (with file dimensions of 32x32x32 voxels) were created with MatLab and the TOM-toolbox. The tubular template had an inner-radius of 3 voxels, an outer-radius of 6 voxels, and a length of 32 voxels (figure 3.1.A, B). The cuboids with dimensions $X$ and $Z$ equal to the template size, and even thicknesses in $Y$-dimension ranging from 4 to 18 voxels (figure 3.1.C-K). The structure was given value 1 (white) while the background was value 0 (black). Finally, masks were created to define the area containing the structure in the template. The masks were binary 3D images which indicate the area within the template that contains the structure of interest. Only those voxels in the template that correspond to a voxel in the mask with a value of 1 are taken into account for the correlation process; while those that correspond to a voxels of value 0 are excluded. A spherical mask (value=1) with a radius of 14 voxels was created on a black background (value=0). Dedicated masks were created for the cuboid templates based upon the thickness in Y by adding two additional voxels (containing background values in the template) on either side. The thicknesses of these masks range from 8 to 22 voxels. Finally, the point-spread function (PSF) was described as a single white voxel (value=1) at position (1, 1, 1). The PSF describes the distortion of a single pixel due to acquisition and processing of the image, and can be used to take missing wedge/pyramid-artefacts into account by distorting the template prior to the cross-correlation-step. A single white voxel mimics an ideal microscope and perfect data collection in which no distortion takes place, and no wedge-artefacts are present.

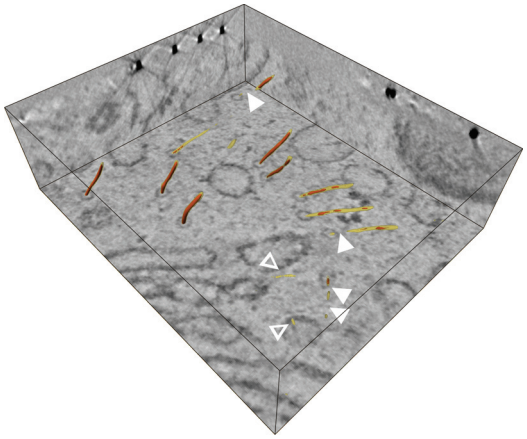

**Figure 3.2. Localization and annotation of microtubule.** *Microtubules were localized using template matching with a tubular template and a spherical mask. Template matching localizes the structure of interest: a brighter peak in the correlation file indicates when the template is present in the tomogram. This peak is visualized by setting a grey-value threshold. Red shows the regions of microtubules that were identified at a threshold value of 0.485 (the optimal threshold of correlation) and the transparent yellow lines show the regions of the microtubules that were identified at a relatively low threshold (approximately 20% below the optimal threshold of correlation). Lowering the threshold leads to less false negatives, and thus to more complete tubules; even though some holes still exist (closed arrowheads). False positives appear if the threshold is set too low (open arrowheads), falsely indicating the presence of a microtubule at this location.*

The Euler angles, as defined in the TOM toolbox [Nickell et al. 2005], over which the template was rotated were 180º over psi (ψ) and theta (θ) with an increment of 5º; beyond these values repetition of the template occurs. Due to symmetry, rotation over phi (φ) was not necessary, since the shape of the templates was such that rotation over this axis would not produce a new image. The dimension of the Fourier transform was set to the smallest dimension in the tomographic volume. The different calculations took approximately 20, 70, and 90 minutes respectively for each volume, using 54 parallel CPUs.

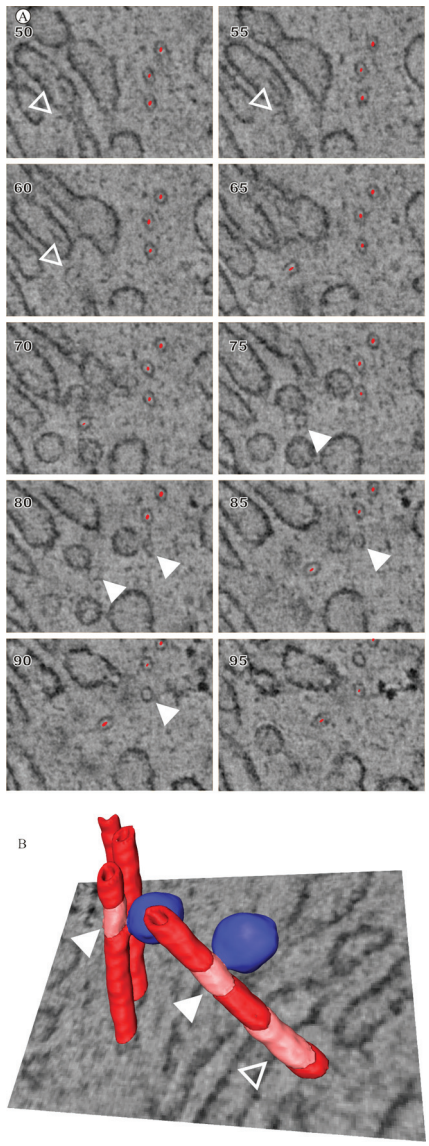


**Figure 3.3. Areas with false negatives on microtubules.** *The top panel (A) shows a series of digital slices through a tomogram. Localization results are shown in red with a threshold of 0.4 (approximately 20% below the optimal threshold of correlation). Vesicles that appear to be attached to the microtubules gave rise to false negatives (closed arrowheads). Similarly, membranes of the Golgi-apparatus in proximity of the microtubules result in false negatives of the matched microtubule (open arrowheads). These results are visualized in a manually annotated 3D model (B) where red shows the regions that were localized using template matching, pink are the false negatives that the procedure missed, and in blue vesicles are shown. The arrowheads show the same regions as presented in the top panel.*

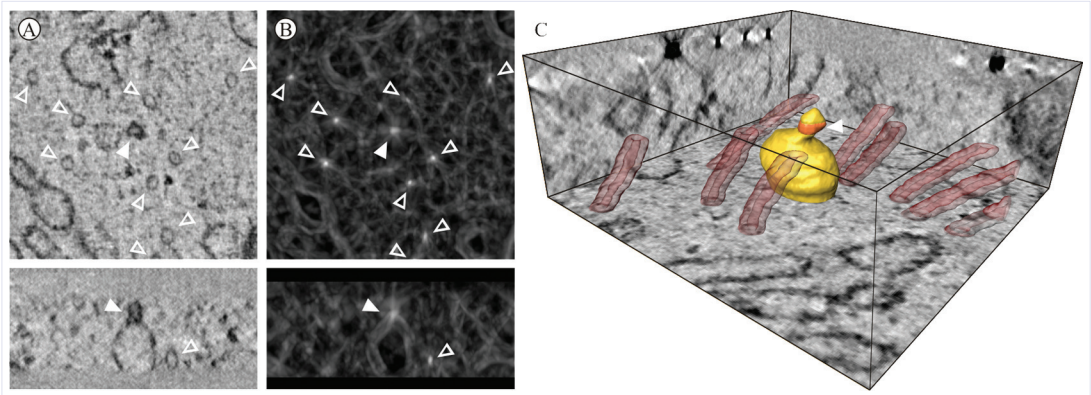


**Figure 3.4. Areas with false positives on microtubules.** *Tubulation of a membrane (A; closed arrowheads) resembles the microtuble-template. As a consequence, a bright correlation-peak could be observed at that location in the tomogram (B; closed arrowhead) along with the correlation-peaks of the microtubules (open arrowheads). This tubulation was visualized in a 3D model by manual annotation. The orange region (C; closed arrowhead) shows where a tube was detected at approximately 10% below the optimal threshold of correlation.*

### 3.2.3 Data Visualization

The outcome of the template matching procedure is a 3D volume with cross-correlation values. For the segmentation and contouring approach, these cross correlation values (ranging from -1 to +1) were visualized by surface rendering, using Amira. To reduce the requirements on in-core computer memory, the 16bit cross-correlation values as produced by Omnimatch were scaled and converted to 8bit images. By varying the grey-value threshold during surface rending it is possible to visualize the location of a matched structure. To describe the performance of template matching for the purpose of contouring, we introduce the terms 'false positive'- and 'false negative'-annotation. With false positive annotation is meant that, at a particular threshold, the surface-rendered cross correlation values show features which should not be shown from a cell-biological point of view. For instance, false positive annotated structures could be elongated parts of membranes while it is attempted to annotate only microtubules. With false negative annotation is meant that parts of a particular organelle that, based upon visual inspection of the tomogram by a cell-biologist, should have been annotated but wasn't.

## 3.3. Results and Discussion

### 3.3.1 Automatic Detection of Microtubules in TEM-images

At relatively low resolution, ~5 nm, microtubules share a very homogeneous, tubular, shape. In electron tomographic reconstructions of stained sections microtubules are often abundant, and relatively easy to detect and recognize upon visual inspection. Moreover, microtubules are involved in many cell biological processes and automated annotation of these structures in tomograms can contribute to further understanding of cell biological events as it can provide a skeleton of annotated (known) structures. These arguments make microtubules suitable for evaluating the template matching procedure.

In figure 3.2 annotated microtubules are shown. At a first glance, most microtubules appear to be detected correctly. On closer examination, we observed that (even at a low correlation-threshold when false positives appear (open arrowheads)) holes are present in some of the detected microtubules (closed arrowheads). When analysing the tomographic regions that were missed using template matching, we noticed that these holes revealed biological occurrences easily overlooked by manual annotation. For instance, as shown in figure 3.3, in several of these regions, vesicles

(figure 3.3.A; closed arrowhead, figure 3.3.B) or other membranous structures (figure 3.3.A; open arrowhead) associated with the microtubules could be observed. Figure 3.4 shows correctly annotated microtubules, together with a false positive annotated structure; membrane tubulation (figure 3.4; closed arrowhead). While misinterpreted from a biological point of view, the template correctly annotated a short cylinder-shaped feature.

Based upon these observations, we conclude that template matching can be used as an additional tool to detect structures like microtubules within a TEM-reconstruction containing stained cellular structures. Furthermore, we showed that while localization and morphology can be examined based on where the template fits in the tomogram, false negatives can indicate equally significant information from a cell biological point of view.



### 3.3.2 Visualization of membranes in the ER and Golgi-apparatus

Membranes are extensively modelled features in electron tomograms of stained sections. While at a 5 nm resolution scale, microtubules appear as rather homogeneous structures that can be annotated quite effectively, membranous structures are often more complex to contour. To evaluate whether template matching can be used to visualize such membrane-systems we looked at the endoplasmic reticulum (ER) and the Golgi-apparatus. Both these organelles play an important role in the secretory pathway, and their transport mechanisms have been extensively studied. In recent years electron tomography has been extremely valuable in understanding the architecture of these organelles. As a model for the membrane we used a cuboid template of 4 voxels thick with a corresponding cuboid mask of 8 voxels thick; resembling the average thickness of the membranes manually observed in the tomogram. In figure 3.5 it

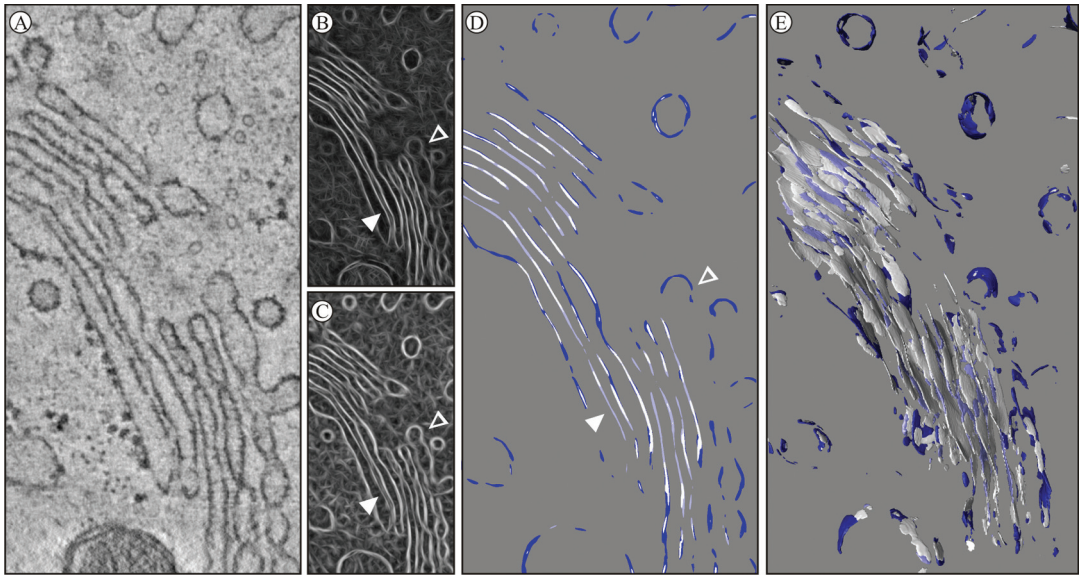


**Figure 3.5. Localization and annotation of the Golgi-apparatus.** *A small region of a tomogram containing a Golgi-apparatus is shown in figure 3.5.A. Cross-correlation results are shown for a cuboid model of a 4 voxel thick membrane matched both with a cuboid mask (B) and a spherical mask (C). Curved membranes are better detected using a spherical mask (open arrowheads), while the cuboid mask allows a clear distinction between membranes in close proximity to each other (closed arrowheads). An overlay of both cross-correlations exceeding the optimal threshold of correlation is shown in (D), where dark blue represents the area exclusively detected by using the spherical mask, light blue is the area detected only with the cuboid mask, and white is the overlapping area detected by both. (E) shows a semi-automatic 3D-model of a Golgi-apparatus created by combining the cross-correlation results of both calculations.*

is shown that automatic segmentation of complex membranous structures with a limited curvature is indeed possible using template matching with these settings (figure 3.5.A, B, and D (light blue and white)).

Though large parts of the membranes are correctly annotated, a significant amount is missed (false negatives). Due to the cuboid shape of the template, regions in the ER where ribosomes are attached to the membranes were largely excluded.

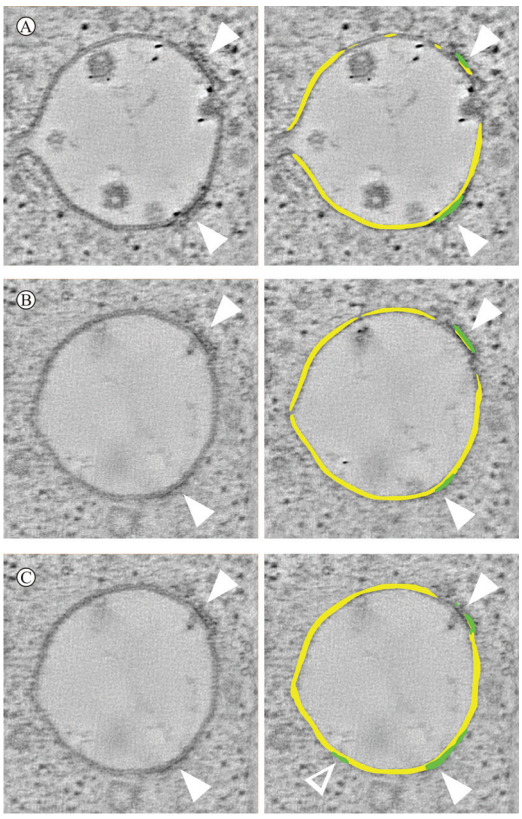


**Figure 3.6. Localization and annotation of thick clathrin coats on endosomes.** *We localized clathrin coats (green, close arrowheads) present on endosomal membranes (yellow) based upon a difference in stained thickness between coated and uncoated membrane, (A) and (B) show different optical slices with an overlay of the matched cuboid of 6 voxels (yellow) and 16 voxels (green) in thickness at a cross correlation threshold of 0.5. (C) shows the same section as (B) but with a threshold of 0.45. A region in the uncoated membrane appears (open arrowhead), where the thicker template has a higher correlation-value to the tomogram than in the surrounding membranes.*

Furthermore, in the trans Golgi network (TGN) the strong curvature and many membrane constrictions hinder automatic segmentation using this template and mask (figure 3.5.B, open arrowhead). We found that by using a spherical mask (instead of a cuboid mask) that the curvature of the membrane resulted in less false negatives (figure 3.5.C, open arrowhead, D (dark blue and white)). This is due to the fact that with the cuboid-shaped mask the background intensities are excluded. By including these with the spherical mask, the relative importance of the intensities describing the shape of the structure decreases. As a consequence, slightly curved membranes will still be considered to resemble the template as long as its environment (contained within the masked area) is devoid of any other structures. On the other hand, two membranes close together will be lost from the matching with a spherical mask (figure 3.5.C, closed arrowhead), whereas the cuboid mask detected two clear distinct membranes (figure 3.5.B, closed arrowhead). By combining the models created using both masks (figure 3.5.D), we optimized the performance of annotation and were able to obtain a 3D surface-rendered representation of these membranous cellular compartments in an semi-automatic manner (figure 3.5.E). The matchings were combined, by including those voxels that exceeded the optimal threshold of correlation for either or both of the conditions.

### 3.3.3 Automatic Detection of Coated Membrane Domains on Endosomes

Cellular membranes have a heterogeneous composition. Differences in lipid and protein composition are associated with the formation of domains *(Brown, 1997; Pfeffer, 2003)*, many of which are known to play a functional role in the cell. Among those, clathrin coats on endosomes *(Raposo et al., 2001; Sachse et al., 2002)* are suitable to evaluate the possibilities of using template matching to identify such domains. Endosomes possess a relatively simple membranous organization, and in electron tomographic reconstructions these coats can be visualised against the endosomal membrane as thick patches *(Murk et al., 2003)*. To discriminate between these thick patches and the thinner uncoated

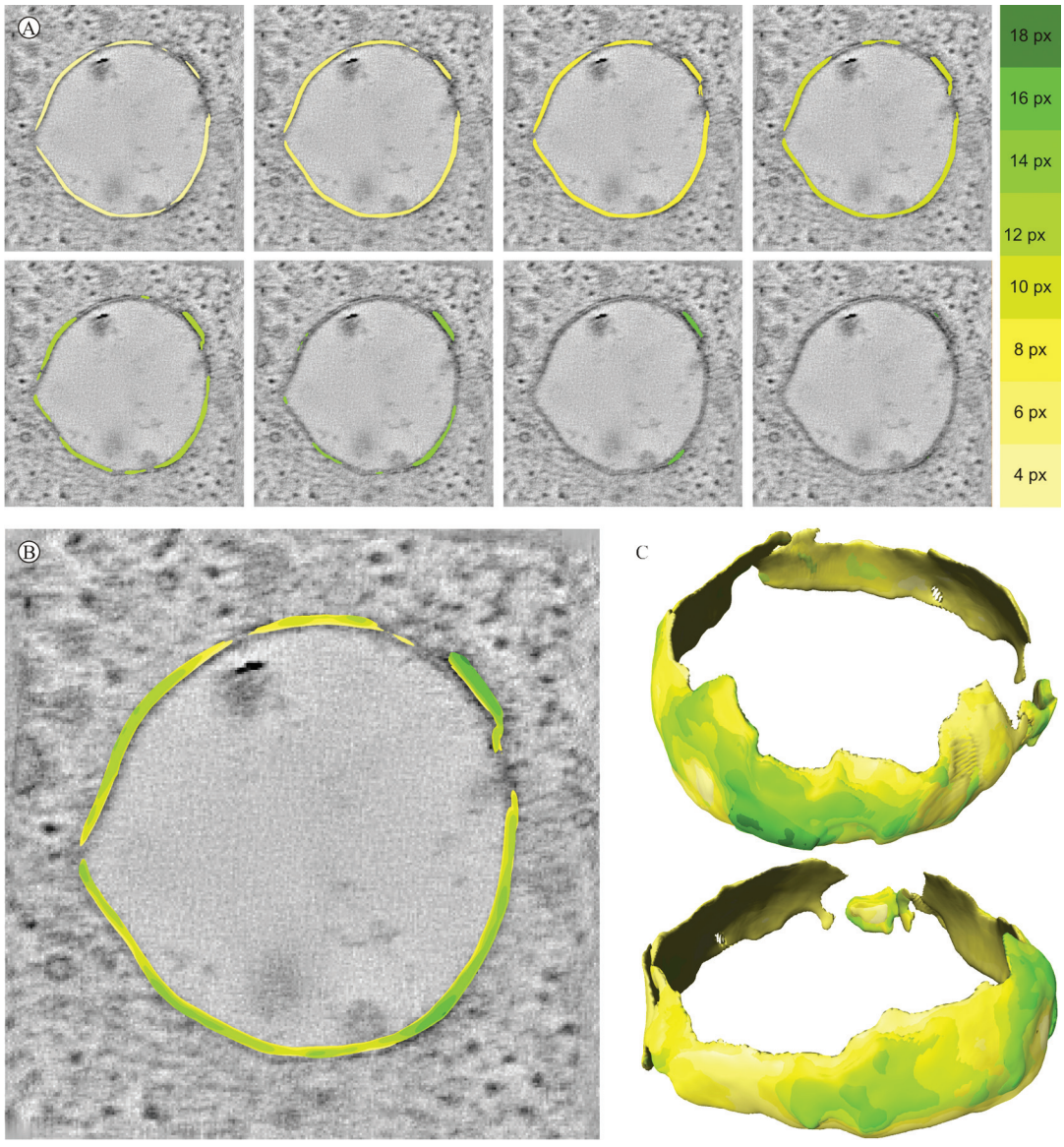


**Figure 3.7. Visualization of heterogeneity in stained membranes of a endosomal structure.** *A series of cuboid templates of increasing thickness (figure 3.1.C-K) were matched to the endosome. Based on the local stained thickness of the membrane these templates matched differently as visualized in (A) separately for each template at a correlation threshold of 0.5. In the overlay (B) and the 3D model (C) clear thinner and thicker stained regions can be seen indicating heterogeneity in membrane composition represented by a difference in membrane staining.*

membranes, we applied two artificially generated cuboid templates of distinct different thicknesses (6 voxels and 16 voxels; figure 3.1.E&J) to a tomogram of an endosome with clathrin coats. As shown in figure 3.6 (A and B, closed arrowheads), it is indeed possible to discriminate between coated and non-coated membranes. By comparing the automatically annotated model to the one published by Murk et al, we note that at a cross-correlation-threshold of 0.5 (the optimal threshold for the 6

voxels thick template) all the manually identified, thicker clathrin coats were exclusively localized in the membrane. We noticed that when we lowered the threshold to 0.45, a third region appeared in an area of uncoated membranes (figure 3.6.C, open arrowhead). This value was considered the optimal threshold of correlation for the 16 voxels thick template.

Considering the resolution-range aimed for to annotate the cellular architecture, the template chosen to detect the clathrin patches was not based on the ultra-structure of clathrin, but based on the fact that clathrin coats simply appear thicker on stained membranes. As such, the technique is used as a tool to detect variations in membrane-staining thickness instead of localizing specifically clathrin.

Heterogeneity within non-coated membranes of endosomes is not unexpected, since the membranes of internal vesicles in multi-vesicular bodies and its limiting membrane have different protein and lipid compositions [Kobayashi et al., 1998], indicating lipid sorting in the membrane. We therefore set forth to visualize membrane regions of different staining thicknesses (figure 3.7.A). We created several cuboid templates of different even thicknesses ranging from 4 to 18 voxels (figure 3.1.D-K). If the membranes were homogeneous, and no detectable different domains would exist, each template is expected to fit equally well on every location of the membrane. Also, a single template – with a thickness closest to the thickness of the stained membrane – is expected to fit best for the entire membrane of the structure. However, in case of staining-heterogeneity, different templates will fit best at different locations corresponding to thicker and thinner stained-patches, and templates will not fit equally throughout the membrane. For each of the eight different membrane templates we set the threshold for the minimal cross-correlation to 0.5 (the highest optimal threshold for any of the templates). Those regions exceeding the threshold are presented in figure 3.7.A. To visualize the distribution of thicker (green) and thinner (yellow) regions on the endosomal membrane we projected these regions on top of each other (figure 3.7.B). While the thick, coated patches are clearly visible, colour variations (representing differences in stained thickness) can be observed throughout the regions of uncoated membrane. In figure 3.7.C this heterogeneity in membrane staining is presented in 3D. It seems that these variations are not randomly distributed, since patches of connected regions are visible rather than randomly distributed small spots. This is an indication that these regions are genuine reflections of biological structures with different biological functions. It is however unclear at this time what they truly represent, and if the visualized heterogeneity has any biological significance in terms of protein sorting or vesicle budding.

## 3.4. Conclusions

For structures in tomograms of stained sections, template matching provides a less subjective way of analysing the data when compared to manual annotation. Template matching introduces a degree of quantification and automation in analysing morphological studies. Furthermore, it can help pinpoint to biologically relevant phenomena in the tomogram that are easily missed by eye alone. By varying a single property of an artificial (computationally generated) template matched to a volume, it is possible to examine this property by analysing how well each variation fits at a given location. We have illustrated this possibility by matching cuboid templates of increasing thickness to stained membranes to visualize patches of clathrin-coats and heterogeneity.

Template matching can be a valuable addition to manual annotation of tomograms of microtubules and membranous structures. Though it is possible to trace cellular structures automatically, the technique still requires a human component. First, if present, incorrectly annotated structures (false positives), have to be removed. This can be done either by raising the correlation threshold, or by manually erasing the falsely annotated structures. Second, if present, missed structures (false negatives) have to be compensated for, either by lowering the correlation threshold, or by manual contouring.

While template matching can visualize membranes in a cell, it cannot distinguish between membranes of different organelles. To achieve exclusive segmentation of the organelle of interest, correctly identified membranes of surrounding organelles have to be removed by manual intervention. Moreover, in some studies, different membranes of a single organelle (for example the different stacks of a Golgi-apparatus) have to be distinguished by user expertise. Such a distinction cannot be achieved by an automated template matching procedure

To understand the overwhelming amount of structural details within a tomogram, segmentation steps are unavoidable. Template matching is one of the possible approaches to model the content of tomograms, and can help unravel complex cellular architecture in stained sections.



## Acknowledgements

We would like to thank Jean-Luc Murk, Hezder van Nispen tot Pannerden, and Hans Geuze for providing us with the tomograms of the endosome and its accompanying model. Also, David Lutje Hulsik, Alevthyna Yakushevska, Hakan Yakali, and Sandra Waaijenborg for their constructive discussions. Furthermore, Friedrich Förster, Reiner Hegerl, Stephan Nickell, Achilleas Frangakis, and Wolfgang Baumeister from the Max-Planck-Institut für Biochemie in Martinsried for providing the OmniMatch-software for template matching and, Bart Heupers from the SARA computing and networking services in Amsterdam for his help with integrating and running the OmniMatch-software on the Dutch grid environment. This research has been made possible by the IOP genomics project.

# CHAPTER IV

# STEM tomography in cell biology

# STEM tomography in cell biology

A.E. Yakushevska° • M.N. Lebbink° • W.J.C. Geerts° • L. Spek° • E.G. van Donselaar°
K.A. Jansen▪ • B.M. Humbel° • J.A. Post° • A.J. Verkleij° • A.J. Koster▪

° *Cellular Architecture and Dynamics, University of Utrecht, the Netherlands*
▪ *Molecular Cell Biology - Electron Microscopy, Leiden University Medical Center, the Netherlands*

Noise is the most impertinent of all forms of interruption. It is not only an interruption, but is also a disruption of thought.

*Arthur Schopenhauer*

Published in *Journal of Structural Biology*
**159**: 381-391 *(2007)*

Transmission Electron Tomography has been used in biological sciences for quite some time and proven to be a valuable tool. However, to date, the different Scanning Transmission modes are almost not used for electron tomography on resin-embedded biological material. We explored different STEM modes on Epon-embedded, osmium-uranyl-lead-stained biological material. Bright Field-TEM and High Angle Annular Dark Field-STEM tomograms from the same areas were recorded and compared. Contrast and signal-to-noise ratios were calculated. Template matching was used to validate results obtained in Bright Field-TEM and High Angle Annular Dark Field-STEM tomograms. It is concluded that High Angle Annular Dark Field-STEM gives a five times better contrast and signal-to-noise ratio than Bright Field-TEM. Template matching showed that 1.3 times more information could be extracted from High Angle Annular Dark Field-STEM tomograms than from Bright Field-TEM tomograms.

## 4.1. Introduction

In many material and life sciences studies, three-dimensional (3D) structural information at high resolution can provide valuable clues on material composition or biological processes. During the last 15 years, advanced methods and equipment to image structures in 3D have been developed and made available to the scientific community. Transmission Electron Microscopy (TEM) is a powerful tool to study cellular ultrastructure as it can generate images with nm-scale resolution. TEM is therefore highly suitable to visualize organelles such as the Golgi apparatus. However, TEM provides two-dimensional (2D) images, which are basically 2D projections of the 3D specimen in the microscope. Due to the stacking of 3D features in the 2D images, the 3D architecture is difficult to reveal.

Electron Tomography (ET) is a method that restores high-resolution 3D information of structural components from a set of 2D images obtained by TEM (Frank, 1995; Koster et al., 1997; Baumeister et al., 1999; Midgley & Weyland, 2003; Hoppe & Hegerl, 1980). In ET a series of 2D projection images is acquired of a sample that is tilted over a large angular range (±70°) and with small tilt increments (usually 1 degree). After aligning the projection images of the tilt series relative to each other, a 3D-reconstruction (i.e. tomogram) is computed. Depending on the accelerating voltage and the use of energy filtering, ET can be applied to biological samples of about 100 to 1000 nm in thickness. This makes it a powerful method for imaging cell membranes, organelles and other subcellular structures, including the Golgi apparatus (Trucco et al., 2006; Mironov et al., 2003), nuclear membranes (Beck et al., 2004), and peroxisomes (Geuze et al., 2003).

High-resolution 3D imaging of biological samples requires a high degree of preservation, close to the native state, of the cellular architecture and macromolecular complexes. This can be achieved by employing a cryo-immobilization procedure such as plunge-freezing or high pressure freezing (HPF).

For many cell biological questions it is important to localize specific molecular structures within the cellular context. Electron tomography of frozen-hydrated specimens is a powerful tool to provide 3D structural maps of cell organelles with sufficient resolution to localize those specific molecular structures on the basis of their "molecular signatures" (i.e. their shape) (Medalia et al., 2002). This approach is often referred to as "template matching" (Frangakis et al., 2002; Bohm et al., 2000), which is a generic tool that can be utilized to detect characteristic shapes corresponding to known molecular machines. Unfortunately, template matching is not applicable to molecules that are smaller than 200 kD, to molecules with indistinguishable shapes, and to molecules that are buried in larger aggregates.

Acceptable preservation of the cellular architecture and molecular make-up can also be obtained by means of freeze-substitution (a procedure that replaces at low temperature (-80 °C to -90 °C) the cellular water by an organic solvent (Schwarz et al., 1989)). The solvent can contain chemical fixatives to stabilize the biological structures, and heavy atoms like uranium and osmium to give contrast to the sample before it is embedded in a resin matrix. If it is not a prerequisite that structures can be imaged up to the molecular resolution, the vitrification step may be replaced by chemical fixation with aldehydes.

Thus the specific morphological question defines the type of sample preparation and the choice of image acquisition parameters (e.g. type of microscopy and amount of electron dose). An alternative to template matchingfor the localization of structures in frozen-hydrated sections is labeling of the molecule of interest with antibodies. In this approach, a high-density tag (e.g. a gold particle) is indirectly bound to an antibody that has specific affinity for the macromolecule of interest. In general, immuno-based detection of molecules is applied to stained, resin-embedded sections. To optimize the performance of the labeling, the probe should be small to avoid problems due to limitations in penetration and sterical hindrance. In contrast, to optimize the performance of the imaging, the probe should be large and of a high-density material to enable its detection with Bright Field-TEM (BF-TEM). For instance, ultra-small gold labels (e.g. 1.4 nm Nano gold particles) are highly suitable for labeling but prove to be difficult, if not impossible, to detect using BF-TEM imaging. Moreover, these small labels are difficult to pin-point in a 2D image of a resin-embedded and stained biological section, due to the presence of flakes of stain in the specimen (about 0.5 nm in size) which generate similar small 'dark' spots in a BF-TEM image. Therefore, the direct (visual) detection in BF-TEM tomograms is a great challenge due to relatively high content of noise in a tomogram, which can obscure the label. In this context, "noise" does not refer to electron shot noise or electronic amplifier noise, but to the cellular "background structure" of the stained cytoplasm.

To enhance contrast the 1.4 nm gold labels are often amplified to larger (10-20 nm) particles using a chemical silver or gold enhancement procedure. Unfortunately, this amplification step is difficult to control and can result in heterogeneous particle sizes. These practical drawbacks of ultra-small gold labeling in sections led us to the question if a more sensitive imaging technique could be developed and optimized that allows for the direct visualization of 1 nm gold particles in a 200-500 nm thick section. A TEM imaging technique that has favorable specifications for this purpose is Scanning Transmission Electron Microscope (STEM) microscopy, in combination with a high angle annual dark field (HAADF) detector *(Monson et al., 1987; Stierhof et al., 1992)*.

In material research STEM is already known to be an invaluable tool for the analysis of the structure and chemistry of materials at high spatial resolution *(Pennycook et al., 1999)*. Due to the fact that the signal in HAADF-STEM is proportional to the square of the atomic number ($Z^2$), the method is well-suited for the detection of heavy atoms, in particular small particles like ultra-small gold *(Otten et al., 1992)*.

Moreover, with state-of-the-art instrumentation there is no need for compromise in terms of resolution when using the STEM imaging mode instead of the TEM imaging mode. The resolution in HAADF-STEM microscopy depends on the probe size, and can be expressed as the convolution between the object function of the specimen and the shape of the probe used to analyze it *(Loane et al., 1992)*. Furthermore, on judging the image formation properties, HAADF-STEM imaging should outperform BF-TEM for those questions where contrast is more important than resolution, as for example in the detection of small gold labels, or the imaging of stained and even unstained samples *(Carlemalm et al., 1982;Ohtsuki, 1980;Milligan et al., 1990; Otten et al., 1992)*. Besides resolution and contrast, another advantage of STEM over TEM is the efficiency in collecting spatial information of the specimen to provide complementary structural information. Apart from collecting highly scattered electrons with the HAADF detector, which provides an image optimal for detecting differences in atomic weight (Z), additional detectors are available simultaneously, such as Bright Field (BF), Dark Field (DF), Secondary Electrons (SE), Energy Dispersive X-ray (EDX) and Electron Energy Loss Spectroscopy (EELS) detectors. Although up to now these signals have not been acquired simultaneously, each can contribute potentially important spatial and structural information of the sample. For instance, EDX and EELS are useful signals for the detection of small gold, or for the distinctions between gold, silver or other elements, or to measure the thickness of the specimen *(Midgley & Weyland, 2003)*.

During the last few years, HAADF-STEM tomography is becoming an important tool for material science research [Ziese et al., 2002; Midgley et al., 2003; Arslan et al., 2005]. Recently, it was demonstrated that STEM-tomography has the capability to achieve 1 nm resolution for material science samples [Arslan et al., 2005; Midgley et al., 2001]. In contrast to the field of material sciences, STEM-tomography has not yet become a mainstream technique for the life sciences. To our knowledge, the first application of STEM for 3D imaging of very thick (>1 µm) stained sections was reported by Beorchia et al. 1993. Since then, few examples of STEM imaging on stained resin-embedded sections have been published [Ziese et al., 2002; Beorchia et al., 1993; Midgley et al., 2001].

In 2002, Ziese et al. discussed the possibilities and use of STEM tomography for imaging stained sections. It was demonstrated that gold particles of approx. 0.8 nm in diameter (located on the surface of the section) could be imaged using HAADF-STEM. While the obtention of 3D structural information is within the reach of BF-TEM tomography, the study of Ziese et al. [Ziese et al., 2002] demonstrated that HAADF STEM tomography is possibly more sensitive, thereby enabling the visualization of structural detail at the finest level. Equivalent tilt series were acquired from Epon embedded specimens using both BF-TEM and HAADF-STEM modes. Their result showed that, whereas general structure of biological material is resolved in both reconstructions, the HAADF-STEM imaging and 3D reconstruction revealed higher contrast and a better signal to noise ratio (SNR).

In the present paper, we computed HAADF-STEM tomograms from biological specimens and compared them with BF-TEM tomograms. A quantitative measure is necessary to compare electron tomograms recorded by various methods. Unfortunately, a straightforward resolution measure is not available for electron tomograms. Moreover, the complex relationships between the anisotropic resolution, the experimental parameters that describe the missing wedge, the angular sampling distance, the limiting total electron dose, the restricted number of 2D images, and the possible specimen damage inferred by the electron beam, complicate the formulation of a theoretical measure even further.

We decided to compare BF-TEM and HAADF-STEM tomography using three criteria. First, as a basis for comparison, we chose the same imaging parameters for BF-TEM tomography as we used in many of our tomography studies. Therefore, we compare BF-TEM and STEM images on the basis of an equal total electron dose. Second, we measured straightforward statistical parameters (signal-to-noise ratio and contrast) of well-defined visible features in the tomograms compared to their environment. Third, we used template matching [Frangakis et al., 2002;Bohm et al., 2000] to annotate membranous structures in the tomograms of the stained sections [Lebbink et al., 2007] and compared the amount (volume) of detectable membranes in the tomograms produced by BF-TEM and HAADF-STEM. This quantitative measure of recognized volume gives an objective measure for the effectiveness of each imaging mode.

## 4.2. Materials and methods

### 4.2.1. Cell culture

Human umbilical vein endothelial cells (HUVECs) were isolated and grown on culture dishes or Costar 3414 filters (Corning Inc, Corning NY, USA) as described before [Eman et al., 2006]. Normal rat kidney (NRK) cells were grown as described before [Trucco et al., 2004].

### 4.2.2. Pre-embedding labelling with BSA gold

To induce a 3D intracellular gold label, HUVECs were washed with serum-free medium and incubated for 10 min with a 5nm gold-BSA solution in serum free RPMI medium containing 0.5% FCS (Gibco, Invitrogen Corp., UK), as described before for other cell types [Möbius et al., 2003;Kleijmeer et al., 1997].

### 4.2.3.Chemical fixation

HUVECs were chemically fixed for 1–2 h in a solution of 2% formaldehyde and 0.2% glutaraldehyde in 100 mm HEPES (2-[4-(2-hydroxylethyl)-1-piperazinyl] ethansulphonic acid) at 37 °C *(Griffiths, 1993)*. After washing in distilled $H_2O$, the samples were gradually dehydrated in 50%, 60%, and 70% aqueous ethanol (10 min each), then in 80% and 90% (20 min each), and finally in anhydrous ethanol for 30 min followed by Epon embedding. Epon sections were cut at 250 nm and collected on 50-mesh formvar-coated copper grids. Sections were post-stained with 20% (w/v) methanol uranyl acetate for 5 min and with lead citrate *(Reynolds, 1963)* for 3 min at room temperature. The specimens shown in figures 4.2 and 4.3 were prepared using chemical fixation.

### 4.2.4. High-Pressure Freezing /Freeze Substitution and staining

High-pressure frozen and freeze-substituted (HPF-FS) HUVECs were prepared as described before *(Murk et al., 2003)*. HPF was done without any cryo protectant and in the presence of medium only. Briefly, after the cells were cryo-immobilized by HPF they were transferred into microtubes containing a precooled substitution fluid (at -90°C) of 2% uranyl acetate and 2% osmium tetroxide in anhydrous acetone. After overnight substitution at -90°C, uranyl acetate was washed away with anhydrous acetone. Finally, the tubes were transferred into a 1.5-ml microtube containing anhydrous acetone supplemented with 0.5% osmium tetroxide. Substitution lasted for another 24h before the samples were warmed up (1°C per hour) to -30°C, where they remained for 8h before transferring them to ice at 0°C for 1h *(Wild et al., 2001)*. Thereafter, the substitution fluid was washed away by anhydrous acetone and subsequently filters with cells were embedded in Epon. After Epon polymerization, chemically fixed and HPF-FS specimens were cut at 250 nm and collected on 50-mesh formvar-coated copper grids. Sections were post-stained with 20% (w/v) aqueous uranyl acetate for 5 min and with lead citrate *(Reynolds, 1963)* for an additional 3 min at room temperature. Before BF-TEM and HAADF-STEM data acquisition 15-nm goat anti-rabbit immuno-gold particles (Aurion, Wageningen, The Netherlands) were absorbed to the sections for 10 min. The specimen shown in figure 4.4 was prepared using high pressure freezing and freeze-substitution.

### 4.2.5. HAADF-STEM and BF Tomography

STEM and TEM data collection was performed on a 200-kV Tecnai 20 transmission electron microscope (FEI Company, Eindhoven, The Netherlands) with a Field Emission Gun (T20-FEG) and a Twin objective lens. The sample was mounted in a high-tilt specimen holder (Fischione type 2020, Fischione Instruments, Pittsburgh, USA).

BF-TEM single axis tilt series were acquired from -70° to +70° at 1° increment with an objective aperture of 40 µm. Images were recorded with a CCD camera (Gatan Inc, model 694). The full frame CCD chip contained 2048×2048 pixels of 14 µm. At a nominal magnification of 13500, and with binning 2 of the pixels on the chip, the calibrated pixel size was 1.58 nm. The tomographic tilt series were acquired automatically with the program Xplore3D (FEI Company, Eindhoven, The Netherlands). The sections were pre-irradiated to avoid shrinking effects during recording *(Luther, 1992)*. The electron dose was $1.4x10^3$ $el^-/nm^2$ for every image in the tilt series.

For the STEM data acquisition on the T20-FEG we chose an extraction voltage of 3.6 kV, gun lens setting 7, spot size 6, and a 70-µm C2 condenser aperture. These settings corresponded to a spot size of approximately 1.96 nm. The STEM single axis tomographic tilt series were acquired automatically, including focusing and image shift correction, with Xplore3D. Projection images were recorded with the on-axis HAADF detector for tilt angles from -70° to +70° (1° increment). At a nominal magnification of 56,000×, the calibrated pixel size was 1.96 nm. With a dwell time of 8 µs/pixel (10 s/image), the electron dose corresponded to $1.4x10^3$ $el^-/nm^2$ for each tilt increment, resulting in a total dose for a tilt series of $2.00x10^6$ $el^-/nm^2$. The

camera length was set at 120 mm to ensure detection of merely incoherently scattered electrons in HAADF-STEM imaging. BF and DF images were taken under the same imaging conditions as for HAADF-STEM with the only difference that the camera length was 50 mm to provide the collection efficiency.

For the alignment and reconstruction of the TEM and STEM tilt series we used the IMOD package [Kremer et al., 1996], which is based on using fiducial markers for alignment and resolution-weighted backprojection for reconstruction.

### 4.2.6. Measurement of STEM spot-size

In incoherent imaging like HAADF-STEM the total number of high-angle scattered electrons determines the image intensity of a pixel. Therefore, the HAADF image formation can be described as a convolution of the intensity distribution of the incident probe with the appropriate cross-sections for the high-angle scattering processes. Because of the highly localized nature of the high-angle scattering processes, the resolution of HAADF images is determined by the size of the incident coherent electron probe. Since the electron probe size has such a great influence on the resolution, we measured the probe diameter prior to the STEM image acquisition. We chose the probe size to commensurate with the sampling distance during scanning (i.e. the pixel size in STEM). As a measure for the probe size, we took the full width at half maximum (FWHM) of the probe intensity profile. The FWHM was measured by imaging the electron spot on the CCD camera and measuring the intensity profile with Digital Micrograph (Gatan Inc., Abingon, UK). For the STEM imaging conditions with spot size 6 the FWHM was equal to 1.96 nm.

### 4.2.7. BF-TEM/HAADF-STEM Electron Dose

To be able to compare HAADF-STEM and BF-TEM imaging, we chose to image with the same electron dose (El.D.) conditions. The measure of the El.D. in the BF-TEM imaging mode was provided by the Low Dose settings of FEI's microscope operating software that is based on the electric current of the fluorescent screen induced by the electron beam.

$$\text{El. D} = \frac{2.15 \times \text{emulsion}}{\text{exp osure time}} \times \frac{(\text{counts/sec}) \times \text{dwell time}}{\text{area of electron probe}}$$

In order to obtain the relatively small El.D. for STEM we had to compromise on extracting voltage, which reflected on exposure time, and dwell time. Therefore we used an extraction voltage of 3.6 kV and an exposure time of 5.1 sec. Since we measured exposure time on the small focusing screen of the microscope we had to correct for the sensitivity of that screen, which was in our case equal to 21. The dwell time was 8 x $10^{-6}$ sec for a probe size of 1.96 nm.

Following FEI calibration, the electron dose was equal to 1.4x$10^3$ $el^-/nm^2$.

$$\text{El. D} = \frac{2.15 \times 4 \cdot 10^{-6}}{5.1 \times 21} \times \frac{0.625 \cdot 10^{19} \times 8 \cdot 10^{-6}}{2.88}$$

For both TEM and STEM modes, the El.D. was set to 1.4x$10^3$ $el^-/nm^2$ per image in a tilt series. The procedure for the HAADF-STEM tilt series acquisition was as follows. First, at low magnification (3000 x), the area of interest was located using the BF-TEM imaging mode. Next, again in BF-TEM mode, the area was pre-radiated for 20 min to prevent shrinkage of the section during data collection [Beorchia et al., 1993]. Next, the STEM tilt series were recorded, using the low dose imaging feature of the automated software that ensured that the (automated) focusing was performed on a different area of the specimen than the area used for data acquisition.

### 4.2.8. Contrast and SNR measurement

As one of the criteria to compare the various tomograms, we defined a measure for contrast and a measure for signal to noise ratio (SNR). In our measurements we assumed that the contribution of noise by the detector to the signal was negligible. This assumption is valid because of the inherently high-contrast of the metal-stained specimen we discuss in this manuscript, in combination with the relatively high (that is, compared to low-

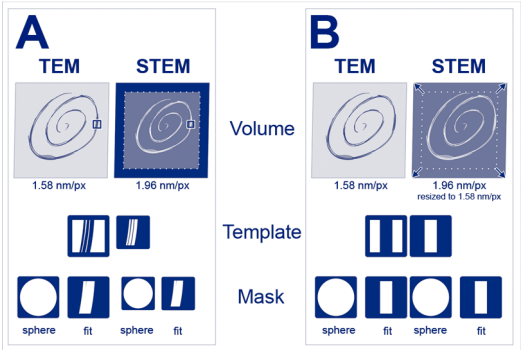


**Figure 4.1. Schematic description of how the input files for template matching were pre-processed.** *(A) Magnification scaling of TEM and STEM tomograms by cropping the STEM tomogram to the same size as the TEM tomogram. The same area containing a piece of membrane was cut out and a binary representation was used as a template for each volume. Both a spherical mask, and a fitting mask (exceeding the template by two pixels on either side) were used. (B) Magnification scaling by adapting the pixel-size of the STEM to that of the TEM tomogram. The pixel size of the STEM tomogram divided 1.24 fold (1.96/1.58), and the same digitally generated template (with a membrane thickness of 6 pixels) was applied to both tomograms.*

dose cryo imaging) electron dose we used. Related to the relatively high-dose imaging we discuss, we define as the "noise" term not the electron shot noise or the electronic amplifier noise, but the visible "background" structure of the stained cytoplasm adjacent to the membrane.

The contrast of a stained piece of membrane ($C_m$) is defined as $C_m = (I_m\text{-}I_b)/I_b$, with Im the mean (average) intensity of the piece of membrane and Ib the mean intensity of the plastic area (background). The signal to noise ratio of the membrane (SNR) is defined as $SNR_m = sd_{(I_m\text{-}I_b)}/sd_{I_b}$ with $sd_{I_b}$ the standard deviation of the background. The STEM images were acquired with the waveform just fitting the full analog-to-digital converter (ADC). A threshold was applied to the TEM images at the min and max of the histogram. Since the measure of the signal to noise ratio is a relative one, the results are independent of the absolute numbers of the STEM images or the TEM images. Measures for contrast and signal to noise ratio were carried out using the Priism software package *(Chen et al. 1996;Chen H et al., 1992)*.

## 4.2.9. Template matching in TEM and STEM tomograms

We used template matching as described by Frangakis et al. *(Frangakis et al., 2002)*. Recently *Lebbink et al. (2007)* showed that this technique can be used to extract computationally areas of membrane from tomograms of resin embedded structures. We used this technique as a tool to compare objectively and quantify the image quality of TEM and STEM tomograms. Using template matching, the tomograms are mathematically compared (correlated) to a template. If a feature in the tomogram is similar to the template, a high cross-correlation-value will be assigned to that location in the tomogram. Furthermore, a mask determines which voxels of the template are matched to the tomogram, and which are not. A relatively large spherical mask surrounding the template will lead to a higher cross-correlation value if in close proximity of the similarly looking feature in the tomogram no density is present *(Lebbink et al., 2007)*.

Due to a small difference in magnification between the STEM and TEM imaging mode, a correction-step had to be performed (see below). We performed two template matching procedures, one with a binary template extracted from the original tomogram and one with an artificial template. In both procedures the contrast of the TEM tomogram was inverted to white membranes on black background to increase the matching performance.

In the first procedure (figure 4.1.A) the tomograms were cropped to the same cellular region. Next, the same area of membrane was chosen on the basis of its relative position to the gold beads present in the sample. Because of the difference in magnification, this area was either 32 voxels for STEM or 36 voxels for TEM. For both templates corresponding masks were created which were either spherical (r=13 voxels for STEM and r=15 voxels for TEM) or fitting (a mask for the same shape as the template, but exceeding the structure in the template by two pixels on each side). The spherical mask was created using the TOM-toolbox *(Nickell et al., 2005)* in

MatLab (MathWorks, Natick, MA, USA). All other manipulation-steps were performed in Amira 3.1(TGS, France).

In the second procedure the resolution (1.96 nm/px) of the STEM image was adjusted to the resolution of the TEM image (1.58 nm/px) by increasing all dimensions 1.24 fold in Amira and cropping out the area present in both tomograms. The template was artificially created using the TOM-toolbox and contained a cuboid of 32x6x32 white voxels in a black volume of 32 voxels. Both a spherical mask (r=13 pixels) and a fitting mask (cuboid-shaped with a thickness of 10 voxels) were made.

Calculations were performed on 54 CPU's at the LISA-cluster of the SARA super computer facility (Amsterdam, the Netherlands). The templates were matched over 180° in φ (phi) and θ (theta) with an increment of 5°. Beyond these angles repetition of the structure occurs. Each calculation took approximately 75 minutes. The missing wedge was not taken into account in these calculations except that they are comparable in STEM and TEM under the used conditions.

## 4.3 Results and discussion

Bright-Field transmission electron tomography (BF-TEM) is a widely used technique in life sciences to image specimens in 3D. During the last five years numerous studies appeared in which tomography played a major role, and several groups are working on methods to improve the applicability and resolution of the technique *(Diez et al., 2006; Penczek et al., 2006; Lawrence et al., 2006)*.

HAADF-STEM tomography is not widely used for applications on biological specimens. A disadvantage of STEM imaging, as implemented in available microscopes, is that it is not capable of phase contrast imaging. This is one of the reasons why STEM imaging is not applicable for frozen-hydrated biological structures. On the other hand, the sensitivity of HAADF-STEM imaging to differences in atomic number (Z) represents a strong advantage. Therefore, to get better insight into the STEM technique and to determine to what extent the technique could be valuable for applications in life sciences, we focused on one potential application of HAADF-STEM: the detection of small high-density labels in a light matrix (resin). We compared the performance of BF-TEM tomography with HAADF-STEM tomography. For this purpose we have chosen several criteria for

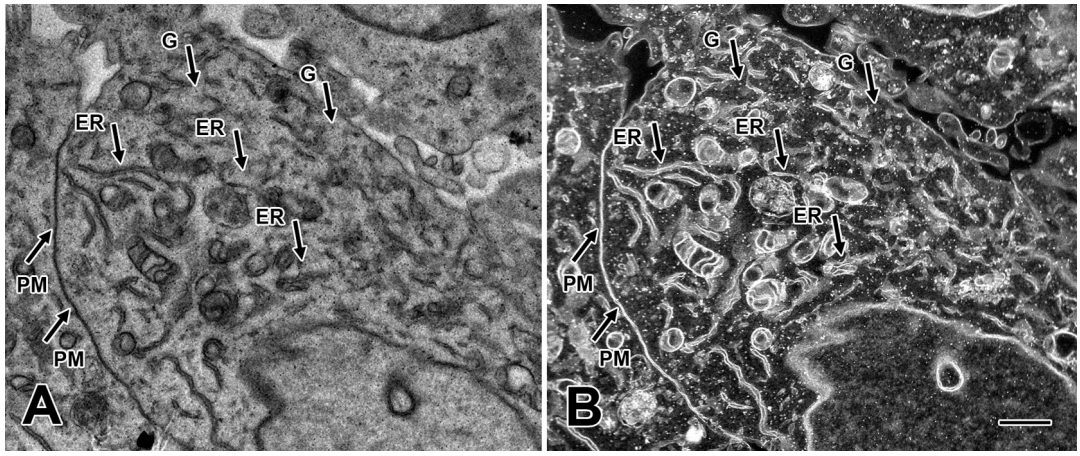


**figure 4.2. Visualization of the different structures in the images of NRK cells recorded in BF-TEM and HAADF-STEM.** *The images were recorded from chemically fixed and positively stained NRK cells in a 100 nm thick section. (A) BF-TEM image using the CCD camera taken at a magnification of 9600x, which corresponds to a pixel size of 1.61 nm on the BF-TEM. (B) HAADF-STEM image with 2000x magnification (working distance 150 µm) where the pixel size is 6.3 nm. (ER) indicates the endoplasmatic riticulum, (PM) indicates the plasma membrane, and (G) indicates a gold particle Scale bar = 1 µm*

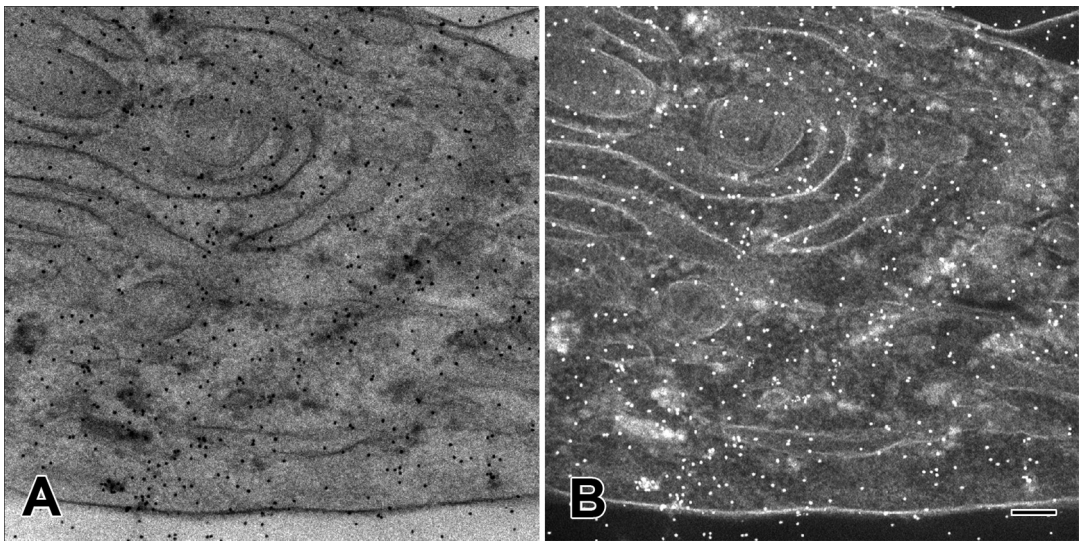


**Figure 4.3. Visualization of HUVECs in BF-TEM and HAADF- STEM mode.** *Images of chemically fixed HUVECs in a 250 nm thick section were recorded using BF-TEM (A) and HAADF-STEM (B). In both cases the specimens were positively stained. Scale bar =100 nm*



comparison, such as visual inspection, statistical analysis by measuring contrast and SNR of a feature relative to its background, and the use of template matching to determine whether features (specifically stained membranes) can be detected more effectively in a TEM or in a HAADF-STEM tomogram.

### 4.3.1. HAADF-STEM images have higher contrast and less noise

Due to the nature of HAADF-STEM image formation, we expected to obtain a higher contrast and a better signal to noise ratio in HAADF-STEM images of stained structures than in BF-TEM images. Visual inspection confirmed this notion, as is illustrated in figure 4.2, where low-magnification images of NRK cells taken in BF-TEM and HAADF-STEM modes from the same area are shown. Several features, like the plasma membrane (PM) and the endoplasm reticulum (ER) looked more pronounced with HAADF-STEM (figure 4.2.B) than with BF-TEM (figure 4.2.A). Striking was the appearance of the 15 nm gold particles (*G*) that were very clear in the HAADF-STEM images, compared to the BF-TEM images where they were hardly visible. Since HAADF-STEM collects a signal that is related linearly to the scattering power of the sample, and is free of the Fresnel fringes that are characteristic for coherent axial bright-field images *(Engel et al., 1974)*, the high density material of the gold and stain is imaged with higher contrast than with BF-TEM. The lack of possible phase-reversals related to BF-TEM imaging with phase contrast, the linearity, and the high SNR provided by the HAADF detector, lead to images that are straightforward to interpret.

A second example where an area of a specimen is imaged with both HAADF-STEM and BF-TEM is shown in figure 4.3. In this case we imaged a 250nm thick section of Epon embedded HUVECs.

By visual inspection of the HAADF-STEM image (figure 4.3.B) there seemed to be less difference with the BF-TEM image (figure 4.3.A) than was the case in figure 4.2. However, we found that the stained membrane structures imaged with HAADF-STEM appeared less noisy and seemed to have higher contrast than with BF-TEM. To quantify the differences between BF-TEM and HAADF-STEM, we applied two methods (see materials and methods). We summarized the findings in Table 4.1. First, we measured the contrast and

Table 4.1. Contrast and SNR in HAADF-STEM and BF-TEM images computed for stained membranes.

| | HAADF-STEM | | BF-TEM | |
|---|---|---|---|---|
| | Contrast | SNR | Contrast | SNR |
| Membrane | 0.66±0.1 | 8.87±1.32 | 0.12±0.02 | 5.00±0.78 |
| El.D $\times 10^3$ $el^-/nm^2$ | 1.4 | | 1.4 | |

*The standard deviation was determined by measuring 10-12 areas within the corresponding images.*

signal to noise ratio (SNR) of features of interest in the zero tilt image of the tilt series recorded in HAADF-STEM and BF-TEM. Second, we applied template matching to determine if stained features are visualized more clearly with HAADF-STEM than with BF-TEM.

As shown in Table 4.1, the membrane contrast in a HAADF-STEM image (0.66) was five times higher than the membrane contrast in a BF-TEM (0.12) image. The SNR of the membrane in the HAADF-STEM image (8.87) was higher than the SNR measured in a BF-TEM (5.0) image. This indicates that the HAADF-STEM images of stained sections have a higher contrast and are less noisy than images recorded with BF-TEM mode, using a similar electron dose. Similar results were obtained when the calculations were carried out on the zero tilt images of other tilt series, or on high-pressure frozen and freeze substituted HUVECs (data not shown). The measurements were repeated 20 times, and on 10 different features. The increase in contrast can be explained by the high angle scattering related to the atomic number ($Z$) of the high-density stains. Another contribution to the higher contrast of the HAADF-STEM images comes from the absence of chromatic aberration in that imaging mode. Especially at higher tilts, e.g. at 70 degree specimen tilt of a 250 nm thick specimen, this contribution will be noticeable.

It is important to keep in mind that these conclusions on the increase of contrast depend heavily on the microscope conditions used, such as electron dose, size of the different apertures, CCD camera sensitivity in TEM imaging mode, gun lens size, dwell time and camera length in STEM imaging mode. Therefore these calculations are only relevant for the conditions used in this study. For a fair comparison we chose the conditions so that for a certain pixel size the El.D. was comparable for TEM and STEM mode.

### 4.3.2 More information extracted from HAADF-STEM tomograms

So far we looked at plastic sections of biological material, which showed a significant improvement in SNR and contrast in HAADF-STEM images compared to BF-TEM images. However, on visual inspection there seemed to be not a significant difference in the level of detail that could be observed with HAADF-STEM imaging (figure 4.3) compared to BF-STEM. Nevertheless, HAADF-STEM tomograms (figure 4.3) showed some features that were not visible in BF-TEM tomograms.

Figure 4.3.A and B show similar areas from BF-TEM HAADF-STEM and HAADF-STEM tomograms. The total electron dose exposed to the sample in HAADF-STEM was the same as for BF-TEM. The tilt series with TEM and STEM imaging mode were run separately. The TEM series was collected first, followed by the STEM series. In optical sections through the HAADF-STEM tomograms (figure 4.3.B) there was no visible beam damage although the acquisition time for a HAADF-STEM tilt series (appr. 2 h) was about four times longer than for BF-TEM (appr. 40 min). To the eye, the noise level in a HAADF-STEM optical section was significantly lower than in its TEM counterpart. This visual notion was confirmed by the measurements of contrast and SNR (results not shown). Even though most features, like the 5nm gold particles (G), the PM, the ER and

the mitochondrial membrane (MM) were visible in both tomograms, the HAADF-STEM tomograms displayed a higher contrast and revealed details that were hardly visible in the TEM counterparts. For instance, the MM was more clearly visible and the cytosolic proteins were more prominent in the STEM image (arrow head figure 4.4.B).

### 4.3.3. Template matching shows better resolved membranes in HAADF-STEM tomographic reconstructions

To compare the performance of HAADF-STEM tomography with TEM tomography in a quantitative manner template matching was applied. Both a binary template extracted from the original tomograms, and a single artificial (i.e. computer generated model) cuboid-shaped template were used. In case of the cuboid-shaped template we adjusted the magnification of the HAADF-STEM tomogram (1.96nm/px) to the TEM-tomogram (1.58nm/px) to correct for the difference in magnification. This correction was not performed in case of the extracted template, because such a magnification-correction is already contained in the template itself.

In the cross-correlation files we looked at three different parameters: maximum fit, the range of the optimal threshold of correlation, and the amount of fitted cubic nanometer of membrane. We compared these parameters for HAADF-STEM and TEM template-matched reconstructions. The first parameter was the maximum fit which is defined as the highest cross-correlation obtained by template matching. The higher this value, the closer the structure detected in the volume resembled the structure contained within the template. Since the same biological sample was used for both HAADF-STEM and TEM, differences in this value have to be related to differences in the image formation mechanism as well as the alterations caused by the acquisition. One important factor is the level of background, for instance randomly distributed speckles or image intensities that makes it more difficult to track membranes. In all cases, the max fit in HAADF-STEM was approximately 15% higher than in TEM, indicating that in HAADF-STEM the background was less disturbing in the reconstruction (Table 4.2, max fit).

The second parameter was the range of the optimal threshold of correlation (OTC), which indicates how well the structure could be distinguished from

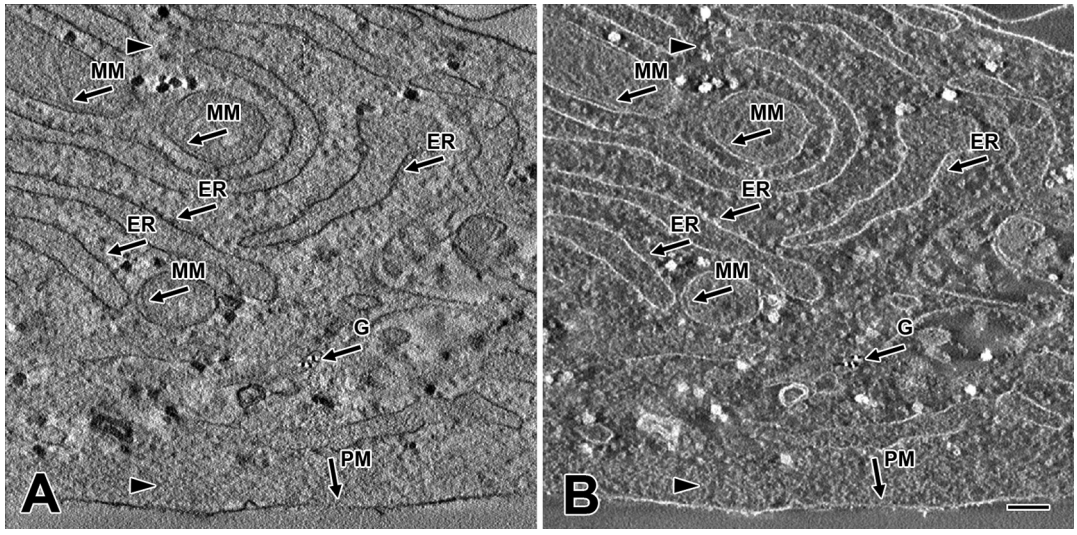


**Figure 4.4. Reconstruction slices from the 3D reconstruction calculated from the BF-TEM (A) and HAADF-STEM (B) projection images.** The slices are 70nm thick. PM indicates plasma membranes, ER indicates endoplasmic reticulum, G indicates 5nm BSA-gold particle, MM indicates mitochondrial membrane, and arrow-heads indicate cytosolic membrane. Scale bar =100 nm

the background. The smaller the range, the less the structure could be exclusively extracted. The OTC is defined as the lowest cross-correlation value at which no false positive matches are observed, and thus a maximum of exclusively and correctly matched structures is segmented [Lebbink et al. 2007]. False positives are defined as locations in the tomogram that are incorrectly interpreted as a structure similar to the template. This value was obtained manually by visual inspection. To correct for the differences in max fit, we looked at the OTC value as a percentage of the max fit. We found that the relative OTC for HAADF-STEM and TEM, under the conditions used, were at approximately the same percentage of the corresponding max fit. (Table 4.2, OTC as % of max fit). We can therefore conclude that for both acquisition techniques the general structure is equally distinct from the background.

To find out if we could extract more information from the HAADF-STEM or from the TEM-tomogram, we calculated the third parameter which was the number of cubic nanometers of membrane detected by template matching at the OTC. This parameter is a marker for the visibility of each matched structure in the tomogram. Thus while the general structure can be equally distinct from the background (as shown by the range of the OTC), the visibility of individual occurrences of the structure can differ between HAADF-STEM and TEM. The better the individual visibility of the structures, the more voxels will obtain a high cross-correlation value. Our measurements show that in the HAADF-STEM tomogram 1.3 times more membrane could be detected (Table 4.2, matched $nm^3$, HAADF-STEM/TEM), indicating that within the range where the template was exclusively detected (OTC) more information was present and extractable from the HAADF-STEM tomogram than from the TEM tomogram. This increase in information was confirmed by visual inspection of the 3D isosurface representations of both the TEM and HAADF-STEM cross-correlation files with a threshold set at the OTC. Several holes present in the membrane – regions that could not be identified by template matching – in TEM are filled in the matched HAADF-STEM tomogram (figure 4.5, arrowheads).

**Figure 4.5. 3D Representation of a highlighted region of membranes matched in HAADF-STEM and BF-TEM tomographic reconstructions.** The arrowheads point to several of the regions where template matching performed better in HAADF-STEM (bottom) than in BF-TEM (top). These 3D models were created from tomographic volumes with an artificial cuboid shaped template and a mask of the same shape.

The results of the comparisons of HAADF-STEM with BF-TEM imaging are summarized in Table 4.3. Except for the data collection time, HAADF-STEM outperforms BF-TEM imaging on the criteria we used. HAADF-STEM images display almost five times better contrast and SNR than those obtained with BF-TEM. The template matching showed that in HAADF-STEM tomograms 1.3 times more membranes can be detected than in BF-TEM tomograms.

Table 4.2. Comparison of template matching between HAADF-STEM and BF-TEM tomograms.

| Mode | Method | Max fit | OTC as % of max fit | Matched $nm^3$ at OTC | HAADF – STEM / BF – TEM |
|---|---|---|---|---|---|
| *HAADF-STEM* | Extracted template fitted mask | 0.683 | 41 | $4.5 \cdot 10^6$ | 1.36 |
| *BF-TEM* | | 0.578 | 39 | $3.3 \cdot 10^6$ | |
| *HAADF-STEM* | Extracted template spherical mask | 0.799 | 51 | $3.4 \cdot 10^6$ | 1.34 |
| *BF-TEM* | | 0.675 | 51 | $2.5 \cdot 10^6$ | |
| *HAADF-STEM* | Artificial template fitted mask | 0.746 | 46 | $3.7 \cdot 10^6$ | 1.33 |
| *BF-TEM* | | 0.542 | 43 | $2.8 \cdot 10^6$ | |
| *HAADF-STEM* | Artificial template spherical mask | 0.858 | 61 | $3.1 \cdot 10^6$ | 1.32 |
| *BF-TEM* | | 0.720 | 58 | $2.3 \cdot 10^6$ | |

The column 'Mode' shows which acquisition technique was used (HAADF-STEM or BF-TEM). 'Method' shows which template-mask combination was used. 'Extracted template' indicates that the template originated from a cropped region of the tomogram, from which a binary representation was used as template. 'Artificial template' indicates that an artificial cuboid-shaped template was used, while the volume of the HAADF-STEM was resized to match the volume of the BF-TEM tomogram Two distinct mask-shapes were used: one was identical to the structure in the template, but exceeding this structure by two pixels on either side ('Fitted mask'), the other was spherical ('Spherical mask'). The column 'max fit' shows the highest correlation value obtained by template matching. This is an indication of the influence of background; a higher max fit means less background. The optimal threshold of correlation (OTC) as a percentage of the highest correlation value is shown in the column 'OTC as % of max fit'; which describes how well the structure can be distinguished from the background. A lower value indicates that it was easier to make that distinction. In the column 'matched $nm^3$ at OTC' we show the number of cubic nanometers of membrane that could be extracted from the tomogram using template matching (without extraction of background). This value is compared between HAADF-STEM and BF-TEM in the final column 'HAADF-STEM/TEM', where the number of $nm^3$ matched in the HAADF-STEM tomogram was divided by the value of the $nm^3$ matched in the corresponding BF-TEM. Values larger than 1 indicate better matching results for HAADF-STEM than for BF-TEM.

## 4.4. Conclusions

In contrast to TEM imaging, STEM imaging allows simultaneous collection of signals that arise from the electron-specimen interaction, such as BF, DF, and HAADF. We demonstrate that HAADF-STEM tomography is a powerful tool to study stained biological specimens. Compared to TEM tomography, HAADF-STEM tomography yields better contrast and better SNR using the same electron dose. The better performance is important for the detection of small gold-beads in thick sections as is the case in 3D immuno-labeling experiments.

Table 4.3. Performance comparison between HAADF-STEM and BF-TEM tomography.

| | HAADF-STEM | BF-TEM |
|---|---|---|
| *Tilt series time acquisition* | 2 h | 40 min |
| *Contrast* | 5.05 | 0.4 |
| *SNR* | 15.49 | 3.8 |
| *Matched $nm^3$* | $4.5 \cdot 10^6$ | $3.3 \cdot 10^6$ |
| *Pixel size* | 1.96 | 1.58 |
| *El.D.$\cdot 10^3$ el/$nm^2$* | 1.4 | 1.4 |

STEM tomography may be used as a complementary technique to TEM tomography. The data collection speed with TEM-tomography is faster and provides very useful tomograms for a variety of applications. Nonetheless, data collection with STEM is fast and reproducible. Moreover, due to the increased contrast in the HAADF-STEM imaging mode, it may be a useful method for imaging stained, and most likely also unstained specimens containing DNA or RNA with small density differences to protein, and for the detection of small heavy atoms, like ultra small gold particles used with immuno-labeling.

To compare tomograms produced by the two imaging modes, we quantified numbers for the contrast and signal to noise ratio, but also for the amount of detectable structures using template matching. For the imaging conditions used, HAADF-STEM tomograms provide stained structural arrangements such as membranes with better detectable detail than with a TEM tomogram taken under similar imaging conditions.

Based on these observations we conclude that STEM tomography can be a very useful 3D imaging tool besides TEM tomography when finest structural detail in stained sections has to be detected.

## Acknowledgements

We would like to thank Alexander Mironov for providing the NRK sections as described in Materials and Methods. We also would like to thank Montserrat Barcena for constructive discussions on HAADF-STEM image formation and aspects of reconstruction. We would like to thank Jack Valentijn for the critical reading of the manuscript. This research has been made possible by the Dutch IOP genomics project IGE03012 and the Cyttron consortium.

# CHAPTER V

## induced membrane domains as visualized by electron tomography and template matching

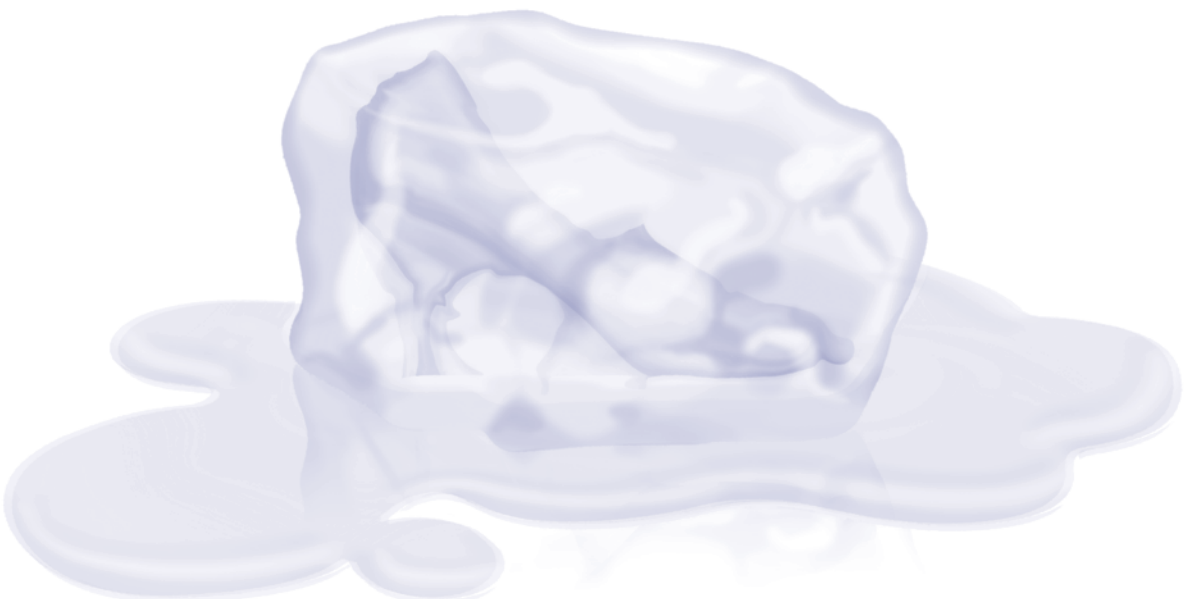

# induced membrane domains as visualized by electron tomography and template matching

M.N. Lebbink[o] • E. van Donselaar[o] • B.M. Humbel[o]
L.O. Herzberger[i] • J.A. Post[o] • A.J. Verkleij[o]

[o] *Cellular Architecture and Dynamics, University of Utrecht, the Netherlands*
[i] *Department of Computer Science, University of Amsterdam, the Netherlands*

Honest differences are often a healthy sign of progress.

*Mahatma Gandhi*

Published in *Journal of Structural Biology*
**166**: 156-161 *(2009)*

Membranes play a crucial role in many cellular processes, and it is therefore not surprising that many electron tomographic studies in life sciences concern membranous structures. While these tomographic studies provide many new insights into membrane connections and continuities in three dimensions, they are mostly limited to a macro-morphological level. In this article we demonstrate that by combining electron tomography and three dimensional template matching we are able to investigate membrane morphology at a new level: membrane domains in three dimensions. To test this, temperature induced lipid phase separation in the outer membrane of *Escherichia coli* was studied . We compared the inner (containing phosopholipids) and outer (containing lipopolysacharids) leaflet of the *Escherichia coli* outer membrane at both 37ºC and -20ºC, and could visualize how these leaflets react differently to temperature shifts. These findings can be explained by the physico-chemical nature of the building blocks and are in line with earlier published data. The present study shows for the first time, that the combination of electron tomography and template matching is robust enough to visualize existing membrane domains that are beyond the perception of manual annotation.

## 5.1 Introduction

Many biological studies directly or indirectly focus on increasing our understanding of the architecture and dynamics of cellular – or multi-cellular – systems. This is done either from a fundamental point of view to increase our knowledge of the organization of life, or based around a more applied question like for example gaining insight into the disturbances that lead to diseases. In recent years electron tomography has become increasingly important to our understanding of the cellular organization in three dimensions and has shown particular strength in revealing membrane connections and continuities both within and between organelles [Mannella et al., 1998; Geuze et al., 2003; Marsh et al., 2004; Trucco et al., 2004].

While the value of electron tomography in macro-morphological studies is undisputed, the question can be raised whether the same technique can also be used to investigate subtle local differences within membranes. To investigate this, three things are required: a biological model system in which subtle differences (domains) can be induced in the membrane, a preparation method that successfully preserves such subtle differences without redistribution or obscuration, and a detection method that is robust enough to extract these subtle differences from the acquired tomographic volumes.

As a model system, we decided to use temperature induced lipid phase separation. Lipid phase separation occurs as a physical property of mixed lipid membranes in which differences in phase transition temperatures causes the lipids to sort into liquid and solid domains. This lipid separation has a huge effect on the distribution of proteins, which are 'squeezed' into the liquid areas, and thus depleted from the solid regions. The biological model system used in this paper to investigate this property is the *Escherichia coli* bacterium. Domain formation by lipid phase separation in the *E. coli* membrane has been extensively studied and was clearly shown using freeze fracture techniques [Verkleij & Ververgaert, 1975; Verkleij et al., 1977]. The decision to examine specifically the outer membrane of the *E. coli* rather than the plasma (or inner) membrane was made for practical reasons; unlike the outer membrane, the visibility of the plasma membrane was obscured by the cytoplasm, making it difficult to distinguish it from the background. Furthermore, unlike the inner membrane, the outer membrane building blocks distribution is highly asymmetrical; having an outer leaflet composed of lipopolysaccharide (LPS) and an inner leaflet consisting of phospholipids [Reeves et al., 1996; Raetz & Whitfield, 2002]. While temperature induced lipid phase separation occurs greatly in phospholipid based membranes, LPS based membranes are largely unaffected [Overath et al., 1975; Rottem & Leive, 1977], giving us an internal control to ascertain that the membrane itself is not disrupted by the process.

Cryo-fixation techniques like high-pressure freezing (HPF) are generally accepted to fix the sample instantly, while preserving ultra-structural details. The use of stain can be a complicating factor, since the molecular nature of staining methods is not fully understood. Nevertheless, stain deposition is directly affected by the composition of a membrane, and it can be assumed that alterations in its local composition will increase or decrease local staining. Consequently, it can be expected that the visibility of local differences in composition (domains) are not obscured, but rather enhanced in a stained sample.

The third requirement is a method that could (semi) objectively extract subtle differences within a membrane from electron tomographic volumes. In our previous article we already hinted on the possibility of using three dimensional template matching as developed by Frangakis et al. for this task (Frangakis et al., 2002, Lebbink et al., 2007); here we further explore this approach.

In this paper, we study a controlled biological system where membrane domain formation is induced by incubating *E. coli* for fifteen minutes at minus twenty degrees Celsius prior to high-pressure freezing. We demonstrate, that by combining electron tomography and template matching we are able to (semi) objectively extract information from tomographic volumes that lies beyond the possibilities of manual annotation, and cannot be extracted by eye alone.

## 5.2. Material and Methods

### 5.2.1 Sample Preparation and Electron Tomography

*E. coli* (*NCCb 2399* aka *CE1052* strain (Verkleij et al., 1977)) were grown overnight on LB-agar plates at 37ºC. The cells were placed at either 37ºC (control cells) or sandwiched between aluminium high-pressure freezing cups at -20ºC (lipid phase separation induced cells) for 15 minutes; while the holder and the cells were kept at either room temperature (37ºC sample) or on ice (-20ºC sample) during mounting. Thereafter the cells were immediately high-pressure frozen (Leica EMHPF, Leica Microsystems, Vienna, Austria). Next, freeze-substitution was performed in acetone containing 2% $OsO_4$, 0.2% Uranyl-acetate in acetone, and 1%$H_2O$ (Walther & Ziegler, 2002). The samples were kept at -90ºC for 48 hours, brought to -60ºC in steps of 2ºC per hour, and subsequently held at -60ºC for eight hours. They were then brought to -30ºC at 2ºC per hour and remained in the freeze-substitution unit (Leica Microsystems, Vienna, Austria) at -30ºC for eight hours. The samples were washed four times for 30 minutes in the freeze substitution machine at -30ºC with acetone containing 2% $OsO_4$ and 1%$H_2O$ to remove the Uranyl-acetate. Next, the samples were placed on ice, and the $OsO_4$ and $H_2O$ were removed by washing twice for 30 minutes with anhydrous acetone.

After freeze substitution, the cells were embedded in Epon by gradual infiltration with the resin (Mollenhauer, 1964), and subsequent polymerization for 72 hours at 60ºC. Thereafter, 150 nm thick sections were cut. These sections were put on Formfar-coated, non-carbon-coated, 50 mesh copper-grids. Next the samples were stained with uranyl-acetate (Terzakis, 1968) in methanol for 4 minutes, and Reynolds' lead citrate (Reynolds, 1963) for two minutes.

### 5.2.2 Electron Tomography

Fiducial-gold markers (5nm colloid gold) were added to both sides of the grid, and TEM projection images were taken over two perpendicular axis (double tilt (Penczek et al., 1995, Mastronarde, 1997, Arslan et al., 2006)) on a 200kV Tecnai-20 Electron Microscope (FEI company, Eindhoven, the Netherlands) from -60º to +60º with a 1º increment. The TEM-projection images were reconstructed into a double-tilt tomogram using the IMOD/eTomo package (Kremer et al., 1996). All fiducial-markers were tracked manually in each projection to assure optimal tracking resulting in optimal tomograms. The voxel-sizes of the tomograms were at 37ºC 0.82 nm/vx and at -20ºC 0.77 nm/vx. We visually compared the *E. coli* outer membrane for both conditions both in a single virtual slice as well as in twenty slices averaged into a single image using IMOD.

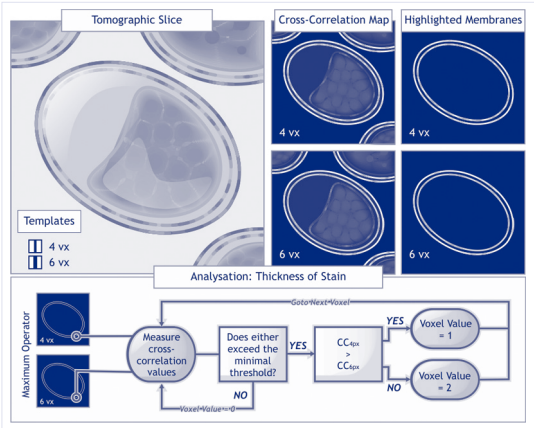


**Figure 5.1. Schematic description of the analysis process for the cross-correlation maps.** *A tomogram was matched to two templates that differed in a single property (thickness of the leaflet described within the template file). Then, background in the cross-correlation map was masked out, highlighting only the leaflets of interest (upper panel). A maximum-operator was applied to the highlighted leaflets to analyze homo- or heterogeneity in stained leaflet thickness. For each voxel the similarity between the leaflet at that location was compared to both templates, and a specific grey value was assigned depending on which template showed greater similarity as indicated by the height of the correlation value (lower panel).*

### 5.2.4 Template Matching

Template matching was performed as described by Lebbink et al. using cuboid-shaped templates of either 4 or 6 voxels thick and cuboid-shaped masks which exceeded the template-thickness by two voxels on each side (thus 8 and 10 voxels thick respectively) *[Lebbink et al., 2007]*. Calculations were performed on 54 CPU's each (SARA super-computer facilities, Amsterdam, the Netherlands). The file-dimensions were 32x32x32 voxels for both the templates and the masks. The missing wedge was not taken into account for these calculations. As described before *[Lebbink et al., 2007]*, the template was rotated (in Euler angles) for 180º over psi (ψ) and theta (θ) with an increment of 5º, and for 0º over phi (φ).

### 5.2.5 Analysis of the cross-correlation files

The cross-correlation files acquired by template matching were loaded into Amira 3.1 (TGS/Mercury, France). The separate leaflets were highlighted in a mean correlation map, averaged from both the 4 and 6 voxel correlation maps, to produce an image containing only the membrane leaflets of interest (schematically described in figure 5.1, top panel). Membrane regions of 3 different *E. coli* bacteria were matched and analysed for both conditions.

We looked whether there was a morphological difference in stained membrane thickness (figure 5.1, bottom panel). For this we use a simple maximum operator to measure for each (leaflet containing) voxel whether the leaflet at that location showed greater resemblance (having a higher cross-correlation value) to the 4 voxel thick or to the 6 voxel thick template. While we used a low threshold value (0.2) on the cross-correlation map, this did not extensively induce false positive artefacts, due to the use of highlighted leaflets. After the maximum operator, we removed small islands of voxels prior to visualising the leaflets in 3D.

To test whether the overall recognizability (matching value) of the leaflets changed at either temperature we averaged the highlighted membrane matched against 4 and 6 voxel-thick templates, and voxels were grouped in five groups based on their correlation value (supplementary figure 5.1).

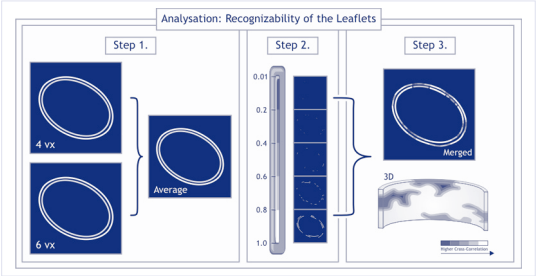


**Supplementary Figure 5.1. Schematic description of the analysis of recognizability of the leaflets.** After highlightment of the leaflets (as described in figure 5.1), the cross-correlation values for both templates is averaged to counter the effect of thickness (step 1). The averaged matching values are divided into five groups that are assigned a grey (from 1 to 5). The first group contained all voxels with a correlation value between 0.01 and 0.2, the second group the voxels between 0.2 and 0.4, the third group ranged from 0.4 to 0.6, the fourth group from 0.6 to 0.8, and the fifth group contained all voxels with a higher correlation value, up to 1 (step 2). These groups were then visualized in three dimensions using Amira (step 3).

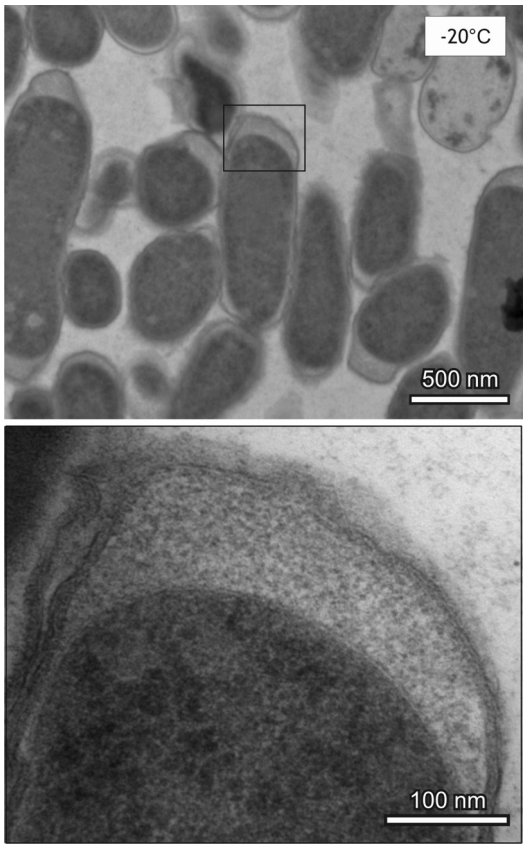


**Figure 5.2. Validation of the Freezing Process.** *To ensure that no freeze damage artefacts had occured during sample preparation we examined the sample incubated at -20ºC for artefacts caused by the formation of ice crystals. In the majority of the cells – incubated at either temperature – no artefacts were observed in either the periplasmic space or the cytoplasm.*

## 5.3. Results and Discussion

Lipid phase separation as an effect of environmental factors and membrane composition is a well-stablished phenomenon (Quinn, 1989; Williams, 1990). More than thirty years ago, the effects of temperature on the local membrane composition were already visualized on an electron microscopic level using freeze-etching (Verkleij et al., 1972). Because of the robustness of this system, it is an ideal model system to test whether temperature induced membrane domains can be observed in an Epon embedded and post-stained electron tomographic images as well.

A major risk when exposing cells to -20ºC is the formation of ice crystals and subsequently – if these crystals grow too big – damage to the sample. A general solution is the use of a cryoprotectant. However, since cryoprotectants do – in one way or another – interact with (and thus slightly change) the membrane we are investigating at an ultrastructural level, this option was not available to us. Therefore we decided not to use any cryoprotectant, and visually check whether freeze damage had occurred during preparation. Based on the absence of characteristic protein aggregation, indicative for ice crystal formation, in both the cytoplasm and the periplasmic space it can be concluded that no freezing damage occurred during the incubation step at -20ºC, the HPF and the freeze substitution (figure 5.2). Consequently, the differences observed between the membrane systems subjected to the two temperatures should be considered effects of changes within the membrane. We therefore proceeded using this approach.

By visually comparing the micrographs and electron tomograms of the *E. coli* incubated at 37ºC and -20ºC, we noticed several effects of the temperature incubation. First of all, while granulation in the stain deposition at the inner leaflet of the outer membrane was visible at both temperatures, it was more extensive at -20ºC (Figure 5.3). This increased granulation effect at -20ºC is likely due to protein aggregation caused by the lipid phase separation, since proteins are the major component involved in stain deposition at the inner leaflet. Hardly any change is observed in the outer leaflet for two reasons: first of all, the LPS-based leaflet is far less affected by lipid phase separation than it is phospholipid-based counterpart, and secondly, LPS molecules are themselves heavily stained, and a possible change in protein staining will therefore be largely obscured.

Enlargement of the periplasmic space caused by osmotic effects was observed throughout the samples incubated at both temperatures and showed no clear visual difference in size between the different samples; although individual cells were very variable in the size of the periplasmic space. For both conditions, the visibility of the inner membrane

was obscured due to its close proximity to the cytoplasm which resulted in a low contrast between the membrane and the background. The decision was therefore made to investigate the *E. coli* outer membrane.

The electron tomograms were analysed by template matching against two template files (cubes with dimensions 32 voxels) that differed in a single property: thickness of the contained structure. The artificial template files contained a simplified representation of a small piece of membrane in the shape of a cuboid of respectively 4 and 6 voxels thick. After matching, the membranes of interest were manually extracted/highlighted from the tomogram, and analyzed using a maximum operation for each voxel. Using this approach, we can visualize which template more closely resembles/fits a location on the membrane. Our results are shown in figure 5.4.

In line with freeze etching data [Verkleij et al., 1977], we observed clear domains that were variable in size in the LPS-based outer leaflet of the outer membrane. In this outer leaflet of the puter membrane no clear general differences were observed between -20ºC and 37ºC (figure 5.3, o.m.o.l. (green)). This observation is in sharp contrast to the results obtained from the phospholipid-based inner leaflet. For this condition we observed that, at 37ºC, there was an overall similarity of the entire matched region to a single template (figure 5.4), which is in agreement with a random distribution of stained proteins throughout the leaflet, as a result of diffusion of the membrane proteins within the membrane. The picture changes, however, drastically when bacteria are incubated at -20ºC for 15 minutes prior to high-pressure freezing. In the 3D representation of the template matched results (figure 5.3, o.m.i.l. (red)) a very heterogeneous image is obtained. Based on the thickness of the deposited stain, domains are observed that share greater similarity to one template, while others share greater similarity to the second template. These findings can be easily explained by the physical process of lipid phase separation, which causes proteins to aggregate within the leaflet, resulting in regions that are protein enriched and regions that are depleted of

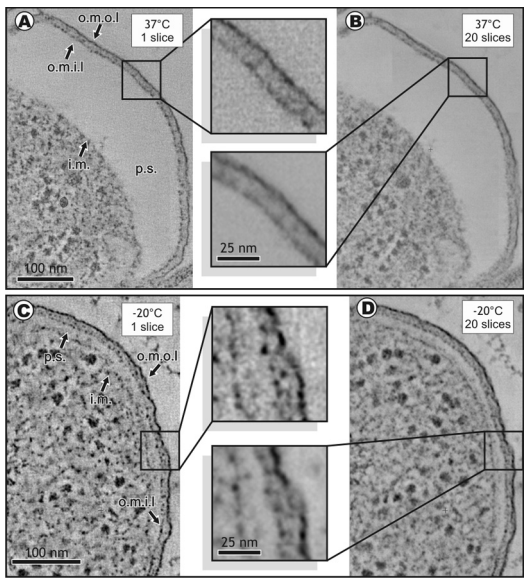


**Figure 5.3. Electron Tomography on Membranes of High-Pressure Frozen *E. coli* from Different Temperatures.** *E. coli were incubated for 15 minutes at 37ºC (figure A & B) or -20ºC (figure C & D) prior to high-pressure freezing. The inner membrane (i.m.), the periplasmic space (p.s.), the outer membrane's inner leaflet (o.m.i.l.), and the outer membrane's outer leaflet (o.m.o.l.) are indicated. Figures A and C are virtual tomographic slices of 37ºC and -20ºC respectively, while figures B and D the same regions shows in 20 merged virtual slices (using the IMOD Slicer option). An increased granulation of the inner leaflet of the outer membrane at -20ºC compared to 37ºC can be observed.*

proteins. Consequently, the deposition of stain changes drastically, since protein enriched regions will be more heavily stained than protein depleted regions. Freeze fracture data [Verkleij et al., 1977] indicates that a domain size of one to two hundred nanometres may be expected, which is the same range as the domains observed by template matching.

Since the visualization of domains due to lipid phase separation within membranes by template matching is possible, and is, for a major part, based on the staining of protein components in the membrane, the prediction is made that the membrane visibility, and thus the cross-correlation value, should be decreased in certain membrane regions. This decrease should (at least partly) coincide with the regions where stain deposition is decreased due to protein depletion. This prediction is indeed

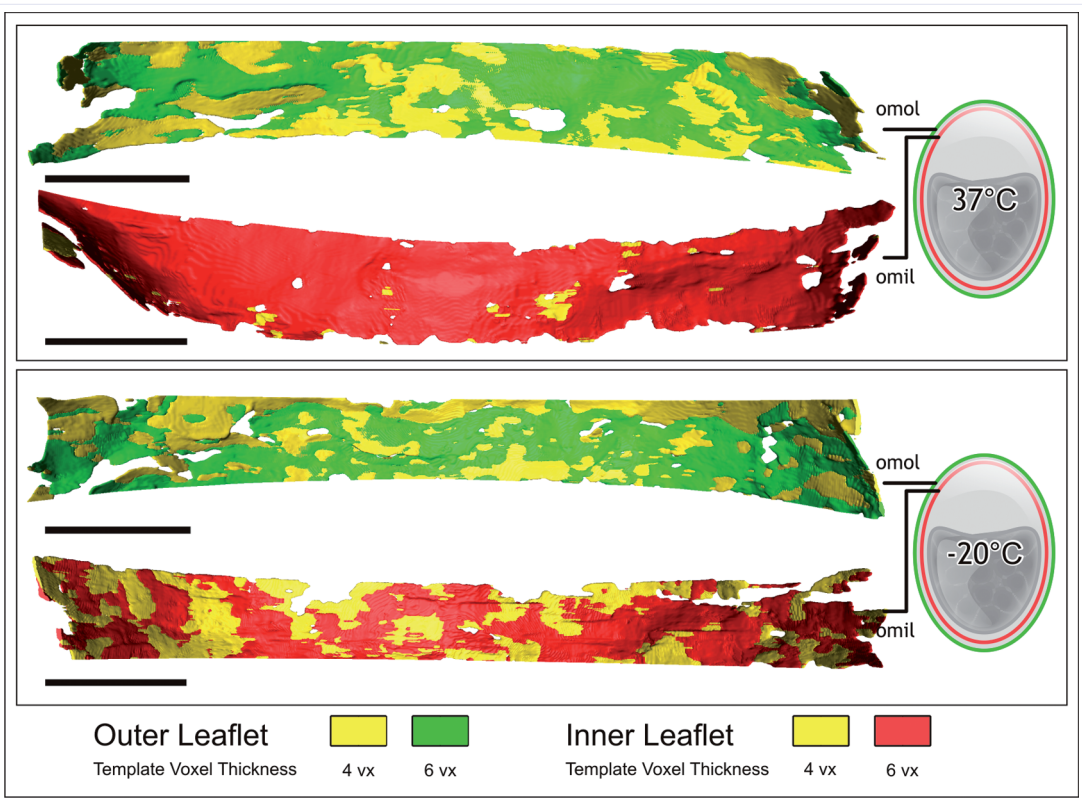


**Figure 5.4. Three-Dimensional Representation of Lipid Phase Separation in *E. coli* in opposing membrane leaflets.** *The E. coli outer membrane was analysed by electron tomography and template matching. Using cuboid-shaped templates of different thickness (4 and 6 voxels) and by maximum operation it was determined for each location on the membrane leaflets, with which of the templates it shared the greatest commonality. The LPS-based outer leaflet was hardly affected by the decrease in temperature (leaflet indicated as omol (green in the PDF-file) leaflet in both the upper and the lower panel), whereas the phospholipid-based inner leaflets showed a radical change from an homogeneous state (leaflet indiacted as omil (red in the PDF-file), upper panel) to a highly heterogeneous state (leaflet indiacted as omil (red in the PDF-file), lower panel). Bar indicates 100 nm (perspective changes throughout the image not taken into account). Camera positions were not matched.*

valid, as the overall cross correlation value for the inner leaflet of the outer membrane is indeed decreased (supplementary figure 5.2).

## 5.4. Conclusion

Because of their involvement in many cellular processes, a good understanding of the complexity of bio-membranes is critical to many biological questions. in recent years, electron tomography has had a great impact on our 3D understanding of organellar morphology, as well as on connectivity and continuity between organellar membranes. However, the technique has not been applied to processes occurring within a membrane, such as domain formation and phase separation. Bridging the gap between 3D morphology and ultra-structural membrane organization is a challenge for electron tomography and raises the bar for electron tomography to a new level.

In this article we have shown that within the biological model system of the *E. coli* we were able to visualize temperature induced heterogeneity within a membrane. The observed domains that are present within the inner leaflet of the *E. coli* outer membrane after -20ºC incubation are in line with the predicted effects of lipid phase separation and the resultant regions of protein aggregation and depletion, and share a size similar to those observed

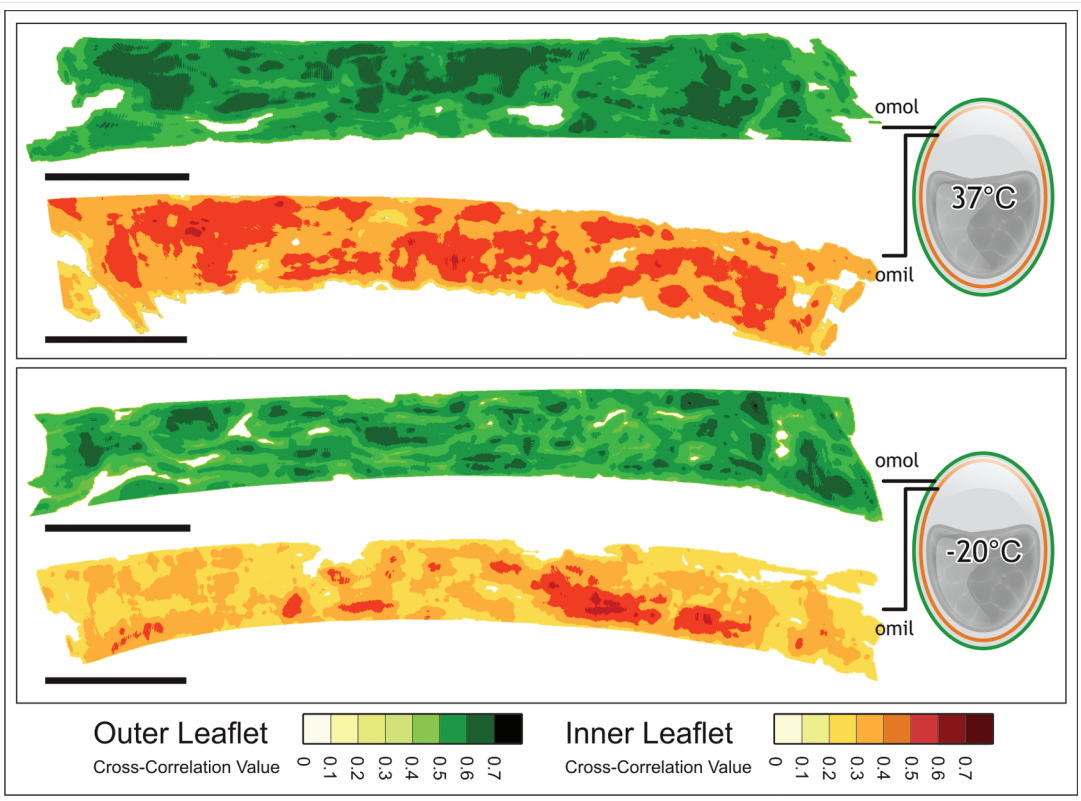


**Supplementary Figure 5.2. Three-Dimensional Representation of Membrane Recognizability at Different Temperatures.** *Recognizability of the membrane by template matching was analysed in an averaged cross-correlation file (averaged between the matched values of the 4 and 6 voxel thick templates). The overall visibility of the outer leaflet (green leaflet, upper and lower panel) did not show a considerable decrease is matching strength. In contrast, the matching values of the inner leaflet (red leaflet, upper and lower panel), decreased considerably. Since staining – and subsequently the recognizability – of the membrane is mostly affected by the presence of proteins, this decrease in visibility can be explained by a depletion of protein in the solidified lipid domains, and an accumulation in the fluid regions, both caused by lipid phase separation. While not perfect, an overlap can be observed between the less well recognized regions and the thinner stained membranes. Bar indicates 100 nm (perspective changes throughout the image not taken into account). Camera positions were not matched.*

by freeze fracture. As predicted by the difference in composition, we also observed, that the inner leaflet was far more affected by the temperature induced lipid phase separation than its LPS-composed counterpart. We can therefore conclude that the approach taken by combining template matching with electron tomography, is robust enough to extract information from a tomographic image that is not achievable by manual segmentation. By this approach a link is created between the morphological electron tomographic approach and the (local) composition of the biological membrane studied (as reflected in stain deposition).

The presented combination of techniques allows us to visualize the presence and shape of membrane domains on an electron microscopical level in three dimensions within their cellular context and can thereby can help us understand the structure and cellular complexity of these domains; and increase our insights into the processes in which they are involved.

## Acknowledgements

We would like to thank Hans de Cock for providing us with the *E. coli* cells, Willie Geerts for acquiring the tomographic tilt-series, and Bram Koster for critically reading the manuscript.

Template matching calculations were performed at the SARA super-computer facilities, Amsterdam, the Netherlands. Cellular Architecture & Dynamics is part of the NoE. This research was supported by a grant from Senter Novem (IOP Genomics project IGE03012).

# CHAPTER VI

## template matching reveals a spiral coating on the membranes of the caveolar system in endothelial cells

# template matching reveals a spiral coating on the membranes of the caveolar system in endothelial cells

M.N. Lebbink[✦] • N. Jiménez[✦] • K. Vocking
L.H.P. Hekking • A.J. Verkleij • J.A. Post

*Cellular Architecture and Dynamics, University of Utrecht, the Netherlands*

✦ *these authors contributed equally to the work presented in this paper*

If Edison had a needle to find in a haystack, he would proceed at once with the diligence of the bee to examine straw after straw until he found the object of his search... I was a sorry witness of such doings, knowing that a little theory and calculation would have saved him ninety per cent of his labor.

*Nikola Tesla*

Submitted in revised form

Endothelial cells are rich in caveolae, flask-shaped invaginations of the plasma membrane characterized by the presence of a striated coating and of caveolin on their cytoplasmic surface and by their role in multiple cellular processes, like transcytosis. Caveolae are part of a complex caveolar system comprising other caveolae-related structures so far less characterized. In this paper we present an extensive electron tomographic analysis of the caveolar system in situ. Large volumes of human umbilical vein endothelial cells (HUVECs) were studied to get insight in the 3D ultrastructure of the integral caveolar system and three dimensional template matching was applied to tomograms in order to localize membranes and membrane coatings in an objective manner. We provide a notable view on the architecture of the caveolar system that comprises - as confirmed by 3D immunolabeling for caveolin of 'intact' cells - *bonafide* caveolae, free plasmalemmal vesicles, racemose invaginations and multi-caveolar bodies. Remarkably, membrane coatings localized by template matching are distributed in a spirally fashion on all the subpopulations of the caveolar system. The novel observations that we present contribute to a clear view on the ultrastructural complexity of the caveolar system in the cellular context, setting a detailed morphological basis for its functional diversity.

## 6.1 Introduction

The luminal face of blood vessels is covered by a layer of endothelial cells that acts as a critical barrier between the lumen and the vessel wall, while allowing controlled transit of water, solutes and even cells between the blood and the subendothelial intima. These endothelial cells are rich in caveolae (Palade, 1961); specialized invaginated domains of the plasma membrane that are coated with caveolins. Over the years many studies have shed a light on the functional complexity of caveolae; revealing a role – frequently mediated by caveolin itself – in many cellular processes including cholesterol trafficking, signal transduction, and intracellular transport (for a review see (Anderson, 1998)). However, one of the most remarkable functions of caveolae in the endothelial context is the role that they play in mediating permeability by virtue of their transcytotic capabilities (Simionescu, 1983; Predescu et al., 1997).

Caveolae – or plasmalemmal vesicles – were first identified in electron microscopic studies as flask shaped invaginations of the plasma membrane (Palade, 1953; Yamada, 1955). In the decades upon their discovery, their characteristic morphology (shape, electron-translucent content, and a regular size of 60 to 90 nm in diameter) was the primary criterion for identification. By means of different electron microscopic techniques, several subpopulations of caveolae-related structures were described, namely: 1) luminal and abluminal *bonafide* caveolae; i.e. single invaginations from the plasma membrane (Burns & Palade, 1968), 2) free plasmalemmal vesicles (Burns & Palade, 1968), 3) luminal and abluminal clusters of caveolae continuous with the plasma membrane - also known as racemose invaginations (Chien et al., 1982; Bundgaard et al. 1983; Bundgaard, 1991; Sandvig et al., 2008), and 4) in specific types of endothelia, trans-endothelial channels (Simionescu et al., 1975) as well as vesiculo-vacuolar organelles (Kohn et al., 1992; Dvorak & Feng, 2001) that form pores spanning the cytoplasm of endothelial cells. A combination of these different caveolar subpopulations can be present in an endothelial cell and form a structurally complex system that will be henceforth referred to as the caveolar system.

A milestone in caveolae research was the discovery of a striated coating on the cytoplasmic surface of *bonafide* caveolae of endothelial cells (Peters t al., 1985) and the subsequent demonstration of caveolin as component of the coating in fibroblasts (Rothberg et al., 1992). However, a comprehensive high-resolution study of the distribution and 3D arrangement of the caveolar coating on the different elements of the caveolar system in the (endothelial) cellular context is lacking. This gap is partly due to the technical limitations of commonly used approaches that have to be applied to fragments of plasma membrane pulled out of cells (scanning electron microscopy (Peters et al., 1985) and replica analysis by transmission electron microscopy (TEM) (Rothberg et al., 1992) or that provide a mere 2D view of structures in their cellular context (conventional

TEM of thin sections (Burns & Palade, 1968). In recent years, electron tomography has emerged as a robust approach to obtain ultrastructural 3D information on cellular components within their cellular environment (Baumeister et al., 1999; McEwen & Marko, 2001). However, in a recently published study including several cell types, analyses by means of manual annotation of tomograms in which a coating was observed on the caveolar-membrane failed to recognize any order of organization of the coating beyond random irregular strands that, as suggested by the authors, could be due to the redistribution of stain caused by the electron beam (Richter et al., 2008). Bearing in mind all the technical limitations just mentioned, it appears that a proper analyses of the architecture of the intact caveolar system and localization of a putative coat on the caveolar membrane by electron tomography demands the following requirements to be met: first, complete cells should be optimally fixed for the preservation of ultrastructural details, allowing the caveolar system to be studied in situ. Second, post-staining of sections should be avoided, since staining may introduce 'artefacts' that obscure ultrastructural details (due to, for example, the limited penetration of the contrasting agents throughout the embedding-resin that causes a gradient of density in the tomogram's *Z* direction). Third, large cellular volumes should be analyzed in order to find diverse structures representative of the caveolar system. And fourth, to reduce misinterpretation, objectivity should be strived for during data analyses.

In this paper we present an extensive electron tomographic study of the caveolar system in human umbilical vein endothelial cells (HUVECs). In order to preserve ultrastructure in a near-native state, cells were cryoimmobilized by high-pressure freezing. To allow for the analysis of non post-stained material, HUVECs underwent tannic-acid mediated osmium impregnation after freeze-substitution and prior to embedment in Epon (Jiménez et al., 2009) . Large cellular volumes were acquired by electron tomography and three dimensional template matching (Frangakis et al., 2002; Lebbink et al., 2007) was applied to localize membranes and membrane coatings of the caveolar system in an objective manner. Our results provide a remarkable view on the architecture of the caveolar system in HUVECs that comprises not only membrane attached (single or clustered) and free caveolae, but also free pleomorphic caveolar clusters (that we refer to as multi-caveolar bodies). Interestingly, based on the localization of membrane coatings by template matching, it is revealed that on all subpopulations of the caveolar system they are distributed in a spirally fashion. In addition, we have confirmed the presence of caveolin on the membranes of the caveolar system by 3D immunolabeling of 'intact' HUVECs prior to embedment in Epon. The present work contributes to a clear view on the ultrastructural complexity of the caveolar system within its cellular context, setting a detailed morphological basis for its functional diversity.

## 6.2 Material and Methods

### 6.2.1 HUVECs isolation and culture

Endothelial cells were isolated from umbilical veins as previously reported (Eman et al., 2006). Umbilical cords had been obtained from the Department of Obstetrics and Gynecology, Diakonessen Hospital, Utrecht, The Netherlands, with the informed consent of the parents. Cells (passage 1) were cultured in culture dishes containing Aclar pieces (discs of 1.5 mm diameter for high-pressure freezing; squares of 1 cm side for chemical fixation) coated with Matrigel, exactly as previously described (Jiménez., 2009). Medium was refreshed every 2 or 3 days. After reaching confluence, cells were incubated four more days before being further processed in order to allow the cell monolayer to reach a tight cobblestone status mimicking the endothelium in situ.

### 6.2.2 Cell processing by high-pressure freezing/freeze-substitution or by chemical fixation for transmission electron tomography

Cells grown on Aclar discs were cryoimmobilized by high-pressure freezing and subsequently freeze-substituted as described before (Jiménez., 2009). The freeze-substitution fluid consisted of 2% $OsO_4$ (Electron Microscopy Sciences, Hatfield, PA), 0.1% anhydrous glutaraldehyde (

Electron Microscopy Sciences) and 1% $H_2O$ in anhydrous acetone (Merck, Darmstadt, Germany). After freeze-substitution and before embedding in Epon, cells underwent en block osmium impregnation mediated by tannic acid to improve membrane contrast [Jimenez., 2009]. To this end, cells were incubated with 1% tannic acid and 1% $H_2O$ in anhydrous acetone, 1 h, washed with acetone, treated with 1% $OsO_4$ and 1% $H_2O$ in anhydrous acetone, also for 1 h, and washed again with acetone. All the incubations for the osmium impregnation happened on ice. Finally cells were embedded in Epon [Jimenez., 2006]. Cells grown on Aclar squares were chemically fixed with aldehydes, post-fixed with $OsO_4$, tannic acid-mediated osmium impregnated and embedded in Epon exactly as reported [Jimenez., 2009].

After Epon polymerization Aclar pieces were removed from the block leaving exposed the Epon-embedded cell monolayer. Fresh Epon was added and left to polymerize. Blocks were properly trimmed and 300-nm thick sections were cut perpendicular to the cell monolayer. In this way, both the apical (or luminal) and basolateral (or abluminal) plasma membrane of the cells could be visualized in every section. Sections were collected on copper slot grids coated with Formvar and carbon. Colloidal gold particles (15 nm) were applied to one side of the grid to serve as fiducial markers in the alignment of the tilt series. Sections were not post-stained.

### 6.2.3 Pre-embedment immunolabeling of cells for 3D localization of caveolin

HUVECs grown on Aclar squares were chemically fixed with 4% paraformaldehyde in 0.2 M HEPES buffer pH 7.3, 30 minutes at room temperature (RT). After washing with PBS, cells were permeabilized with 0.1% Saponin in PBS for 30 minutes at RT. Next, cells were incubated 1 hour at RT with 5 µg/ml rabbit α-caveolin (Transduction Laboratories, Lexington, KY) primary antibody, thoroughly washed, incubated 1 hour at RT with protein A conjugated to 5-nm-gold ( Department of Cell Biology, Medical School, Utrecht University, The Netherlands), and washed again. PBS containing 0.1% Saponin was used for the washing and to dilute antibodies. Next cells were rinsed thoroughly with PBS before undergoing a chemical fixation, post-fixation, osmium impregnation and Epon embedding as explained in the previous section. This extra fixation and en block osmium impregnation after immuno-labelling was done in order to improve the ultrastructural preservation and contrast of the cells for electron tomographic studies.

### 6.2.4 Electron tomography

For every condition (high-pressure frozen, chemically fixed or immuno-labeled cells) regions of interest were localized using a Tecnai-12 microscope (FEI Company; Eindhoven, The Netherlands) operating at 120 kV equipped with a side-mounted Megaview II camera (Olympus Soft Imaging Systems; Münster, Germany). Cellular areas containing a high-density of caveolae-like structures (based on morphological criteria, and eventually in the presence of gold labeling for caveolin) were located and pre-irradiated to prevent Epon to shrink during the tilt series acquisition. Afterwards, tilt series of the regions of interest were automatically recorded at 200 kV using a Tecnai-20 microscope (FEI Company) equipped with a bottom-mounted slow-scan CCD camera (Tem-Cam F214; TVIPS GmbH, Gauting, Germany) and a motorized goniometer. Grids were placed in a Model 2020 Advanced Tomography Holder (E.A. Fischione Instruments Inc, Export, PA). Recording was performed with Xplore3D software package (FEI Company). Specimens were tilted at 1° intervals from -65° to +65°. This resulted in a dataset of 131 collected digital images (2048×2048 pixels each) with a pixel size of 0.7 nm. Grids were then manually rotated by 90°, and similar series were taken. Recorded images were aligned, tomograms reconstructed and two orthogonal single-axes tomograms were merged into one using the IMOD software package [Kremer et al., 1996; Mastronarde, 1997]. For accuracy in the alignment of the tilt series, the centre of the fiducial markers was manually selected in every image projection. In the final step prior to reconstructing the tomographic volume, by means of weighted-back projection, the

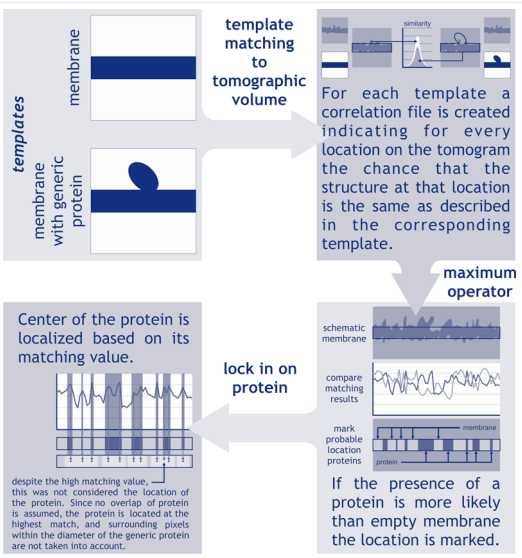


**Supplementary Figure 6.1. Schematic depiction of the steps involved in localizing proteins on a membrane by template-matching.** *In the first step two templates are created; one describing empty membrane, and one describing a membrane with a coat element attached. In the second step these templates are compared to every location in the volume by template matching, and a cross-correlation- or matching-value is obtained. In the third step, a maximum operation is applied to determine where on the membrane the chance (matching-value) is higher for the presence of a coat element than for empty membrane. In the final step the centre of the protein is determined, and surrounding voxels are removed to prevent overlap.*

volume was binned resulting in a final voxel-size of 1.4 nm (not taking into account shrinkage in *Z*-direction) for the reconstructed tomograms. When necessary, tomograms of serial sections were calculated, aligned to each other and joined into a single volume using the program Midas, incorporated in IMOD.

### 6.2.5 Manual segmentation of tomograms

3D modelling of immunolabeled cells was performed by manual segmentation. For this, tomograms were displayed in 3DMOD graphical user interface (as part of IMOD package). They were thoroughly examined to make an initial assessment of the architecture of caveolae-like structures. This analysis was made first in the ZaP Window of 3DMOD which allows visualizing the tomogram in parallel to the plane of the original ultramicrotome sections (*XY* plane). When necessary, the Slicer tool (part of 3DMOD program) was used to rotate the data around the *X*- *Y*- and *Z*-axes. 3D models were produced within the Zap Window, by tracing contours overlaid on the membranes present in every tomographic slice *(Kremer et al., 1996)*, combining manual tracking with computer-assisted tracking of high contrast lines. Each distinct membrane-bound compartment was drawn as a different object and a different colour was assigned to each object. Gold particles were represented as spheres. Finally all the contours were meshed and the *Z*-scale was stretched with a factor 1.66 to correct for the expected 40% Epon shrinkage. 3D models were displayed and analysed using the Model View Window of 3DMOD.

### 6.2.6 Template matching of membranes and coated membranes

The process of localizing membranes and coatings by template matching is schematically depicted in supplementary figure 6.1. Template matching was

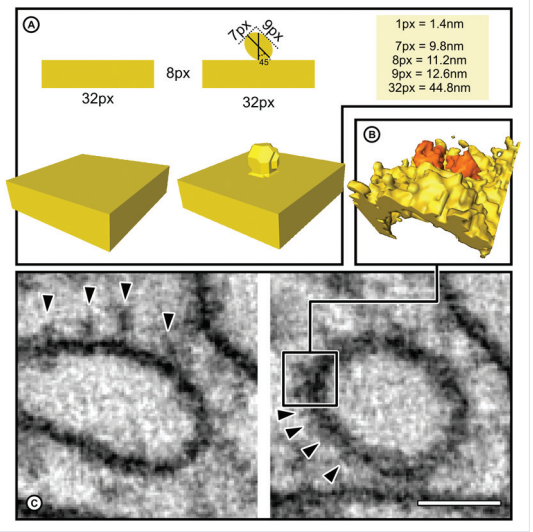


**Figure 6.1. Template Based on the Proteins on the Caveolar Membrane. Two templates were created.** *The first resembled empty membrane and was cuboid shaped, while the second contained the same membrane with a structure, representing the protein-coat complex, attached (A). The shape and size of the attached structure was based on the overall three-dimensional properties (B) of the membrane attached complexes observed in the tomographic micrographs (C, arrowheads). Scalebar: 50 nm*

performed using OmniMatch (developed in the group of Baumeister [Böhm et al., 2000; Frangakis et al., 2002]) on a computer-cluster running 54 CPUs (at the SARA supercomputer facilities, Amsterdam, The Netherlands), as described in [Lebbink et al., 2007]. Two distinct templates (created with Matlab (Mathworks, USA) and the Tom Toolbox [Nickell et al., 2005]) were matched to the tomograms, one schematically describing the (empty) membrane, and the other describing a membrane with an attached generic coating. The shape and size of the simplified generic coat (figure 6.1) was based on structures in our tomograms that resembled the structures described by [Richter et al., 2008] and were in agreement with the expected dimensions (approximate 10 nm in diameter) of the caveolin oligomers suggested to assemble into caveolin filaments [Fernandez et al., 2002]. After template matching the assumption is made that a membrane associated particle is present at a location if that stretch of membrane shares a greater resemblance to the coat-attached template than to the empty template. This is achieved by a maximum operation where - for each voxel - the correlation-values are checked [Lebbink et al., 2009]. If the voxel does not exceed a minimal threshold for either template, then it is not identified as a membrane at all, and is given a value of 0. If the first template (empty membrane) has a higher correlation-value than the second template (describing the membrane-coat complex), a value of 1 is assigned. If the second template provides the highest correlation-value, the voxel is given a value of 2. Next the location of the coating is determined more accurately by marking the voxel with highest correlation-value on a stretch of membrane on which the presence of a coat was determined. The diameter of the membrane attached structure in the template exceeded the diameter of the marking to enhance readability of the marked, template matched image (all done in Matlab combined with the Tom Toolbox). The organization of the localized coatings on the membrane was then manually analysed in 3D in AMIRA, and the order was carefully highlighted.

## 6.3 Results and Discussion

### 6.3.1 Identification of Caveolae and Caveolae-Related Structures Based on Morphological Criteria

While the classical view on caveolae regarded them as 'single entity' budding vesicles, it is becoming clear that they are part of a structurally complex system involved in many cellular events. Application of electron tomography is therefore essential to fulfil a reliable and integral 3D study on the caveolar system in situ. Based on their unique morphology, we observed a number of caveolae-related subpopulations in tomograms obtained from endothelial cells processed by high-pressure freezing and freeze-substitution. In the supplementary data a movie is included of a representative tomographic volume giving an overview of these structures in HUVECs (Supplementary Movie 6.1). The primary member that could be observed was the true flask-shaped caveola hanging from the plasma membrane (figure 6.2.A). While the diameter of these invaginations varied, their sizes were within or close to the expected range of 60 to 90 nm, ranging up to 110 nm in some cases. Occasionally, we observed structures at the plasma membrane that morphologically appeared to be budding or fusing caveolar profiles (figure 6.2.B). The second type of caveolae-related structures was the free caveola-like vesicle (figure 6.2.C). As reported by others [Bundgaard et al., 1983], we found that this subpopulation was extremely rare. The size of the occasional caveolar vesicles observed within the samples was within the 60 to 90 nm range. The third subpopulation included plasma membrane-bound clusters of caveolae (racemose invaginations) of different sizes and complexities (figure 6.2.D). Even though racemose invaginations (reconstructed in their totality) were observed at both sides of the cell - penetrating deeply into the cytoplasmic volume - no open connection from one side of the cell to the other has been observed in our tomograms. The final population were intracellular structures resembling a body of multiple fused caveolar vesicles that we refer henceforth to as multi-caveolar bodies (figure 6.2.E). These structures were sometimes very large and spanned the whole tomographic volume (up to

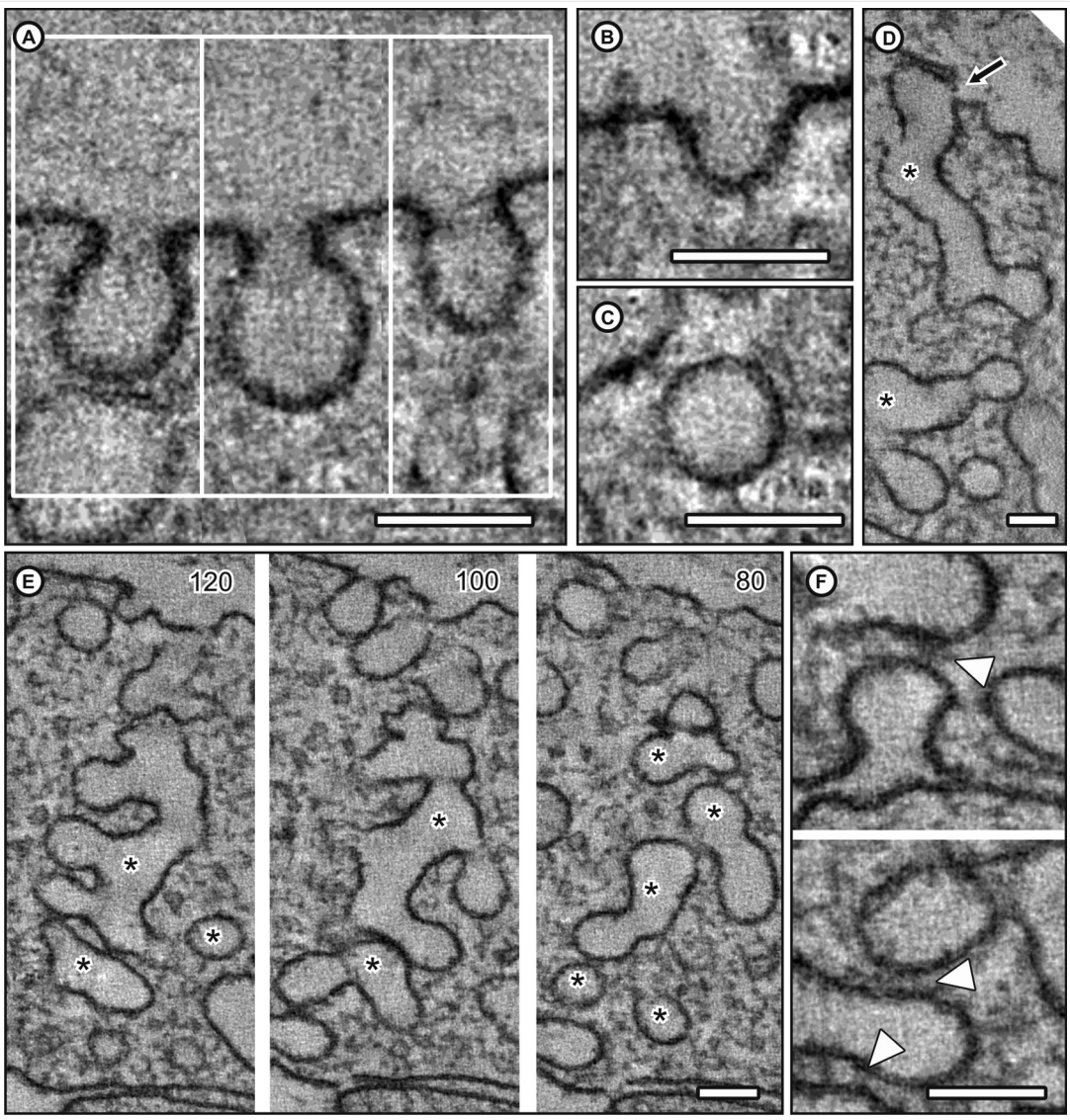


**Figure 6.2. Members of the caveolar system visualized in tomograms of high pressure frozen, freeze-substituted and tannic-acid mediated osmium impregnated HUVECs.** *(A) Diverse caveolae are regularly observed hanging from the plasma membrane at different depths of the tomogram. (B) Sometimes different stages of what appear like budding/fusing profiles are observed. (C) Occasionally, bonafide free caveolar vesicles can be identified in the tomograms. Racemose invaginations can be observed penetrating deeply the cytoplasm of the endothelial cells (D, asterisks; the arrow points the opening to the extracellular space). Figure E shows one large multi-caveolar body (asterisks), which has no direct connection to the plasma membrane, although close apposition and tethering to other – plasma membrane connected - members of the caveolar system is observed (figure F; tethers pointed out by arrowheads; numbers indicate the slice position in the tomogram). Scale bars: 100nm.*

700 nm thick, reconstructed from serial sections) without being continuous with the plasma membrane. Since membrane continuity out of the reconstructed volume cannot be ruled out in these cases, they could be a partial reconstruction of a racemose invagination or a vesicular-vacuolar organelle. However, they could also be caveosomes, organelles positive for caveolin originally

identified and defined in fibroblasts by its function in the endocytosis of viruses mediated by caveolae (Dvorak & Feng, 2001). Interestingly, multi-caveolar bodies often lie in direct proximity of plasma membrane-bound caveolae and racemose invaginations and, in several cases, thread-like complexes (resembling tethers) could be observed connecting the structures (figure 6.2.F). In intracellular membrane trafficking, tethering factors have been proposed to function as molecular bridges that anchor membranes prior to fusion mediated by SNAREs (Sztul & Lupashin, 2006). Tethers have been described between (apparently free) caveolar vesicles and plasma membrane (Palade & Bums, 1968; Predescu et al., 2005) and SNAREs have been shown to play a role in caveolar fusion to the plasma membrane (Predescu et al., 2005). These findings have been interpreted as evidence for the existence of dynamic (single) caveolae involved in transcellular transport (Predescu et al., 2007). The presence of tethers between caveolae

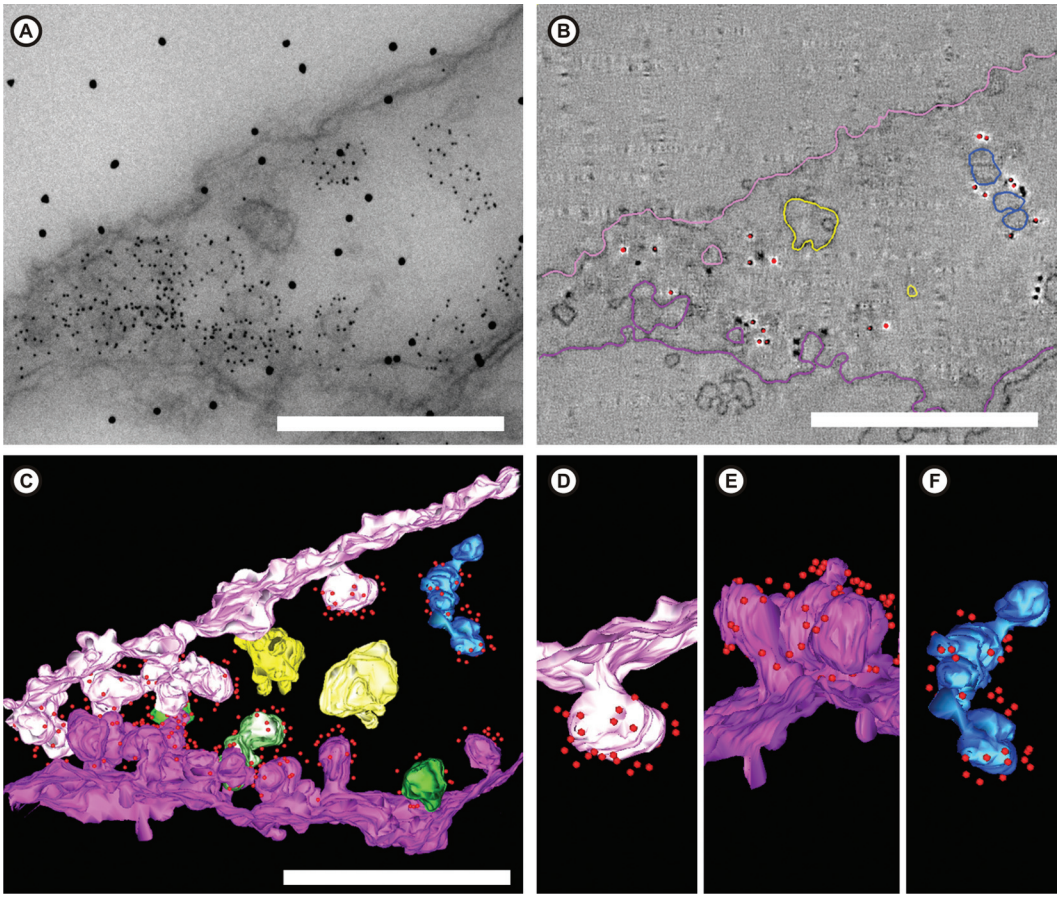


**Figure 6.3. Pre-embedment immunolabeling for caveolin examined by electron tomography.** *(A) Conventional (2D) TEM micrograph of a 300 nm-thick section showing a cellular volume rich in caveolin, localized by the small (5 nm) gold particles. The large gold particles that were applied on the section surface to serve as fiducials for tilt series alignment. (B) Virtual (approximate 2 nm-thick) section extracted from the tomogram reconstructed from dual tilt-series obtained from the volume in (A). Membranes are highlighted manually, and gold particles are indicated as red spheres. (C) View of the complete 3D model obtained by meshing the contours traced on membranes. Luminal (light pink) and abluminal (dark pink) caveolae and racemose invaginations as well as a small multi-caveolar body (blue) are positive for caveolin. Green structures, also labelled for caveolin, have no continuity with the plasma membrane in the tomographic volume, but their real identity (racemose invagination or multi-caveolar body) cannot be established since they are incomplete. Note the absence of labelling on flat areas of the plasma membrane and at endosomal structures (yellow). (D-F) Close-up-views of a luminal caveola (D), abluminal clustered caveolae (E) and the multi-caveolar body (F). Scale bars: 500 nm*

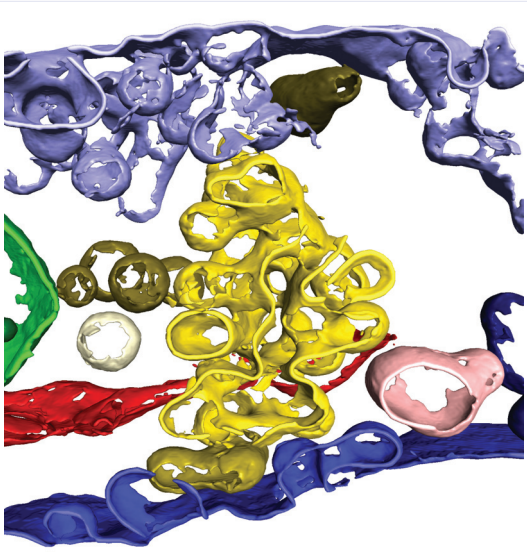

*Figure 6.4. Membranes of the caveolar system and of other cellular structures annotated by template matching. An artificial cuboid-shaped template (32x32x8 pixels) was used to localize membranous structures within a caveolae-rich tomographic volume. Three manual clean-up steps were performed in Amira (TGS/Mercury, France) for visualization purposes. First, a threshold was applied to the cross-correlation file. This value was selected manually to 0.54 out of a maximum correlation of 0.86, which in this example preserved the majority of membrane, and removed the background (non-membranous structures). Second, false positives were removed with the "3D magic wand tool" by including only elements that were (in 3D) attached to obvious membranes. Third, colouring was applied to indicate which structures had membrane continuity. Membranous structures present in the tomogram could be properly segmented in this way. Light blue: luminal plasma membrane, caveolae and racemose invaginations; dark blue: abluminal plasma membrane, caveolae and racemose invaginations; yellow: large multi-caveolar body; green: endosome; red: endoplasmic reticulum; white: free caveola-like structure.*

and multi-caveolar bodies suggests that these structures can potentially fuse, which could mean that caveolae can be involved in transcellular transport in ways diverging from the canonical vesicular transport mediated by single plasmalemmal vesicles. In order to determine if this is the case, further work should be performed including immunolocalization of tethering factors and other components of the fusion machinery. In summary, based on morphological criteria, we have determined the presence of diverse types of caveolae-related structures, characterised by a distinct architecture, in HUVECs.

### 6.3.2 3D Analysis of Pre-Embedment Immunolabeling Confirms the Presence of Caveolin on the Different Elements of the Caveolar System

Next, we aimed to confirm that each of the compartments morphologically identified as members of the caveolar system in HUVECs were indeed caveolae-related structures. Since its discovery on the surface of caveolae in fibroblasts *(Rothberg et al., 1992)*, caveolin has been used as caveolar marker par excellence. In endothelial cells, different types of caveolae-related structures have been characterized by means of caveolin immunolocalization by conventional (2D) TEM *(Esser et al., 1998; Vaile et al., 1999)*. In our study, caveolin needed to be detected in the 3D cellular context for a doubtless identification of the different kinds of subpopulations integrating the caveolar system. To this end, we labelled caveolin in chemically fixed HUVECs prior to embedment in Epon (see complete protocol for pre-embedment immunolabeling in 'Material and Methods' section), and thick sections were examined by means of electron tomography to obtain a 3D overview of caveolin-distribution throughout the cell (figure 6.3). Luminal and abluminal single caveolae and racemose invaginations, as well as small free multi-caveolar bodies were found to be positive for caveolin (figures 6.3.C-F). Free vesicles labelled for caveolin were identified very seldom. Caveolin labelling was found not to be restricted to the neck but was also present on the bulbs of *bonafide* caveolae (figures 6.3.D). These findings conflict with the suggestion that caveolin associates only to the neck of caveolae *(Thorn et al., 2003)* but agree with other recently published data *(Richter et al., 2008)*. Furthermore, we also observed that caveolin was distributed all over the caveolar bulbs of racemose invaginations and multi-caveolar bodies (figure 6.3.E-F). Our results show that all the structures identified in the preceding section as members of the caveolar system were indeed caveolae-related structures.

### 6.3.3 3D Visualization of the Caveolar System by Template Matching of Membranes

Template matching is a digital image processing technique to objectively localize regions of an image that match a template image. In cell biology, this technique was initially applied to localize macromolecular complexes in cryo-electron tomograms of vitrified cellular extracts (Böhm et al., 2000) or of cryofixed phantom cells (Frangakis et al., 2002). Later on it was shown that template matching could also serve as tool for annotation of membranes and membrane domains in tomograms of stained biological material (Lebbink et al., 2007; Lebbink et al., 2009). Matching of a tomographic volume against a cuboid template (representing membrane) provided an objective 3D impression of the organization of organelles in post-stained sections of cryo-immobilized, freeze-substituted, and Epon-embedded cells (Lebbink et al., 2007). For the present work HUVECs underwent tannic-acid mediated osmium impregnation after freeze-substitution and prior to Epon embedment in order to increase cell contrast without the need to post-stain sections (Jimenez et al., 2009). In order to check whether cells processed in this way had appropiate contrast to allow annotation by template matching, a tomographic volume (the same shown in Supplementary Movie 6.1) was matched using a template representing membrane (equal to the template in figure 6.1.A, left; see legend of figure 6.4 for technical details). As shown in figure 6.4, segmentation of membranes was possible and enabled localization of the plasma membrane, diverse elements of the caveolar system, as well as the remainder organelles present in the tomogram. Therefore, tannic-acid mediated osmium impregnation leads to a specimen on which template matching can indeed be applied, without the need for post-staining.

### 6.3.4 Template Matching Reveals a Spiral Coating-Organization on the Membranes of the Caveolar System

From replicas of deep-etched fibroblasts (Rothberg et al., 1992) and scanning electron microscopical data of endothelial cells (Peters et al., 1985) it is known that chemically fixed caveolae (attached to the plasma membrane pulled out of cells) are covered by a structurally unique striated coat. This suggests that proteins on the cytoplasmic side of the invaginated caveolar membrane are distributed in an orderly fashion that might be characteristic of these structures. Based on this, we wanted to study whether a similar distribution would fit the organization of an eventual coating objectively localized by template matching on *bonafide* caveolae, but also on the other subpopulations of the caveolar system present in HUVECs (fixed by high-pressure freezing, and subsequently freeze-substituted and osmium impregnated before embedding). To this end, the first step was to create appropriate templates to be matched. Based on the structure of the membrane-associated particles found by Richter and co-workers in tomograms of caveolae (Richter et al., 2008) and on the 3D appearance of similar structures in our present tomograms, we created a template of membrane onto which a hypothetical coat element was attached, similar to (but not exclusively) a caveolar coat component (figure 6.1). The second step was to match the created template to tomographic volumes. By 'subtracting' the two correlation-files (via a maximum-operator) matched against two templates that differ in a single property, the location of voxels containing this property is indicated within the tomogram. In our case, we localized membrane-areas onto which coat particles were attached by comparing it to the cross-correlation file against 'empty' membrane. The centre of these particles was then indicated by the highest cross-correlation value within such an area. Due to technical reasons, the centre of the matched coat components was shifted a few voxels (approximately 4) perpendicular to the membrane. This does, however, not affect their distribution. The third step was to test the efficiency of the approach that we applied. For this, we compared the template matched localization to manual localization of coat particles on the membrane. We could confirm that template matching localized the same coat components on the membrane as identified by manual localization (data not shown). Moreover, the technique positively identified many locations that had been mistakenly excluded by manual annotation. The fourth and last step was a careful analysis of the coat distribution both in successive 2D virtual tomographic sections

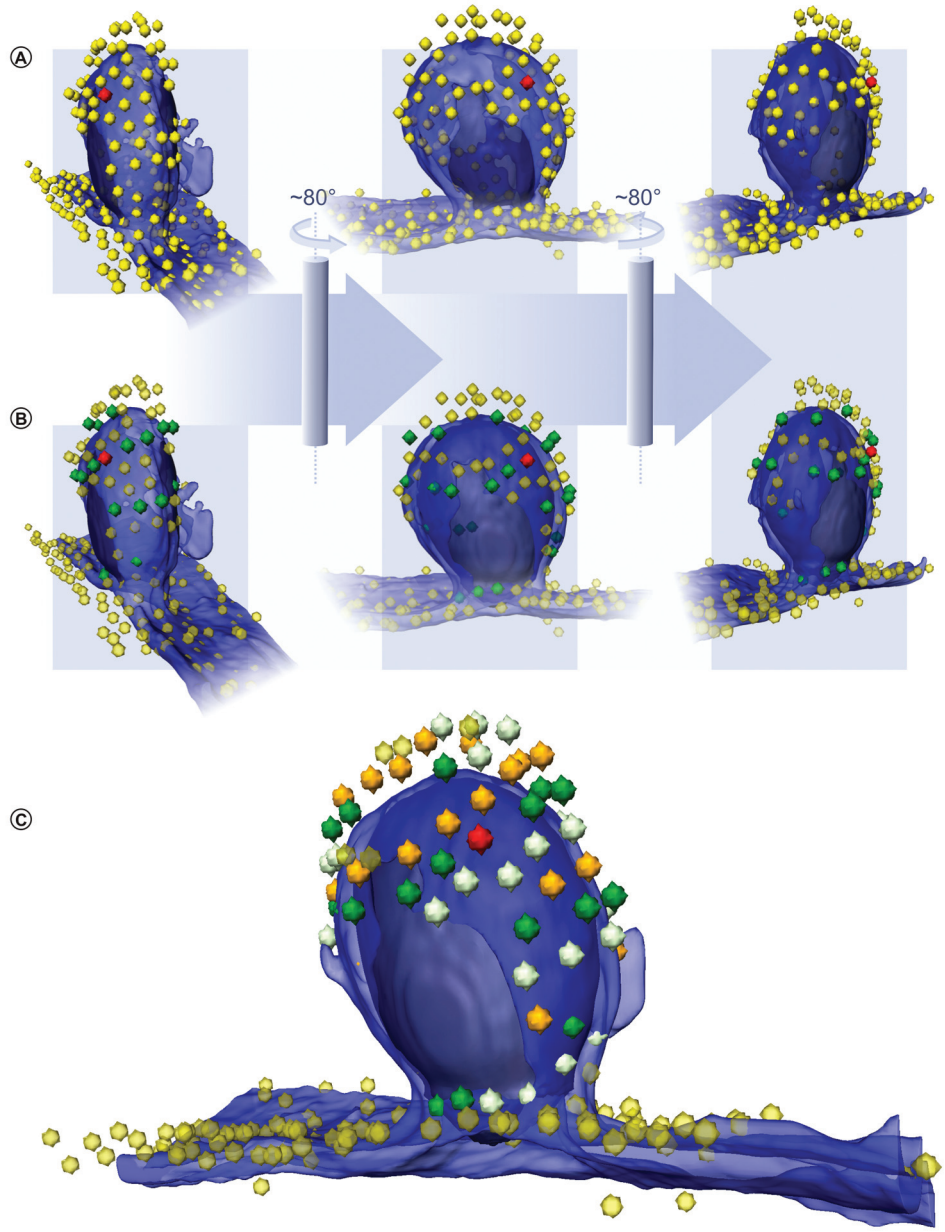


**Figure 6.5. Coating distribution on the membrane of a *bonafide* caveola.** *(A) presents all membrane coat elements (represented by balls) on a caveola that were localized by template matching in 3D seen from three orientations. (B) The coating arranged in a single spiral is indicated in green. (C) Three parallel spirals are indicated. Some matched coat particles are represented transparent in B and C in order to facilitate the visualization of the spirals. The coat element indicated in red is the same throughout all the images. The area lost by the missing wedge is clearly visible (dark blue), and no coating elements are identified within this area. The markings (balls) indicating the location of the centre of the coat components are smaller than the area covered by the actual coat (and structure in the template) to increase readability of the image. Increasing the ball-size does not make the spirals more obviously visible.*

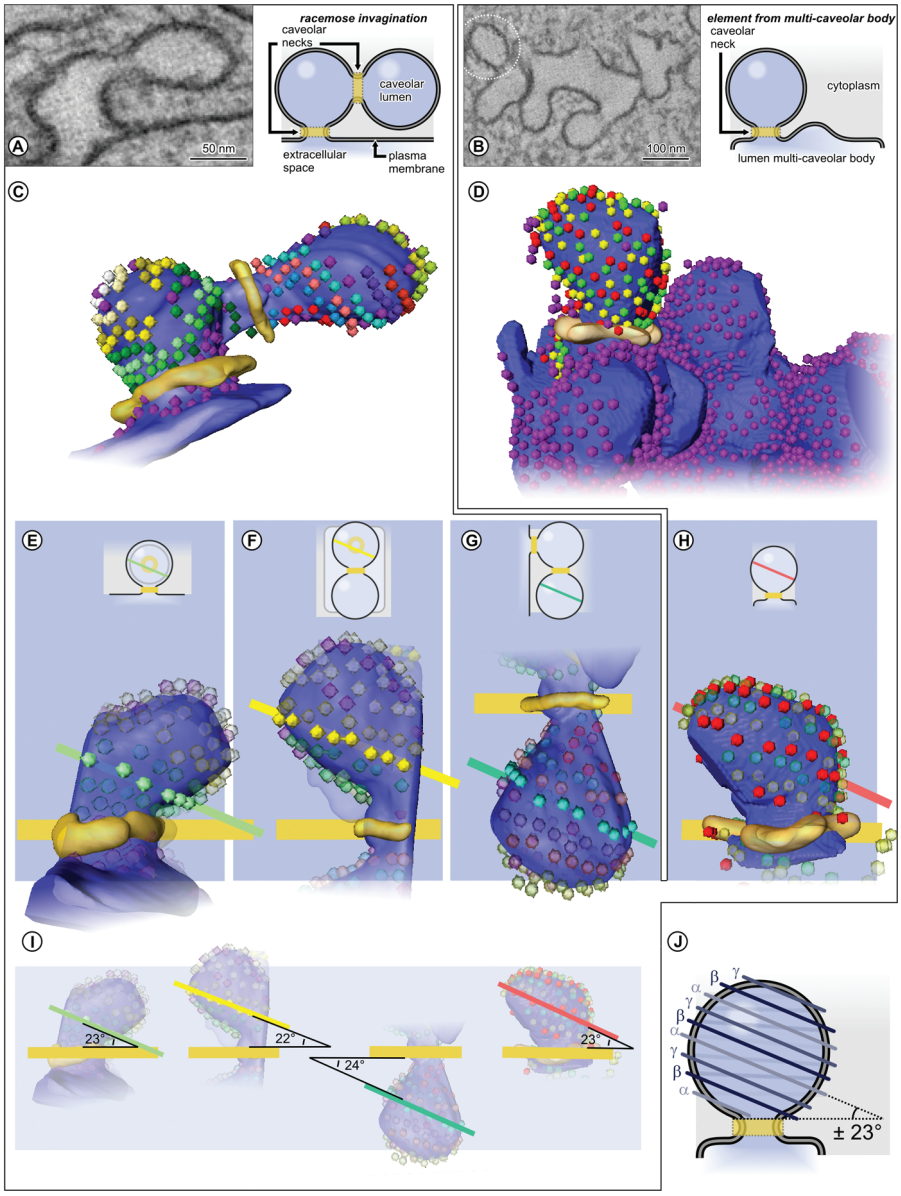


**Figure 6.6. Coating distribution on the membrane of racemose invagination and multi-caveolar body.** *(A) shows a simple racemose invagination consisting of two caveolar entities attaches to each other and to the plasma membrane. The structure can be divided into two parts: a double-necked entity (connected to the plasma membrane) and a single-necked entity (connected only to the other caveolar bulb). (C) shows that multiple spirals cover both the necks and bulbs of the racemose invagination. When their continuity was uncertain due to the missing wedge, spiral-segments were not given the same colours. Single spirals on this racemose invagination are highlighted in (E-G) and projected in relationship to the orientation of the different necks on the structure. (B) shows a multi-caveolar body on which a single-necked entity is indicated by a dotted circle. Upon analysis of the distribution of the coat elements on the indicated entity (D) a similar triad of spirals was observed on this multi-caveolar element as was seen on bonafide caveolae hanging from the plasma membrane. A single spiral is highlighted in (H) and projected in relationship to the orientation of the neck. In (I) the angle of the spirals is referred to the plane of the neck and it was found that they all shared a similar orientation of approximately 23 degrees. (J) summarizes the general organization of the coat elements on a single-necked caveolar entity.*

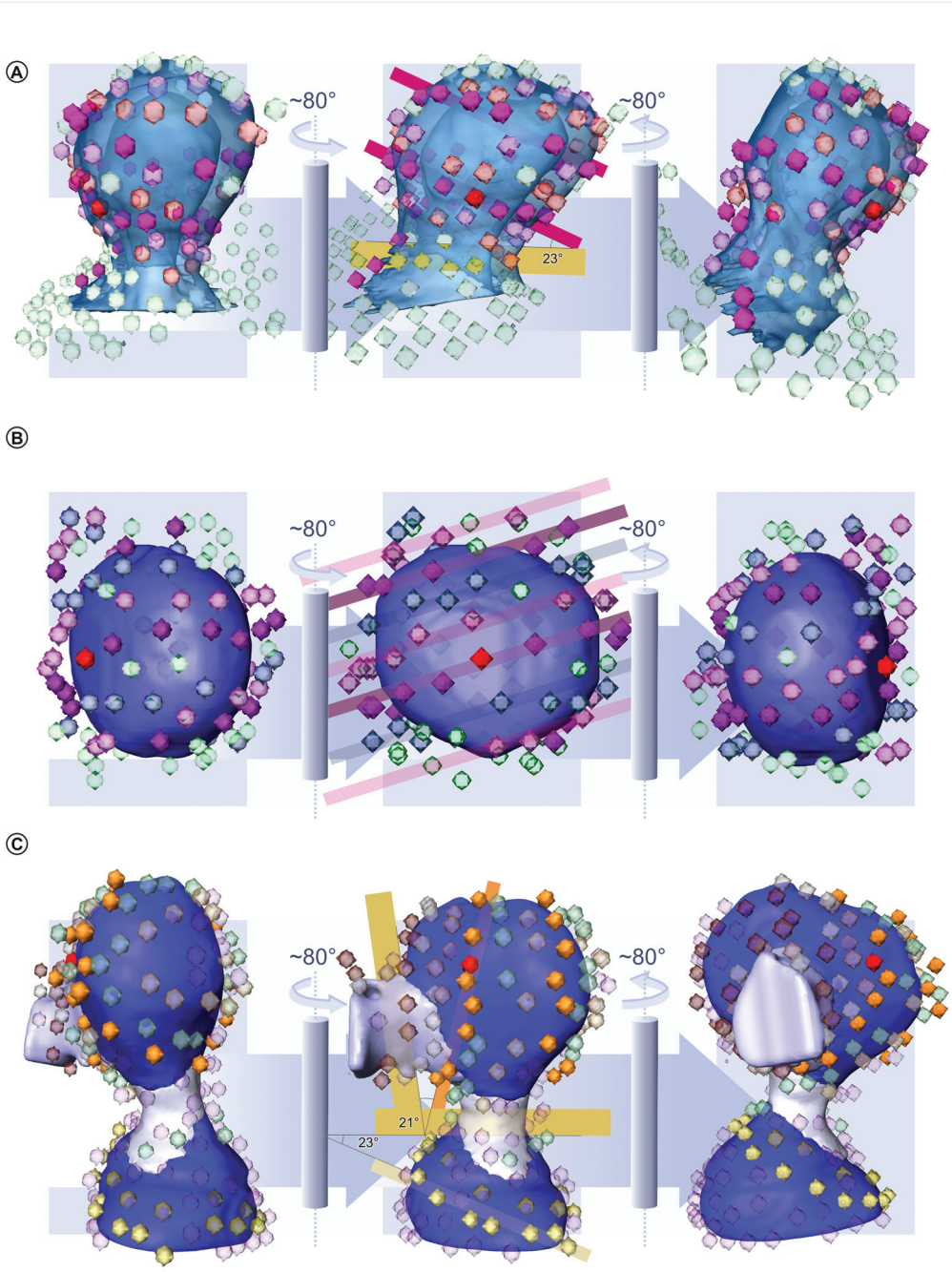


**Supplementary Figure 6.2. Coating distribution on the membrane of caveola, free caveola and racemose invagination in chemically fixed endothelial cells.** *Upon chemical fixation the same triad of spirals can be observed as was seen in samples fixed by high-pressure freezing. In single necked entities like bonafide caveolae (A) and neckless entities likes free caveolar vesicles (B) a triad of parallel spirals could be observed. In double-necked racemose invaginations (C) the organization of these spirals is more complex albeit still organized in a parallel fashion. The orientation of the spirals in relationship to the neck was similar to the angle observed in high-pressure frozen samples. The coat element indicated in red is the same throughout all the set of images.*

and 3D views of the members of the caveolar system.

Since the characteristic caveolar coating reported in the past was described for plasma membrane bound caveolae (Peters et al., 1985; Rothberg et al., 1992), we began with the analysis of *bonafide* caveolae. We could observe an organization in which successive coat elements were at a (by eye) predictable distance from each other (figure 6.5). Remarkably, these particles were arranged as series of (commonly three) spirals covering both the neck and bulb of the invagination (figure 6.5). When related to the plane of the caveolar neck, these parallel spirals had an angle of approximately 23 degrees. The spirally organization of the matched coat was so well-defined that it could never be accounted for consecutive (closed) circular rings on the surface of the caveolae. In our study we also template matched biological membranes of caveolae-unrelated structures (the Weibel-Palade bodies) present in the same tomograms. In this case, we did not observe an ordered distribution of coats on the membrane (data not shown), indicating that the spirally-organization is caveolae-specific. It has been hypothesized that the caveolar coat is too fragile to withstand non-chemical forms of fixation (Richter et al., 2008). Although we did observe a spiral-like distribution in the non-chemically fixed samples, in order to reduce the chance of (potential) loss of the coating during preparation, we also included chemically fixed HUVECs (processed as described in Material & Methods) in this study for comparison. Our results showed that no obvious difference in coat organization could be observed when comparing high-pressure frozen (figure 6.5) and chemically fixed samples (supplementary figure 6.2). Therefore, by objective annotation of tomograms by means of template matching, we could demonstrate that *bonafide* caveolae of both cryofixed and chemically fixed endothelial cells have a spiral coating on the cytoplasmic side of the membrane, what is in agreement with the data obtained by scanning electron microscopy and TEM analysis of replicas in endothelial cells and fibroblast (Peters et al., 1985; Rothberg et al., 1992). The fact that cells, processed in notably different ways and analysed using different approaches (compare Material & Methods in (Peters et al., 1985; Rothberg et al., 1992) with the current), show the spiral coating indicates that the coating distribution is not an artefact caused by sample preparation, but is indeed a representation of the in vivo organization of the coat on the caveolar membrane. Once we showed the validity of our approach to study with detail the 3D organization of coating on caveolae we proceeded to examine it in the other (until now unexplored) members of the caveolar system in a similar way.

Within the different subpopulations of the caveolar system present in our tomograms of HUVECs, we observed that they each possessed a similar spirally distribution of coat elements, on the membrane of the caveolar necks and bulbs integrating them, as we observed on the *bonafide* caveolae (figures 6.6, Supplementary figure 6.2). In Supplementary Movie 6.2, a 3D overview of the organization of membrane coatings on elements of the caveolar system is presented. Analysis of the 3D distribution of membrane coating related to the architecture of some members of the caveolar system provided some interesting observations. Similar to the *bonafide* caveolae, single-necked caveolar entities were encapsulated by a triad of spirals. However, on double-necked caveolar entities the number of spirals is less defined. In addition, in racemose invaginations we noticed a change in orientation of the spiral specifically related to the neck-area interconnecting caveolae "fused" in tandem (Supplementary figure 6.2). It was striking however, that this orientation-change always caused the angle of the spiral to conform to a 23 degree angle towards the plane of one of the necks. This was observed both in chemically fixed and high-pressure frozen samples. Another striking and unexpected observation was revealed on the surface of multi-caveolar bodies: we observed that the coating arranged in spiral on a caveolar bulb often spanned larger regions on the entire body connecting to the spiral coating on other caveolar bulbs (Supplementary Movie 6.2). This coating arrangement suggests that multi-caveolar bodies are quite stable organelles rather than transient structures.

We report for the first time the presence of a spirally coating on the membrane of all types of

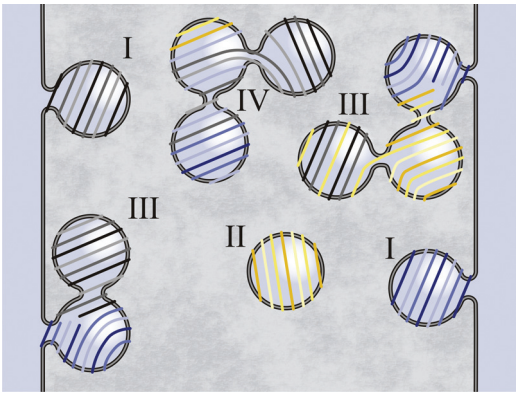


**Figure 6.7. Schematic overview of the membrane coating distribution in the caveolar system.** *Members of the caveolar system are all encapsulated by membrane attached coats in a spirally fashion as described in the past for membrane-hanging caveolae. In this scheme the organization of the coating is summarized. I: bonafide caveolae hanging from the luminal or abluminal plasma membrane are encapsuled by a triad of paralelly organized spirals. II: the same organization of spirals in a triad can be observed covering the bulb of free caveolar vesicles. III & IV: while multi-necked caveolar structures like racemose invaginations and multi-caveolar bodies share parallel spirals that which angle in relationship to the plane of the neck is similar to that of bonafide caveolae, the overall organization of the coat is more complex (changing orientation in relationship to the nearest neck area) and the number of spirals is less defined. Both spirals that encapsulated a single bulb and spirals that crossed the neck and encapsulated areas of multiple bulbs were observed.*

members of the caveolar system in endothelial cells. In figure 6.7 we present a scheme summarizing our findings. The existence of a coating on all these cellular components sets a structural basis for the characteristic unique morphology of caveolae (in their single or clustered form); a feature that during decades was trusted as the only criterion for their identification. Our finding is supported by the demonstration of caveolin, an important component of the caveolar coating (Rothberg et al., 1992), associated to the membrane of the different caveolae-related structures (figure 6.2). In the current study, the use of osmium-impregnated cells (20) was critical to avoid introducing a staining gradient in the *Z* direction of the tomograms that could complicate data interpretation. However, probably the most crucial choice that we made to be able to find the 3D distribution of the caveolar coating was the application of template matching, an objective tool for annotation of tomograms. The combination of cell processing and analysis approaches that we used can explain why we did find the spirally-distribution of coat in tomograms of caveolae while others (Richter et al., 2008), performing excellent tomography of post-stained cells combined with manual tomogram annotation, did not. In spite of our observations, two intriguing questions remain open. One concerns the real composition of the coating that we identified by template matching. Whether the coat elements are specifically caveolin oligomers as previously suggested (Rothberg et al., 1992) or comprises other elements cannot be concluded based on the current results. It is however worth noting that the template that we created - based on coat particles found in our tomograms (figure 6.4) - overlaps the expected dimensions (approximate 10 nm in diameter) of the caveolin oligomers suggested to assemble into caveolin filaments (Fernandez et al., 2002). The other question regards the biogenesis of caveolae and caveolae-related structures in endothelial cells: are all these structures generated from the plasma membrane (as suggested by (Fra et al., 1995)) or are they formed by fusion of single caveolae previously assembled in the Golgi complex (Tagawa et al., 2005)? - The novel observations that we present in this paper fill a gap in current knowledge about the ultrastructural organization of the integral (and complex) caveolar system of endothelial cells. Future work will be necessary to unravel the functional implication of the existence of diverse caveolae-related entities, what promises to be difficult, but exciting.

## Acknowledgements

We thank Miriam Makkinje and Bart de Haan for isolation and culturing of the cells. This work was supported by the Dutch IOP Genomics Project No. IGE03012 and by Cyttron consortium. All calculations were performed at the SARA super computer facilities in Amsterdam.

# CHAPTER VII

## general discussion

# general discussion

Discussion is an exchange of knowledge;
argument an exchange of ignorance.

*Robert Quillen*

Everything in biology and medicine is in some way or another related to cellular organization and function. And cellular organization and function themselves are closely intertwined with membrane organization, (local) composition, and function. Unravelling the mechanisms of life (en disruptions thereof in diseases) is therefore in many cases inseparable from our understanding of cellular membranes. In recent years electron tomography has provided us with new, valuable insights into the organization within, and relationships between membranous compartments of the cell. In addition to the many successes achieved by electron tomography in membrane research, we were confident that by combining three dimensional electron microscopy with three dimensional template matching we could raise the bar for the technique and obtain information hitherto unharvested from electron tomographic volumes. Throughout this thesis I have presented my work on this subject. The current chapter is dedicated to my view of the possibilities and impossibilities of the technique, and its value to cell-biological – and particularly membrane-biological – questions.

## 7.1 Investigating the cell

It is obvious that selecting the right technique for a task is one of the major steps when setting up an experiment; and a technique that is best for one question might not be a suitable solution for another. Biological events take place over space and over time. However, investigating both the spatial and temporal context of such events can mutually exclude the technique of choice: the temporal context is best investigated using (live cell) light microscopy where the spatial resolution is relatively low, while the spatial context is best examined using (three dimensional) high resolution electron microscopy which can only present cellular events at fixed time-points. In many cases a combination of techniques will provide correlative information on both cellular architecture (space) and cellular dynamics (time). However, while correlative microscopy is an interesting and potentially valuable approach in cell-biology, it is only as strong as the techniques used, and continuous development of both temporal and spatial techniques is required. It is my firm believe, that such technical developments in live sciences should be submissive to biological rather than technical questions.

The biological question in view of which the research presented in this thesis was performed is the development and early stages of atherosclerosis. One of the key events in the early stages of this disease is a change in the barrier function of the endothelial layer *(Glass & Witztum, 2001; Lusis et al., 2004)*. This also emerged from the genomics studies performed in view of an IOP project that also the work presented in this thesis was part of. Whether paracytosis, transcytosis, or both lie at the basis of this increase in permeability is still unclear, and within the project one of the goals set out in the project was to improve EM techniques and approaches to study these biomembrane related functions at an ultra-stuctural level. My focus therein was three dimensional electron microscopy – and particularly electron tomography – of high-pressure frozen, freeze substituted samples. This approach was chosen to assure the structural preservation of large cellular systems and components, and allowed us to visualize large continuous caveolar bodies penetrating deeply in the cytoplasm to form a complex caveolar system *(Lebbink et al., in preparation)*. By combining electron tomography with template matching we could semi-objectively visualize membrane heterogeneity *(Lebbink et al., 2009)*, and determine the organization of the caveolar coat throughout the caveolar system *(Lebbink et al., in preparation)*.

## 7.2 Template Matching 1-0-1

Before I get into the possibilities and limitations of the template-matching based electron-tomographic analysis in general, I first want to further discuss the different steps involved in the template matching procedure as described in the different chapters of this thesis, and point out where and how some of these steps can be improved. Such improvements can either concern the technique, user-interaction, or usability.

There are four pieces of software that have become invaluable to me during performing the template

matching described in this thesis: IMOD [Kremer et al., 1996] (now called eTomo), MatLab (with the TOM-Toolbox [Nickell et al., 2005] installed), OmniMatch [Böhm et al., 2000; Frangakis et al., 2002], and Amira 3.1. IMOD is used to reconstruct tomographic tilt-series into a three-dimensional volume. This volume is then pre-processed in MatLab to make it compatible with the OmniMatch software. Also, in MatLab the necessary template- and mask-files are created. OmniMatch is run at the SARA high performance computer facilities in Amsterdam, and thereafter the output is processed by means of several MatLab scripts if necessary. Final visualization is achieved using the tools available in Amira. One of the challenges when using different pieces of software from different companies or scientific groups is, that a lot of file-conversion tends to be necessary, and this is not an exception. While such file-conversion between the .mrc file-format (Imod), and the .em file-format (TOM-toolbox, OmniMatch) is relatively simple, application of the template matching procedure by the 'general public' would require such conversions to be either invisible (automated) or unnecessary (where all software is compatible with the same file-format).

In the introduction-chapter, I've discussed the fundamental basics of electron tomography. In light of the template matching procedure, it is obvious that advances in electron tomography will affect the quality of the matching as well. Within the experiments presented throughout this thesis, we've applied template matching to reconstructions obtained by weighted back-projection as implemented in Imod. Clearly, the approach is however not limited tomographic volumes obtained in such a manner, as it is independent of the acquisition-method, and the technique can be used in collaboration with image enhancement filters that increase the visibility of the structures present in tomographic volumes. It should be noted though, that such filters modify the content of the tomographic volume to make certain features better visible, which might cause artefacts, but also often obscures ultra-structural information while increasing the signal-to-noise ratio. Consequently, such pre-matching filters might be useful when using template matching to extract general features, but should be avoided when ultra-structural analysis is required.

Besides the tomographic volume, OmniMatch requires a template, template-mask, and point-spread function. The template contains a three-dimensional image that describes the structure of interest. There are different approaches to obtain such a template. In the original proof-of-concept paper by Frangakis et al. [Frangakis et al., 2002], template matching was used as a tool to localize and identify cytoplasmic macromolecules within a simplified closed system. Since the identity of these macromolecules was known, and their crystal structure was available, it was possible to adjust the resolution of these known structures to that of the electron microscopic 3D reconstruction, and to obtain the grey values of each voxel by summation of the atomic number of all atoms positioned in it. This is probably the preferred approach when the goal is to localize a known protein with a known structure (whether obtained by crystallography or single-particle analysis does not matter, although the pre-processing steps will be different) that is homogeneous in appearance. For many research questions in electron tomography, however, this does not apply, since the nature of the investigated structures is not compatible with such structural analysis methods, as they are large highly dynamic multi-molecular complexes (including membranes). An alternative approach to obtain a template for such questions could be to extract it directly from the tomogram investigated. If, for example, your research question is to localize and identify both COP- and clathrin-coated vesicles within a golgi-system, a logical and viable approach would be to extract a representative example of either type of vesicle, remove background structures, and run the algorithm. In the current example, clathrin coated budding profiles would be excluded. However, to include them, the protocol can easily be adapted by using only a small section of the coated membrane and rotate the template to detect every clathrin-coated membrane-stretch in the tomogram. While each of the aforementioned methods is valuable it leaves relatively little room for a controlled modification of the template-structure. Throughout this thesis we've used a different approach: we've

created simplified representations of the structure of interest. Using such a template might make the matching process less specific, since ultra-structural information is not taken into account. However, the advantage is two-fold: first of all, highly diverse structures that share an overall morphological similarity (like stretches of membrane) can be identified by this 'general' template, and secondly, the shape of the template is controlled, and can be altered in a controlled fashion. This implies that a single property (like membrane thickness) can be investigated by comparing two templates that differ only in a specific way; differences in matching will be caused by this altered property. This increases the diversity of possible research questions that can be examined by means of template matching and electron tomography.

While the template describes the densities and shape of the structure of interest, it is accompanied by a mask which distinguishes between background and structure within the template. In general, the shape of the mask is directly affected by the shape of the template itself, although in certain cases one may choose to use a spherical mask. This decision is generally based on either of the following: (1) certain versions of OmniMatch do not rotate the mask along with the template and are therefore incompatible with non-spherical masks, (2) it can be difficult to create a binary mask for a complex structure and in such cases a spherical mask may be better applicable, and finally, (3) in certain cases the shape of the template is less important than it's context within the background and a spherical mask is decided upon to include both the structure and its surrounding in the matching process. Since only the voxels of the template that are identified in the mask partake in the matching algorithm, it is important to define a mask that corresponds to the research question; and in most cases this mask will be template specific.

The last input-file for the algorithm is the point-spread function. This function describes the distortion of pixels due to the acquisition of the image. While camera-properties play a general role in the description of the point-spread function, the missing wedge/cone artefact (due to a technically limited number of angles in the tilt-series) is the major component of the distortion in electron tomographic reconstructions. An important property of the missing wedge/cone is that it is a direction specific artefact that can be recognized as blurring of the structure along a certain angle (as shown in figure 1.6 of the introduction). Consequently, a structure in the tomogram will have a slightly different appearance depending on its orientation. The reasoning behind including the point-spread function in the calculation is to cope with these different appearances of the same structure: by convoluting the template structure with the point-spread function after the prior was rotated, the modified template will provide a better representation of the same structure in the same orientation in the tomogram. Nevertheless, we reasoned that when the matching results of two templates are compared, they are affected by the same artefact in the same manner. Consequently, the implementation of the point-spread function can be ignored for such research questions. We therefore decided within the experiments performed throughout this thesis, to use an 'ideal' point-spread function (that did not take any pixel-distortions into account). However, in theory the inclusion of the point-spread function could enhance the recognition capabilities of the template matching algorithm. And while early tests with a description of the missing wedge/cone in the point-spread function-file, did not provide better matching results, we might want to revisit this possibility again in the future. Ideally the point-spread function is created alongside the tomogram and is based on the back-projection angles obtained during the reconstruction. One advantage would be that such a point-spread function might be created automatically, while another is that it would describe the specific missing-wedge/cone artefact as present in the tomogram.

The template matching algorithm itself is calculation-time consuming and to ensure usability (and because the current instalment of the policy of use of the supercomputer does not allow for calculations beyond a limited number of calculation-hours), calculation time has to be reduced in three ways: firstly, if possible the tomogram is cropped to the area of interest, secondly, parallel computing

is used by uploading the four files (the tomographic volume, template, mask, and point-spread function) to the SARA supercomputer facilities computer grid, and finally, the number of angles over which the template is rotated is reduced. Reducing the matching-angles is always a trade-off between accuracy and speed, because each angle greatly increases calculation time, but at the same time template matching achieves the best results when the angle of the template and the structure in the tomogram line up. The optimal number of angles depends on the shape and complexity of the structure described in the template. If the structure is a sphere, there is no need for the algorithm to rotate the template at all, since every rotation results in a repetition of the previous shape. In the case of a cube such a repetition occurs after ninety degrees, and for a cuboid after 180 degrees. As a result, rather than rotating over 360x360x360 (46656000) degrees a cuboid-shaped membrane template has 180x180x1 (32400) original rotation angles before repetition takes place. However, even at SARA - using 54 CPU's - such a calculation would still take considerable time, and further reduction of angles is required. This can be achieved by applying an increment of ten degrees which leads to 18x18x1 (324) original rotation angles thus reducing calculation time to a few hours. With advances in computer-power, many of these restrictions (of which the limited angles is the most severe) will likely vanish in the future; however, even if you could rotate every sample over 360 degrees with a one degree increment doesn't mean you should do it, and optimization of calculation-time should always be a concern.

While support of the supercomputer facilities is a necessity for the current research, advances can be made to make the user interaction more streamlined and less error-prone. Currently, all commands are given either through typing in the shell-console, or by means of text-files containing the job-descriptions. Some initial attempts were made to implement a graphical user interface that would allow OmniMatch to run as a component on the cluster, and such an implementation would significantly improve user-interaction and -friendliness. Future advances in this area will greatly open up the template matching procedure to the 'general public'.

When the algorithm is finished, two files are created: the cross-correlation files which contains the matching values of each voxel, and the angle-file which contains the orientation of the structure in the tomographic volume (related to the template). The experiments described in this thesis are essentially localization studies, in which only the cross-correlation file was obtained, while the angle-file was not taken into account. Inclusion of the angle-file might advance the technique in a number of ways: in theory small gaps (false negative matchings) in the recognition of a continuous structures could be 'filled' by predicting the path of the structure. Such a prediction would be the extrapolation of the preceding path of the structure, which can be deduced from the location and the orientation of the structure. Of course the greater the gap the less accurate such an extrapolation would be. It should be noted though that filling gaps is not a trivial task, and would require the construction of new additional tools. Another possible use of the angle-file would be to screen for false positive matches of a continuous structure in the cross-correlation map. Similar to predicting the path of the structure of fill gaps, it should theoretically be possible to mark areas where the continuous structure radically changes its direction. While such directional changes do occur in the cellular membrane, non-sense changes are likely to indicate a false positive matching. Even more than the filling of gaps, this is not a trivial task, and additional tools will have to be created specifically for this purpose. A third application of the angle-file – which is already possible with the tools at hand – is to 'stamp' a small representation of the structure (either the same as, or distinct from the matched template) at the found location in the correct orientation in a new volume. The advantage of this approach is most obvious for non-streak-like structures (like the microtubules in chapter 3): based on the cross-correlation file alone such a structure is represented by a small line. However, if the corresponding template were to be pasted on top of it, the visualized representation would show a tube rather than a line. There are two reasons why this

possibility did not yet find solid ground in our experiments. First of all, membranes – which we focus on mainly - are commonly presented as streaks in electron tomographic models, so people are used to look at them is such a way; changing their appearance would therefore add nothing but confusion. The second reason is that to accurately stamp the template in the correct orientation, would require us to use a smaller increment than we currently use, and would therefore significantly increase calculation time. However, since its implementation is relatively simple (and since all tools necessary to implement it are already available) this is a valuable approach to explore in the future, when it is called for by a biological question.

To summarize, choosing the right parameters, processing steps, and files are of vital importance to obtain good results by template matching of electron tomographic samples. As with any technique, however, the decisions made have to be in service of the biological question or the results may be irrelevant.

## 7.3 Limitations, Possibilities, and Challenges

Despite the possible advances described in the previous sections, I do not think that template matching is the Holy Grail of tomographic volume annotation techniques; like every technique it has its strengths and weaknesses. Within this thesis I have shown that for certain questions three dimensional template matching can acquire additional and valuable information that can not be extracted from the tomographic volume by means of manual annotation. However, one of our original ideas was not only to explore template matching as an addition to, but rather as an alternative for manual segmentation. The results of this are presented in chapter three.

From these and later experiences I do not feel that template matching on its own will completely replace manual segmentation. This is, because template matching is 'all muscles, no brain'. To explain what I mean, I go back to my analogy with the Cinderella story. During the dance the prince noticed at least three things (he noticed some other things too, but I won't go into that): firstly, the mysterious girl was a women, secondly, on heels she was about five centimetres shorter than the prince, and thirdly, she had the most stunning hazel-brown eyes he had every seen. When he set forth in search for this girl, it makes perfect sense to include these properties: if a girl is longer than the prince, or if she has blue eyes, it doesn't matter whether the template fits or not, because she's not the girl he is looking for. However, template matching does not take any of the additional knowledge - any of the context of the template – into account. If the prince would apply the template matching method he would scan every inhabitant of his kingdom independent of their lengths, eye colour, or gender marking all people who match. This will of course result in a lot of false positives. Similarly, if there's only one girl in the country with hazel-brown eyes who is (on heels) 1.76 meters tall, chances are that this is the girl the prince is looking for, even if the shoe fits 'only' quite well but not perfectly. The same is true for template matching of electron tomographic volumes of biological structures: there is a lot of knowledge we have on the structures visible in micrographs which at the moment is not taken into account by the matching-algorithm. To achieve such a context-aware approach by implementing a near infinite number of possible parameters per template is not the answer, for it will not only substantially increase calculation time, but also render the software pretty much unusable for the user who has to set these parameters. Alternatively, to achieve a context aware approach, an adaptive/learning algorithm would be a better approach. Theoretically this could be achieved through the implementation of an iterative application of the template matching procedure which continuously modifies and optimizes the template and relates the location and orientation of this optimized template to the location and orientation of the same (or another) template. Still this would significantly increase calculation time since despite the implementation of some brains, the muscle is still the major component of the algorithm. One advantage of such an iterative process would be that – at least in theory – it should be possible to split the

process up between iterations, which would allow for calculations that take a longer time than the limit of the supercomputer facilities. An alternative route would be to implement a neural network to 'learn' to recognize the structure of interest. The initial learning stage could be achieved in combination with template matching to teach the algorithm what the pattern of interest looks like (neural networks tend to recognize patterns rather than objects). The advantage of such a neural network approach is that it is more brains and less muscle. The downsides are however, that you can never know what it is the algorithm learned to recognize exactly, that if the learning stage is wrong you teach it the wrong thing, and that once something is wrong you can't simply correct it, but have to teach it all over again. It should be noted though, that neither of these theoretical approaches is compatible with the use of template matching to compare the difference between two controlled templates, because the nature of the templates for each of these techniques would be highly dynamic and adaptive.

Another limitation of template matching is, that identification of structures only applies to relatively small structures of an homogeneous appearance. So while it can be used to annotate membranes, as was shown in this thesis, the identification of the organelle such membranes are part of is not possible. In theory of course both of the before mentioned approaches – and particularly a neural network - might also solve this limitation. In general we recognize organelles by means of context, shape, intensities, and relationships to other organelles, resulting in an extremely complex set of parameters and variables. Due to its nature, however, such patterns might be taught to a neural network (at least in theory).

Despite all points raised above, which show that template matching is still limited in certain ways, we have shown throughout our work that a lot can be achieved already. Template matching is particularly useful to a certain niche of cell-biological questions in electron tomography. The general term of this niche would be 'location and/or orientation'-studies; which corresponds to the two output files created by the algorithm. It was originally developed to localize and distinguish proteins within a (cryo-)tomographic volume. However, whether this concept is generally feasible within the 'crowded' environment of the cellular cytoplasm is debatable of course. Within the IOP genomics project we were interested in membrane heterogeneity which could be related to the dynamic processes involved in the onset and early stages of atherosclerosis. Since the barrier function of the endothelial cell-layer is altered in atherosclerotic-plaques, one of the goals is to compare the ultra-structural membrane organization of specific organelles (caveolae) in healthy and affected cells. To achieve this we had to advance each of the techniques involved (not only electron tomography and template matching, but as a group also the FIB-SEM, sample preparation, membrane staining, etc.) in small – and sometimes tiny – steps; each of which would be invaluable to answer the original question. As a group we have brought these techniques to a new level, and are now in a position that the problem addressed above can be tackeled. Of course template matching based annotation of electron tomographic samples is not limited to our biological question. We have shown that it is possible to apply template matching to the questions of membrane heterogeneity and transcytosis. By combining the strengths of electron tomography and template matching we were able to unravel some of the complexities of the caveolar system in endothelial cells, and could both visualize membrane connections and continuities, and reveal the organization of the caveolar coat as a triad of parallel spirals throughout the entire system; something which was beyond the reach of manual annotation alone.

Supplementary movies are available at:
**http://www.electronmicroscopy.nl/moviegallery/moviegallery.html**

## *Chapter II - FIB-SEM: an in-depth study of atherosclerotic tissue*

*Supplementary movie 2.1.*
The movie shows a sequence of images that were acquired at the plaque area during the slice and view series. In intracellular distribution of the lipid droplets within the foam cell located underneath the endothelium can be clearly distinguished. It can be observed that the lipid droplets are present within the nuclear plane and thus cause deformations of the nucleus.

## *Chapter VI - template matching reveals a spiral coating on the membranes of the caveolar system in endothelial cells*

*Supplementary movie 6.1*
Overview of the caveolar system. A double-tilted serial tomogram of high-pressure frozen, non-poststained HUVECs giving an overview of the caveolar system in endothelial cells.

*Supplementary movie 6.2*
Spirally distribution of membrane coating on a multi-caveolar body processed by high pressure freezing/freeze-substitution.

# bibliography

# bibliography

He who does not read will not be read. he who does not quote will not be quoted. he who does not use the thoughts of other men's brains proves he has no brains of his own.

*Charles H. Spurgeon*

**Agronskaia, A.V. · Valentijn, J.A. · van Driel, L.F. · Schneijdenberg, C.T.W.M. · Humbel, B.M. · van Bergen En Henegouwen, P.M.P. · Verkleij, A.J. · Koster, A.J. · Gerritsen, H.C. (2008)**
Integrated fluorescence and transmission electron microscopy. *Journal of Structural Biology* doi:10.1016/j.jsb.2008.07.003

**Amira**
http://www.amiravis.com

**Anderson, R.G. (1998)**
The caveolae membrane system. *Annual review of biochemistry* **67**:199-225

**Arslan, I. Yates, T.J.V. Browning, N.D. Midgley, P.A. (2005)**
**Embedded nanostructures revealed in three dimensions.** *Science* 309:2195-8

**Arslan, I. · Tong, J.R. · Midgley, P.A. (2006)**
Reducing the missing wedge: High-resolution dual axis tomography of inorganic materials. *Ultramicroscopy* **106**:994-1000

**Baumeister, W. · Grimm, R. · Walz, J. (1999)**
Electron tomography of molecules and cells. *Trends in Cell Biology* **9**:81-5

**Beck, M. · Förster, F. · Ecke, M. · Plitzko, J.M. · Melchior, F. · Gerisch, G. · Baumeister, W. · Medalia, O. (2004)**
Nuclear pore complex structure and dynamics revealed by cryoelectron tomography. *Science 306*:1387-90

**Bennett, P.M. (1974)**
Decrease in section thickness on exposure to the electron beam; the use of tilted sections in estimating the amount of shrinkage. *Journal of Cell Science* **15**:693-701

**Beorchia, A. · Heliot, L. · Menager, M. · Kaplan, H. · Ploton, D. (1993)**
Applications of medium-voltage STEM for the 3-D study of organelles within very thick sections. *Journal of Microscopy* **170**:247-58

**Böhm, J. · Frangakis, A.S. · Hegerl, R. · Nickell, S. · Typke, D. · Baumeister, W. (2000)**
Toward detecting and identifying macromolecules in a cellular context: template matching applied to electron tomograms. *Proceedings of the National Academy of Sciences of the United States of America* **97**:4245-50

**Bretscher, M.S. · Munro, S. (1993)**
Cholesterol and the Golgi apparatus. *Science* **261**:1280-1

**Brown, D.A. · London, E. (1997)**
Structure of detergent-resistant membrane domains: does phase separation occur in biological membranes? *Biochemical and Biophysical Research Communications* **240**:1-7

**Bruns, R.R. · Palade, G.E.(1968)**
Studies on blood capillaries. I. General organization of blood capillaries in muscle. *The Journal of Cell Biology* **37**:244-76

**Bundgaard, M. (1991)**
The three-dimensional organization of smooth endoplasmic reticulum in capillary endothelia: its possible role in regulation of free cytosolic calcium. *Journal of Structural Biology* **107**:76-85

**Bundgaard, M. · Hagman, P. · Crone, C. (1983)**
The three-dimensional organization of plasmalemmal vesicular profiles in the endothelium of rat heart capillaries. *Microvascular Research* **25**:358-68

**van Buul, J.D. · Kanters, E. · Hordijk, P.L. (2007)**
Endothelial signaling by Ig-like cell adhesion molecules. Arteriosclerosis, *Thrombosis, and Vascular Biology* **27**:1870-6

**Carlemalm, E. · Kellenberger, E. (1982)**
The reproducible observation of unstained embedded cellular material in thin sections: visualisation of an integral membrane protein by a new mode of imaging for STEM. *The EMBO Journal* **1**:63-7

**Chen, H. · Clyborne, W.K. · Sedat, J.W. · Agard, D.A. (1992)**
PRIISM: an integrated system for display and analysis of 3-D microscope images. *Biomedical Image Processing and Three-Dimensional Microscopy* **1660**:784-90

**Chen, H. · Hughes, D.D. · Chan, T.A. · Sedat, J.W. · Agard, D.A. (1996)**
IVE (Image Visualization Environment): a software platform for all three-dimensional microscopy applications. *Journal of Structural Biology* **116**:56-60

**Chien, S. · Laufer, L. · Handley, D.A. (1982)**
Vesicle distribution in the arterial endothelium determined with ruthenium red as an extracellular marker. *Journal of Ultrastructure Research* **79**:198-206

**Danielli, J.F. · Davson, H. (1935)**
A contribution to the theory of permeability of thin films. *Journal of Cellular and Comparative Physiology* **5**:495–508

**Diez, D.C. · Seybert, A. · Frangakis, A.S. (2006)**
Tilt-series and electron microscope alignment for the correction of the non-perpendicularity of beam and tilt-axis. *Journal of Structural Biology* **154**:195-205

**van Driel, L.F. · Knoops, K. · Koster, A.J. · Valentijn, J.A. (2008)**
Fluorescent labeling of resin-embedded sections for correlative electron microscopy using tomography-based contrast enhancement. *Journal of structural biology* **161**:372-83

**Dvorak, A.M. · Feng, D. (2001)**
The vesiculo-vacuolar organelle (VVO). A new endothelial cell permeability organelle. *The Journal of Histochemistry and Cytochemistry* **49**:419-32

**Egerton, R.F. · Li, P. · Malac, M. (2004)**
Radiation damage in the TEM and SEM. *Micron* **35**:399-409

**Eman, M.R. · Regan-Klapisz, E. · Pinkse, M.W.H. · Koop, I.M. · Haverkamp, J. · Heck, A.J.R. · Verkleij, A.J. · Post, J.A. (2006)**
Protein expression dynamics during replicative senescence of endothelial cells studied by 2-D difference in-gel electrophoresis. *Electrophoresis* **27**:1669-82

**Engel, A. · Wiggins, J.W. · Woodruff, D.C. (1974)**
A comparison of calculated images generated by six modes of transmission electron microscopy. *Journal of Applied Physics* **45**:2739-47

**Esser, S. · Wolburg, K. · Wolburg, H. · Breier, G. · Kurzchalia, T. · Risau, W. (1998)**
Vascular endothelial growth factor induces endothelial fenestrations in vitro. *The Journal of Cell Biology* **140**:947-59

**Fernandez, I. · Ying, Y. · Albanesi, J. · Anderson, R.G.W. (2002)**
Mechanism of caveolin filament assembly. *Proceedings of the National Academy of Sciences of the United States of America* **99**:11193-8

**Fra, A.M. · Williamson, E. · Simons, K. · Parton, R.G. (1995)**
De novo formation of caveolae in lymphocytes by expression of VIP21-caveolin. *Proceedings of the National Academy of Sciences of the United States of America 92*:8655-9

**Frangakis, A.S. · Hegerl, R. (2001)**
Noise reduction in electron tomographic reconstructions using nonlinear anisotropic diffusion. *Journal of Structural Biology* **135**:239-50

**Frangakis, A.S. · Stoschek, A. · Hegerl, R. (2001)**
Wavelet transform filtering and nonlinear anisotropic diffusion assessed for signal reconstruction performance on multidimensional biomedical data. *IEEE Transactions on Bio-Medical Engineering* **48**:213-22

**Frangakis, A.S. · Bohm, J. · Förster, F. · Nickell, S. · Nicastro, D. · Typke, D. · Hegerl, R. · Baumeister, W. (2002)**
Identification of macromolecular complexes in cryoelectron tomograms of phantom cells. *Proceedings of the National Academy of Sciences of the United States of America* **99**:14153-8

**Frank, J. (1995)**
Approaches to large-scale structures. *Current opinion in structural biology* **5**:194-201

**Frey, T.G. · Perkins, G.A. · Ellisman, M.H. (2006)**
Electron tomography of membrane-bound cellular organelles. *Annual Review of Biophysics and Biomolecular Structure* **35**:199-224

**Geuze, H.J. · Murk, J.L.A.N. · Stroobants, A.K. · Griffith, J.M. · Kleijmeer, M.J. · Koster, A.J. · Verkleij, A.J. · Distel, B. · Tabak, H.F. (2003)**
Involvement of the endoplasmic reticulum in peroxisome formation. *Molecular biology of the cell* **14**:2900-7

**Giepmans, B.N.G. (2008)**
Bridging fluorescence microscopy and electron microscopy. *Histochemistry and Cell Biology* **130**:211-7

**Gilbert, P. (1972)**
Iterative methods for the three-dimensional reconstruction of an object from projections. *Journal of Theoretical Biology* **36**:105-117

**Glass, C.K. · Witztum, J.L. (2001)**
Atherosclerosis. the road ahead. *Cell* **104**:503-16

**Gorter, E. · Grendel, F. (1925)**
On bimolecular layers of lipoids on the chromocytes of the blood.*Journal of Experimental Medicine* **41**:439-443

**Griffiths, G. (1993)**
Fine Structure Immunocytochemistry. (*Springer-Verlag*: Berlin Heidelberg New York. ISBN:0-387-54805-X).

**Henderson, R. · Unwin, P.N. (1975)**
Three-dimensional model of purple membrane obtained by electron microscopy. Nature 257, 28-32

**Heymann, J.A.W. · Hayles, M. · Gestmann, I. · Giannuzzi, L.A. · Lich, B. · Subramaniam, S. (2006)**
Site-specific 3D imaging of cells and tissues with a dual beam microscope. Journal of Structural Biology 155, 63-73

**Hooke, R. (1665)**
Micrographia: or some physiological descriptions of minute bodies made by magnifying glasses : with observations and inquiries thereupon. 112-121 (*Royal Society: London*).
available at: http://digital.library.wisc.edu/1711.dl/HistSciTech.HookeMicro

**Hoppe, W. · Hegerl, R. (1980)**
Computer Processing of Electron Microscope Images, Hawkes, P.W. (Ed.). (*Springer Verlag*: Berlin Heidelberg New York. ISBN:0-387-09622-1).

**Inkson, B.J. · Mulvihill, M. · Möbus, G. (2001)**
3D determination of grain shape in a FeAl-based nanocomposite by 3D FIB tomography. *Scripta Materialia* **45**:753-758

**Jiménez, N. · Humbel, B.M. · van Donselaar, E. · Verkleij, A.J. · Burger, K.N.J. (2006)**
Aclar discs: a versatile substrate for routine high-pressure freezing of mammalian cell monolayers. *Journal of Microscopy* **221**:216-23

**Jiménez, N. · Vocking, K. · van Donselaar, E.G. · Humbel, B.M. · Post, J.A. · Verkleij, A.J. (2009)**
Tannic acid-mediated osmium impregnation after freeze-substitution: a strategy to enhance membrane contrast for electron tomography. *Journal of Structural Biology* **166**:103-6

**Karreman, M.A. · Agronskaia, A.V. · Verkleij, A.J. · Cremers, F.F.M. · Gerritsen, H.C. · Humbel, B.M. (2009)**
Discovery of a new RNA-containing nuclear structure in UVC-induced apoptotic cells by integrated laser electron microscopy. *Biology of the Cell* **101**:287-99

**Killian, J.A. (1998)**
Hydrophobic mismatch between proteins and lipids in membranes. *Biochimica Et Biophysica Acta* **1376**:401-15

**Kleijmeer, M.J. · Morkowski, S. · Griffith, J.M. · Rudensky, A.Y. · Geuze, H.J. (1997)**
Major histocompatibility complex class II compartments in human and mouse B lymphoblasts represent conventional endocytic compartments. *The Journal of Cell Biology* **139**:639-49

**Knott, G. · Marchman, H. · Wall, D. · Lich, B. (2008)**
Serial section scanning electron microscopy of adult brain tissue using focused ion beam milling. *The Journal of neuroscience* **28**:2959-64

**Kobayashi, T. · Stang, E. · Fang, K.S. · de Moerloose, P. · Parton, R.G. · Gruenberg, J. (1998)**
A lipid associated with the antiphospholipid syndrome regulates endosome structure and function. *Nature* **392**:193-7

**Kohn, S. · Nagy, J.A. · Dvorak, H.F. · Dvorak, A.M.** (1992)
Pathways of macromolecular tracer transport across venules and small veins. Structural basis for the hyperpermeability of tumor blood vessels. *Laboratory Investigation; a Journal of Technical Methods and Pathology* **67**:596-607

**Koster, A.J. · Grimm, R. · Typke, D. · Hegerl, R. · Stoschek, A. · Walz, J. · Baumeister, W.** (1997)
Perspectives of molecular and cellular electron tomography. *Journal of structural biology* **120**:276-308

**Kremer, J.R. · Mastronarde, D.N. · McIntosh, J.R.** (1996)
Computer visualization of three-dimensional image data using IMOD. *Journal of structural biology* **116**:71-6

**Kubis, A.J. · Shiflet, G.J. · Dunn, D.N. · Hull, R.** (2004)
Focused ion-beam tomography. *Metallurgical and Materials Transactions A* **35A**:1935-1943

**Ladinsky, M.S. · Mastronarde, D.N. · McIntosh, J.R. · Howell, K.E. · Staehelin, L.A.** (1999)
Golgi structure in three dimensions: functional insights from the normal rat kidney cell. *The Journal of Cell Biology* **144**:1135-49

**Lawrence, A. · Bouwer, J.C. · Perkins, G. · Ellisman, M.H.** (2006)
Transform-based backprojection for volume reconstruction of large format electron microscope tilt series. *Journal of Structural Biology* **154**:144-67

**Lebbink, M.N. · Geerts, W.J.C. · van der Krift, T.P. · Bouwhuis, M. · Hertzberger, L.O. · Verkleij, A.J. · Koster, A.J.** (2007)
Template matching as a tool for annotation of tomograms of stained biological structures. *Journal of structural biology* **158**:327-35

**Lebbink, M.N. · van Donselaar, E.G. · Humbel, B.M. · Hertzberger, L.O. · Post, J.A. · Verkleij, A.J.** (2009)
Induced membrane domains as visualized by electron tomography and template matching. *Journal of Structural Biology*. **166**:156-61

**Lebbink, M.N. · Jiménez, N. · Vocking, K. · Hekking, L.H.P. · Verkleij, A.J. · Post, J.A.**
Template matching reveals a spiral coating on the membranes of the caveolar system in endothelial cells. *in preparation*

**Libby, P.** (2002)
Inflammation in atherosclerosis. *Nature* **420**:868-74

**Loane, R.F. · Xu, P. · Silcox, J.** (1992)
Incoherent imaging of zone axis crystals with ADF STEM. *Ultramicroscopy* **40**:121-138

**London, E. · Brown, D.A.** (2000)
Insolubility of lipids in triton X-100: physical origin and relationship to sphingolipid/cholesterol membrane domains (rafts). *Biochimica et biophysica acta* **1508**:182-95

**Lucic, V. · Förster, F. · Baumeister, W.**(2005)
Structural studies by electron tomography: from cells to molecules. *Annual review of biochemistry* **74**:833-65

**Lusis, A.J.** (2000)
Atherosclerosis. *Nature* **407**:233-41

**Lusis, A.J. · Mar, R. · Pajukanta, P.** (2004)
Genetics of atherosclerosis. *Annual Review of Genomics and Human Genetics* **5**:189-218

**Luther, P.K. · Lawrence, M.C. · Crowther, R.A.** (1988)
A method for monitoring the collapse of plastic sections as a function of electron dose. *Ultramicroscopy* **24**:7-18

**Mannella, C.A. · Buttle, K. · Rath, B.K. · Marko, M.** (1998)
Electron microscopic tomography of rat-liver mitochondria and their interaction with the endoplasmic reticulum. *BioFactors* **8**:225-8

**Marsh, B.J. · Volkmann, N. · McIntosh, J.R. · Howell, K.E.** (2004)
Direct continuities between cisternae at different levels of the Golgi complex in glucose-stimulated mouse islet beta cells. *Proceedings of the National Academy of Sciences of the United States of America* **101**:5565-70

**Mastronarde, D.N.** (1997)
Dual-axis tomography: an approach with alignment methods that preserve resolution. *Journal of structural biology* **120**:343-52

**Matlab**
http://www.mathworks.com/

**Mazzarello, P.** (1999)
A unifying concept: the history of cell theory. *Nature Cell Biology* **1**:E13-5

**McEwen, B.F. · Downing, K.H. · Glaeser, R.M.** (1995)
The relevance of dose-fractionation in tomography of radiation-sensitive specimens. *Ultramicroscopy* **60**:357-73

**McEwen, B.F. · Heagle, A.B.** (1998)
Electron microscopic tomography: a tool for probing the structure and function of subcellular components. *International Journal of Imaging Systems and Technology* **8**:175 - 187

**McEwen, B.F. · Marko, M.** (2001)
The emergence of electron tomography as an important tool for investigating cellular ultrastructure. *The Journal of Histochemistry and Cytochemistry* **49**, 553-64

**Medalia, O. · Weber, I. · Frangakis, A.S. · Nicastro, D. · Gerisch, G. · Baumeister, W.** (2002)
Macromolecular architecture in eukaryotic cells visualized by cryoelectron tomography. *Science* **298**:1209-13

**Midgley, P.A. · Weyland, M. · Thomas, J.M. · Johnson, B.F.G.** (2001)
Z-Contrast tomography: a technique in three-dimensional nanostructural analysis based on Rutherford scattering. *Chemical Communications* **10**:907-908

**Midgley, P.A. · Weyland, M.** (2003)
3D electron microscopy in the physical sciences: the development of Z-contrast and EFTEM tomography. *Ultramicroscopy* **96**:413-31

**Milligan, R.A. · Whittaker, M. · Safer, D.** (1990)
Molecular structure of F-actin and location of surface binding sites. *Nature* **348**:217-21

**Mironov, A.A. · Mironov, A.A. · Beznoussenko, G.V. · Trucco, A. · Lupetti, P. · Smith, J.D. · Geerts, W.J.C. · Koster, A.J. · Burger, K.N.J. · Martone, M.E. · Deerinck, T.J. · Ellisman, M.H. · Luini, A.** (2003)
ER-to-Golgi carriers arise through direct en bloc protrusion and multistage maturation of specialized ER exit domains. *Developmental Cell* **5**:583-94

**Möbius, W. · van Donselaar, E. · Ohno-Iwashita, Y. · Shimada, Y. · Heijnen, H.F.G. · Slot, J.W. · Geuze, H.J.** (2003)
Recycling compartments and the internal vesicles of multivesicular bodies harbor most of the cholesterol found in the endocytic pathway. *Traffic* **4**:222-31

**Mogelsvang, S. · Marsh, B.J. · Ladinsky, M.S. · Howell, K.E.** (2004)
Predicting function from structure: 3D structure studies of the mammalian Golgi complex. *Traffic* **5**:338-45

**Mollenhauer, H.H.** (1964)
Plastic embedding mixtures for use in electron microscopy. *Stain Technology* **39**:111-4

**Monson, K.L. · Wall, J.S. · Hainfeld, J.F.** (1987)
Visibility and stability of a 12-tungsten atom complex in the scanning transmission electron microscope. *Ultramicroscopy* **21**:147-56

**Moreau, P. · Cassagne, C.** (1994)
Phospholipid trafficking and membrane biogenesis. *Biochimica Et Biophysica Acta* **1197**:257-90

**Moss, W.C. · Haase, S. · Lyle, J.M. · Agard, D.A. · Sedat, J.W.** (2005)
A novel 3D wavelet-based filter for visualizing features in noisy biological data. *Journal of Microscopy 219*:43-9

**Mouritsen, O.G. · Bloom, M.** (1984)
Mattress model of lipid-protein interactions in membranes. *Biophysical journal* **46**:141-53

**Munro, S.** (1995)
An investigation of the role of transmembrane domains in Golgi protein retention. *The EMBO journal* **14**:4695-704

**Murk, J.L.A.N. Humbel, B.M. Ziese, U. Griffith, J.M. Posthuma, G. Slot, J.W. Koster, A.J. Verkleij, A.J. Geuze, H.J. Kleijmeer, M.J.** (2003)
Endosomal compartmentalization in three dimensions: implications for membrane fusion. *Proceedings of the National Academy of Sciences of the United States of America* **100**:13332-7

**Murk, J.L.A.N. · Posthuma, G. · Koster, A.J. · Geuze, H.J. · Verkleij, A.J. · Kleijmeer, M.J. · Humbel, B.M.** (2003)
Influence of aldehyde fixation on the morphology of endosomes and lysosomes: quantitative analysis and electron tomography. *Journal of Microscopy* **212**:81-90

**Murk, J.L.A.N.** (2004)
3D Analysis of Endosomes, Lysosomes and Peroxisomes. (*Utrecht University*. ISBN:90-393-3644-X).

**Murk, J.L.A.N. · Lebbink, M.N. · Humbel, B.M. · Geerts, W.J.C. · Griffith, J.M. · Langenberg, D.M.L. · Verreck, F.A.W. · Verkleij, A.J. · Koster, A.J. · Geuze, H.J. · Kleijmeer, M.J.** (2004)
3-D Structure of multilaminar lysosomes in antigen presenting cells reveals trapping of MHC II on the internal membranes. *Traffic* **5**:936-45

**Nakashima, Y. · Raines, E.W. · Plump, A.S. · Breslow, J.L. · Ross, R.** (1998)
Upregulation of VCAM-1 and ICAM-1 at atherosclerosis-prone sites on the endothelium in the ApoE-deficient mouse. *Arteriosclerosis, Thrombosis, and Vascular Biology* **18**:842-51

**Nezil, F.A. · Bloom, M.** (1992)
Combined influence of cholesterol and synthetic amphiphillic peptides upon bilayer thickness in model membranes. *Biophysical Journal* **61**:1176-83

**Nickell, S. · Förster, F. · Linaroudis, A. · Net, W.D. · Beck, F. · Hegerl, R. · Baumeister, W. · Plitzko, J.M.** (2005)
TOM software toolbox: acquisition and analysis for electron tomography. *Journal of Structural Biology* **149**:227-34

**Ohtsuki, M.** (1980)
Observation of unstained biological macromolecules with the STEM. *Ultramicroscopy* **5**:317-323

**Oorschot, V. · de Wit, H. · Annaert, W.G. · Klumperman, J.** (2002)
A novel flat-embedding method to prepare ultrathin cryosections from cultured cells in their in situ orientation. *The Journal of Histochemistry and Cytochemistry* **50**:1067-80

**Otten, M.T. · Stenzel, D.J. · Cousens, D.R. · Humbel, B.M. · Leunissen, J.L.M. · Stierhof, Y.D. · Busing, W.M.** (1992)
High angle annual dark-field STEM imaging of immunogold labels. *Scanning* **14**:282

**Overath, P. · Brenner, M. · Gulik-Krzywicki, T. · Shechter, E. · Letellier, L.** (1975)
Lipid phase transitions in cytoplasmic and outer membranes of Escherichia coli. *Biochimica et Biophysica Acta - Biomembranes* **389**:358-369

**Overton, E.** (1901)
Studien über die Narkose zugleich ein Beitrag zur allgemeinen Pharmakologie. (*Gustav Fischer Verlag*: Jena).

**Palade, G.E.** (1953)
Fine structure of blood capillaries. *Journal of Applied Physics* **24**:1424

**Palade, G.E.** (1961)
Blood capillaries of the heart and other organs. *Circulation* **24**:368-88

**Palade, G.E. · Bruns, R.R.** (1968)
Structural modulations of plasmalemmal vesicles. *The Journal of Cell Biology* **37**:633-49

**Penczek, P. · Marko, M. · Buttle, K. · Frank, J.** (1995)
Double-tilt electron tomography. *Ultramicroscopy* **60**:393-410

**Penczek, P.A. · Frank, J. · Spahn, C.M.T.** (2006)
A method of focused classification, based on the bootstrap 3D variance analysis, and its application to EF-G-dependent translocation. *Journal of Structural Biology* **154**:184-94

**Pennycook, S.J. · Nellist, P.D.** (1999)
Impact of Electron and Scanning Probe Microscopy on Materials, Rickerby D. G., Valdrè G., Valdrè, U. (Eds). 161-207 (*Kluwer Academic*: Netherlands. ISBN:978-0-7923-5940-1).

**Peters, K.R. · Carley, W.W. · Palade, G.E.** (1985)
Endothelial plasmalemmal vesicles have a characteristic striped bipolar surface structure. *The Journal of cell biology* **101**:2233-8

**Pfeffer, S.** (2003)
Membrane domains in the secretory and endocytic pathways. *Cell* **112**:507-17
**Post, J.A. · Verkleij, A.J. · Langer, G.A.** (1995)
Organization and function of sarcolemmal phospholipids in control and ischemic/reperfused cardiomyocytes. *Journal of Molecular and Cellular Cardiology* **27**:749-60

**Predescu, S.A. · Predescu, D.N. · Palade, G.E.** (1997)
Plasmalemmal vesicles function as transcytotic carriers for small proteins in the continuous endothelium. *The American Journal of Physiology* **272**:H937-49

**Predescu, S.A. · Predescu, D.N. · Shimizu, K. · Klein, I.K. · Malik, A.B.** (2005)
Cholesterol-dependent syntaxin-4 and SNAP-23 clustering regulates caveolar fusion with the endothelial plasma membrane. *The Journal of Biological Chemistry* **280**:37130-8

**Predescu, S.A. · Predescu, D.N. · Malik, A.B.** (2007)
Molecular determinants of endothelial transcytosis and their role in endothelial permeability. *American Journal of Physiology. Lung Cellular and Molecular Physiology* **293**:L823-42

**Quinn, P.J.** (1989)
Principles of membrane stability and phase behavior under extreme conditions. *Journal of bioenergetics and biomembranes* **21**:3-19

**Raetz, C.R.H. · Whitfield, C.** (2002)
Lipopolysaccharide endotoxins. *Annual review of biochemistry* **71**:635-700

**Raposo, G. · Tenza, D. · Murphy, D.M. · Berson, J.F. · Marks, M.S.** (2001)
Distinct protein sorting and localization to premelanosomes, melanosomes, and lysosomes in pigmented melanocytic cells. *The Journal of Cell Biology* **152**:809-24

**Reeves, P.R. · Hobbs, M. · Valvano, M.A. · Skurnik, M. · Whitfield, C. · Coplin, D., Kido · N., Klena, J. · Maskell, D. · Raetz, C.R. · Rick, P.D.** (1996)
Bacterial polysaccharide synthesis and gene nomenclature. *Trends in microbiology* **4**:495-503

**Reynolds, E.S.** (1963)
The use of lead citrate at high pH as an electron-opaque stain in electron microscopy. *The Journal of cell biology* **17**:208-12

**Richter, T. · Floetenmeyer, M. · Ferguson, C. · Galea, J. · Goh, J. · Lindsay, M.R. · Morgan, G.P. · Marsh, B.J. · Parton, R.G.** (2008)
High-resolution 3D quantitative analysis of caveolar ultrastructure and caveola-cytoskeleton interactions. *Traffic* **9**:893-909

**Robertson, J.D.** (1959)
The ultrastructure of cell membranes and their derivatives. *Biochemical Society Symposium* **16**:3-43

**Robertson, J.D.** (1981)
Membrane structure. *The Journal of Cell Biology* **91**:189s-204s

**De Rosier, D.J. · Klug, A.** (1968)
Reconstruction of Three Dimensional Structures from Electron Micrographs. *Nature* **217**:130-4

**Roth, T.F. · Porter, K.R.** (1964)
Yolk protein uptake in the oocyte of the mosquito Aedes qegypti. L. *The Journal of cell biology* **20**:313-32

**Rothberg, K.G. · Heuser, J.E. · Donzell, W.C. · Ying, Y.S. · Glenney, J.R. · Anderson, R.G.** (1992)
Caveolin, a protein component of caveolae membrane coats. *Cell* **68**:673-82

**Rottem, S. · Leive, L.** (1977)
Effect of variations in lipopolysaccharide on the fluidity of the outer membrane of Escherichia coli. *The Journal of Biological Chemistry* **252**:2077-81

**Sachse, M. · Urbé, S. · Oorschot, V. · Strous, G.J. · Klumperman, J.** (2002)
Bilayered clathrin coats on endosomal vacuoles are involved in protein sorting toward lysosomes. *Molecular Biology of the Cell* **13**:1313-28

**Sánchez, F.A. · Kim, D.D. · Durán, R.G. · Meininger, C.J. · Durán, W.N.** (2008)
Internalization of eNOS via caveolae regulates PAF-induced inflammatory hyperpermeability to macromolecules. *American Journal of Physiology. Heart and Circulatory Physiology* **295**:H1642-8

**Sandvig, K. · Torgersen, M.L. · Raa, H.A. · van Deurs, B.** (2008)
Clathrin-independent endocytosis: from nonexisting to an extreme degree of complexity. *Histochemistry and Cell Biology* **129**:267-76

**Schliwa, M. · van Blerkom, J. · Porter, K.R.** (1981)
Stabilization and the cytoplasmic ground substance in detergent-opened cells and a structural and biochemical analysis of its composition. *Proceedings of the National Academy of Sciences of the United States of America* **78**:4329-33

**Schwarz, H. · Humbel, B.M.** (2007)
Correlative light and electron microscopy using immunolabeled resin sections. *Methods in Molecular Biology* **369**:229-56

**Simionescu, N. · Siminoescu, M. · Palade, G.E.** (1975)
Permeability of muscle capillaries to small heme-peptides. Evidence for the existence of patent transendothelial channels. *The Journal of Cell Biology* **64**:586-607

**Simionescu, N.** (1983)
Cellular aspects of transcapillary exchange. *Physiological Reviews* **63**:1536-79

**Simons, K. · van Meer, G.** (1988)
Lipid sorting in epithelial cells. *Biochemistry* **27**:6197-202

**Simons, K. · Ikonen, E.** (1997)
Functional rafts in cell membranes. *Nature* **387**:569-72

**Singer, S.J. · Nicolson, G.L.** (1972)
The fluid mosaic model of the structure of cell membranes. *Science* **175**:720-31

**Singer, S.J.** (2004)
Some early history of membrane molecular biology. *Annual Review of Physiology* **66**:1-27

**Smondyrev, A.M. · Berkowitz, M.L.** (1999)
Structure of dipalmitoylphosphatidylcholine/cholesterol bilayer at low and high cholesterol concentrations: molecular dynamics simulation. *Biophysical Journal* **77**:2075-89

**Stierhof, Y.D. · Humbel, B.M. · Hermann, R. · Otten, M.T. · Schwarz, H.** (1992)
Direct visualization and silver enhancement of ultra-small antibody-bound gold particles on immunolabelled ultrathin resin sections. *Scanning Microscopy* **6**:1009-1022

**Stierhof, Y.D. · Hermann, R. · Humbel, B.M. · Schwarz, H.** (1995)
Use of TEM, SEM, and STEM in imaging 1-nm colloidal gold particles. in: Immunogold-Silver Staining: Principles, Methods, and Applications, Heyat M.A. (Ed). 97-118(*CRC Press*. ISBN:0-8493-2449-1).

**Sztul, E. · Lupashin, V.** (2006)
Role of tethering factors in secretory membrane traffic. American Journal of Physiology. *Cell Physiology* **290**:C11-26

**Tagawa, A. · Mezzacasa, A. · Hayer, A. · Longatti, A. · Pelkmans, L. · Helenius, A.** (2005)
Assembly and trafficking of caveolar domains in the cell: caveolae as stable, cargo-triggered, vesicular transporters. *The Journal of Cell Biology* **170**:769-79

**Terzakis, J.A.** (1968)
Uranyl acetate, a stain and a fixative. *Journal of ultrastructure research* **22**:168-84

**Thorn, H. · Stenkula, K.G. · Karlsson, M. · Ortegren, U. · Nystrom, F.H. · Gustavsson, J. · Stralfors, P.** (2003)
Cell surface orifices of caveolae and localization of caveolin to the necks of caveolae in adipocytes. *Molecular Biology of the Cell* **14**:3967-76

**von der Thüsen, J.H. · van Berkel, T.J. · Biessen, E.A.** (2001)
Induction of rapid atherogenesis by perivascular carotid collar placement in apolipoprotein E-deficient and low-density lipoprotein receptor-deficient mice. *Circulation* **103**:1164-70

**Trucco, A. · Polishchuk, R.S. · Martella, O. · Di Pentima, A. · Fusella, A. · Di Giandomenico, D. · San Pietro, E. · Beznoussenko, G.V. · Polishchuk, E.V. · Baldassarre, M. · Buccione, R. · Geerts, W.J.C. · Koster, A.J. · Burger, K.N.J. · Mironov, A.A. · Luini, A.** (2004)
Secretory traffic triggers the formation of tubular continuities across Golgi sub-compartments. *Nature cell biology* **6**:1071-81

**Vasile, E. · Qu-Hong · Dvorak, H.F. · Dvorak, A.M. (1999)**
Caveolae and vesiculo-vacuolar organelles in bovine capillary endothelial cells cultured with VPF/VEGF on floating Matrigel-collagen gels. *The Journal of Histochemistry and Cytochemistry* **47**:159-67

**Verkade, P.(2008)**
Moving EM: the Rapid Transfer System as a new tool for correlative light and electron microscopy and high throughput for high-pressure freezing. *Journal of Microscopy* **230**:317-28

**Verkleij, A.J. · Ververgaert, P.H. · van Deenen, L.L. · Elbers, P.F. (1972)**
Phase transitions of phospholipid bilayers and membranes of Acholeplasma laidlawii B visualized by freeze fracturing electron microscopy. *Biochimica et biophysica acta* **288**:326-32

**Verkleij, A.J. · Zwaal, R.F. · Roelofsen, B., · Comfurius, P. · Kastelijn, D. · van Deenen, L.L. (1973)**
The asymmetric distribution of phospholipids in the human red cell membrane. A combined study using phospholipases and freeze-etch electron microscopy. *Biochimica Et Biophysica Acta* **323**:178-93

**Verkleij, A.J. · Ververgaert, P.H.J.T. (1975)**
The Architecture of Biological and Artificial Membranes as Visualized by Freeze Etching. *Annual Review of Physical Chemistry* **26**:101-122

**Verkleij, A. · van Alphen, L. · Bijvelt, J. · Lugtenberg, B. (1977)**
Architecture of the outer membrane of Escherichia coli K12. II. Freeze fracture morphology of wild type and mutant strains. *Biochimica et biophysica acta* **466**:269-82

**Verkleij, A.J. · Post, J.A. (2000)**
Membrane phospholipid asymmetry and signal transduction. *The Journal of Membrane Biology* **178**:1-10

**Volger, O.L. · Fledderus, J.O. · Kisters, N. · Fontijn, R.D. · Moerland, P.D. · Kuiper, J. · van Berkel, T.J. · Bijnens, A.J.J. · Daemen, M.J.A.P. · Pannekoek, H. · Horrevoets, A.J.G. (2007)**
Distinctive expression of chemokines and transforming growth factor-beta signaling in human arterial endothelium during atherosclerosis. *The American Journal of Pathology* **171**:326-37

**Volkmann, N. (2002)**
A novel three-dimensional variant of the watershed transform for segmentation of electron density maps. *Journal of Structural Biology* **138**:123-9

**Walther, P. · Ziegler, A. (2002)**
Freeze substitution of high-pressure frozen samples: the visibility of biological membranes is improved when the substitution medium contains water. *Journal of Microscopy* **208**:3-10

**Wild, P. · Schraner, E.M. · Adler, H. · Humbel, B.M. (2001)**
Enhanced resolution of membranes in cultured cells by cryoimmobilization and freeze-substitution. *Microscopy Research and Technique* **53**:313-21

**Wilke, K. · Wick, K. · Keil, F.J. · Wittern, K. · Wepf, R. · Biel, S.S. (2008)**
A strategy for correlative microscopy of large skin samples: towards a holistic view of axillary skin complexity. *Experimental Dermatology* **17**:73-81

**Williams, W.P. (1990)**
Cold-induced lipid phase transitions. Philosophical transactions of the Royal Society of London. Series B, *Biological sciences* **326**:555-67; discussion 567-70

**de Winter, D.A.M. · Schneijdenberg, C.T.W.M. · Lebbink, M.N. · Lich, B. · Verkleij, A.J. · Drury, M.R. · Humbel, B.M. (2009)**
Tomography of insulating biological and geological materials using focused ion beam (FIB) sectioning and low-kV BSE imaging. *Journal of Microscopy* **233**:372-83

**Wu, J. · Liu, W. · Sousa, E. · Qiu, Y. · Pittman, D.D. · Maganti, V. · Feldman, J. · Gill, D. · Lu, Z. · Dorner, A.J. · Schaub, R. · Tan, X. (2007)**
Proteomic identification of endothelial proteins isolated in situ from atherosclerotic aorta via systemic perfusion. *Journal of Proteome Research* **6**:4728-36

**Yamada, E. (1955)**
The fine structure of the gall bladder epithelium of the mouse. *The Journal of Biophysical and Biochemical Cytology* **1**:445-58

**Yunghans, W.N. · Keenan, T.W. · Morré, D.J.** (1970)
Isolation of golgi apparatus from rat liver. 3. Lipid and protein composition. *Experimental and molecular pathology* **12**:36-45

**Zambrano, F. · Fleischer, S. · Fleischer, B.** (1975)
Lipid composition of the Golgi apparatus of rat kidney and liver in comparison with other subcellular organelles. *Biochimica Et Biophysica Acta* **380**:357-69

**Zibara, K. · Chignier, E. · Covacho, C. · Poston, R. · Canard, G. · Hardy, P. · McGregor, J.** (2000)
Modulation of expression of endothelial intercellular adhesion molecule-1, platelet-endothelial cell adhesion molecule-1, and vascular cell adhesion molecule-1 in aortic arch lesions of apolipoprotein E-deficient compared with wild-type mice. *Arteriosclerosis, Thrombosis, and Vascular Biology* **20**:2288-96

**Ziese, U. · Kübel, C. · Verkleij, A. · Koster, A.J.** (2002)
Three-dimensional localization of ultrasmall immuno-gold labels by HAADF-STEM tomography. *Journal of Structural Biology* **138**:58-62

# dankwoord

Een promovendus wordt - misschien vreemd genoeg - gedurende zijn AIO-schap niet opgesloten in een kamertje van twee bij twee meter zonder raam. Ook is het niet zo, dat hij gedurende deze periode door de professor verre wordt gehouden van elk sociaal contact dat niet voort vloeit uit de online PubMed databank vol wetenschappelijke artikelen. En hoewel we er natuurlijk over kunnen discussiëren, of een wetenschapper niet een dergelijk kluizenaarsschap na zou moeten streven...ben ik persoonlijk blij dat er meer mensen zijn in mijn leven dan alleen ik (want dan zou ik alleen mezelf nog maar hebben om te vermoeien...en ik kan heel vermoeiend zijn).

Allereerst wil ik mijn paranimfen noemen...het was voor mij al vrij snel duidelijk wie dat zouden worden. Ten eerste heb je niet zo veel keuze als niemand je aardig vindt, en je dus geen vrienden hebt. En ten tweede hebben jullie mij allebei op een cruciaal punt van mijn leven geholpen bij een keuze die me gebracht heeft waar ik nu ben. Toen ik op HAVO zat was ik van plan om scheikunde te gaan studeren...maar toen ik naar het VWO ging begon ik het zo oninteressant te vinden, dat ik ontdekte dat dit niet het vak was waar ik me de rest van mijn leven mee bezig wilde houden (en dat is maar goed ook, want als iemand mij nu vraagt om de molariteit van iets te berekenen...laat ik het zo zeggen: nee). Het was een lang gesprek met Jeschaël die mij uiteindelijk naar de biologie heeft gebracht; een keuze waar ik geen spijt van heb. Maar...tijdens mijn studie heb ik de moleculaire (en in mindere mate de cellulaire) richting van de (medische) biologie genomen, en hoewel ik de theorie interessant vind en begrijp, heb ik net te weinig fantasie om in het praktische deel staande te blijven. Bandjes op een gel, epjes waar DNA in zou zitten...het zal allemaal wel, maar persoonlijk zag ik er de lol niet van in. Op dat ogenblik liet Jean-Luca (en ja, ik spel je naam gewoon zoals het hoort) mij een andere tak van de sport zien...eentje waar je werkelijk ziet waar je naar kijkt: (3D) elektronen microscopie. En dit is een wetenschap waar ik me wel thuis voel. En ik kan oprecht zeggen, dat ik blij ben dat deze wereld van de cel mij in de wetenschap gehouden heeft. Daarom Jes, JL, ik hef mijn glas naar jullie op...en mocht iemand op het lab zich afvragen waarom ze met mij opgescheept zitten (jullie weten wie jullie zijn), dan kunnen ze nu jullie aanwijzen als de schuldigen.

Natuurlijk kan ik mijn promotor niet vergeten: Arie, het was me een eer om AIO bij jou te zijn, en ik hoop oprecht, dat ik er iets van heb weten te leren...de tijd zal het vertellen. Bram (Koster), jij hebt samen met Arie me de mogelijkheid gegeven om als AIO bij Cellular Architecture & Dynamics (al hadden we toen nog niet die naam) te werken...en als er iets is, dat ik geleerd heb van onze samenwerking, dan is het wel dat biologen en natuurkundigen niet altijd naar dezelfde wereld lijken te kijken. En ook dat is goed om als onderzoeker te ontdekken.

Omdat ik niet alleen zat in dat kamertje van twee bij twee, zonder raam...Frits, ik denk niet, dat ik bij een beter iemand op de kamer kon worden gezet dan bij jou. Het is een algemeen erkent wetenschappelijk feit, dat EMmers aangespoord moeten worden om deel te nemen aan de sociale activiteiten (zoals de lunch, of vreemd genoeg zelfs de werkbesprekingen). En ik ben blij, dat jij deze moeilijke taak naar mij toe op je hebt genomen...of je succesvol was zul je aan de anderen moeten vragen. Marco, hoewel de start een beetje moeilijk was tussen ons, moet ik zeggen, dat je gewoon op onze kamer thuis hoort. Heiner, unsere technischen Diskussionen haben mir immer amüsiert...ob sie nun unsere Arbeit betrafen oder Monkey Island. Als laatste kamergenoot wil ik jou nog noemen, Liesbeth. Met jou heb ik in de laatste jaren toch wel een speciale band opgebouwd. Of het nu was omdat dat we samen naar het winkeltje liepen om lunch te kopen (voedsel is voor mij altijd al een heel goed bindmiddel geweest) of dat we gewoon in werkelijkheid allebei enigszins gestoord zijn (zelf neig ik naar het eten, maar dit is een goede tweede) weet ik niet, maar het was een plezier bij je op de kamer te zitten (of jij op mijn kamer...ik was er eerst).

Ik zou mijn werk niet hebben kunnen verrichten zonder de hulp van mensen die meer van computers weten dan waar de aan/uit-knop zit. Bob, het hele project had niet bestaan zonder jouw betrokkenheid bij de benodigde infrastructuur, Maurice (Bouwhuis), Bart, voor mijn werk was de kracht van de SARA supercomputer facilities essentieel, en jullie hebben er voor gezorgd, dat ik die krach tot mijn beschikking had...natuurlijk heb ik wel nog steeds de droom een keer PacMan of Tetris op de supercomputer te spelen. Theo, ook jou wil ik hier noemen, omdat zonder jou enthousiasme en inzet de link naar SARA ook nooit tot stand had kunnen komen.

Natuurlijk wil ik - naast mijn eerder genoemde kamergenoten - ook alle andere EMmers bedanken. Ik ga jullie niet allemaal opnoemen (jullie kunnen je naam terug vinden op www.electronmicroscopy.nl), maar er zijn een paar mensen die ik toch even apart wil vermelden. Allereerst Willie, wij hebben een verschillende manier van kijken en doen. Maar jij hebt bij verschillende delen van mijn onderzoek een waardevolle inbreng gehad. Ik kan - en wil - niet anders dan je daar voor bedanken. Nuria, onze samenwerking bij hoofdstuk 6 van dit proefschrift heeft me een aantal dingen geleerd...een daarvan is, dat het heel goed mogelijk is, dat jij misschien wel een van de beste tomografisten bent. Het was een plezier om met je samen te werken, en ik denk dat ons werk aan caveolae mijn beste artikel in dit proefschrift is...maar meer Spaans dan *Ardilla* kan ik nog steeds niet spreken. Wally, iedereen die weet wat 'as you wish' betekend heeft sowieso een streepje voor bij mij. Jan Andries, je hebt de (soms vermoeiende) taak op je genomen om - in de laatste fase van mijn AIO-schap - de functie van co-promotor op je te nemen, en ik denk, dat dit tot een succesvol proefschrift heeft geleid. Iedereen moet maar uitvechten of jij in deze groep van namen thuis hoort, maar voor mij ben je onderdeel van de imaging groep en hoor je bij de EMmers. Mensen die het hier niet mee eens zijn kunnen natuurlijk altijd een zwarte marker lenen om deze zinnen weg te strepen...dat is aan hun.

Voor die mensen die net - onterecht - Jan Andries bij de EMmers weg hebben gekrast heb ik een ander sprongetje nodig om van de West-vleugel naar de Noord-vleugel te komen, dus Mireille, dat ben jij. Een paar jaar terug nog een EMmer, nu onze expert Arabische talen voor het geval dat we een keer gesponsord gaan worden door een rijke olie-sjeik (met een heel harem aan lama's). Natuurlijk wil ik ook een aantal andere mensen noemen van Cellular Architecture & Dynamics die niet in de West-vleugel zaten. Edward, Bart, Smiriti, Erik, en Jarno, ik noem jullie hier echt niet alleen omdat ik bang ben voor de presentatie die jullie anders voor mij gaan maken. Echt waar, dat heeft er absoluut niets mee te maken. Dus ehm...jongens, meisje, die presentatie is echt nergens voor nodig hoor.

Maurice (Stassen), Bram (Maasen)...tja, jullie werken niet meer bij CAD, maar onze vele gesprekken waren me een waar genoegen, en misschien moeten we deze zomer weer eens afspreken om ergens iets te gaan drinken.

David, Maarten, sommige tradities moeten in ere gehouden worden, en de woensdag pizza-dag is daar een van. Op het ogenblik dat ik dit schrijf is het mijn buurt om te betalen...hopelijk heb ik daar het geld nog voor nadat dit boekje gedrukt is, want het zou toch jammer zijn als promoties een eind zouden maken aan deze traditie. David, ik ken je als sinds het begin van mijn studie biologie in Nijmegen, en toen ik hoorde dat jij op de vijfde verdieping van het Kruyt-gebouw een baan had gevonden was ik wel een beetje overrompeld door het toeval, omdat mijn tweede stage zich grotendeels op dezelfde verdieping heeft afgespeeld. Toch was het meer dan een beetje prettig dat een van m'n vrienden bij dezelfde vakgroep zat als waar ook ik zou komen te werken.

Ja, en met David kom ik terecht bij mijn studie-vrienden. Allereerst Edinio, mocht de wereld ooit overspoeld worden door zombies of vampieren dan weet ik zeker dat jij ons allemaal in de stijl van Blade zult

beschermen met een katana en een shotgun...tenminste, daar zijn David en ik volledig van overtuigd. Dus mochten we ooit overspoeld worden door zombies of vampieren, dan mag je ons niet teleurstellen. Tanja, Natasja, Natascha, helaas hebben jullie tegenwoordig nooit meer tijd voor sociale dingen (in ieder geval niet als jullie helemaal naar Utrecht moeten komen), maar het was een genoegen om met jullie samen te studeren (en de pauzes, en treinreis door te brengen). Natasja, ik wil je nog even apart feliciteren voor de stap die je met Mark gaat nemen.

Roy, wie had kunnen weten dat pepermunt een basis kan zijn van een vriendschap? - Stefan, ik zal dit jaar proberen je verjaardag eens een keer wel te onthouden...dat is een bijzonder grote uitdaging, maar we zullen zien of het lukt (het wordt trouwens weer eens tijd voor poolen en kebab...David, Edinio, dat geldt ook voor jullie).

Jean-Luca, computer Theo, ik wil jullie toch nog een tweede keer noemen, omdat ik onze vele discussies over het geloof toch erg op prijs heb gesteld. En al is het dan zo, dat we verschillende spectra van het Christelijk geloof bewandelen, was dat nu juist wat de discussies zo levendig hield. Jean-Luca, in jouw dankwoord schreef je indertijd: "ik ben nog niet zover dat ik je gelijk ga geven!"...ik kan maar één ding zeggen: "ach...dat komt nog wel."

Maar discussie, kritische studie, en geloof zijn voor mij altijd een eenheid geweest, en dat is een van de dingen waarvoor ik blij ben dat ik in de kerk van Arnhem de ruimte heb gekregen (misschien niet door iedereen...maar die mensen bedank ik hier dan ook niet). Dit is toch altijd een plek geweest waar het duidelijk is, dat je het niet (altijd) me elkaar eens hoeft te zijn - ook niet over zulke basale, wereldbeeldvormende dingen - om toch respect voor elkaar te kunnen hebben. Ik denk niet dat er binnen de wetenschappelijke wereld ook maar één plek te vinden is waar kritische meningen, en discussie zo'n basale rol spelen...En dat is iets waar ik jullie absoluut dankbaar voor ben.

Natuurlijk wil ik ook mijn familie hier bedanken. Gerhard, Angelique, dankzij jullie opvoeding ben ik de mens die ik ben...dus voor klachten kunnen mensen ook bij jullie terecht. Maar uiteindelijk ben ik trots op wie ik ben, en wie ik dankzij jullie ben geworden. Thirza, soms is het lastig als we allebei het laatste woord willen hebben, maar het levert wel leuke discussies en ideeën op, dat is zeker. Jeschaël, je bent meer dan enkel een broer voor me...en op z'n minst weet ik hoe je allebei onze namen correct moet spellen. En er zijn maar weinig mensen op deze planeet die dat kunnen zeggen. Bram (Nekkers), Jes, ooit komt tDMoT echt nog af...geloof me...ooit.

Natuurlijk heb ik ook nog familie die iets recenter familie is geworden, maar die ik ook niet wil vergeten: Yelina, als je heimwee hebt moet je maar gewoon naar Jes kijken en je voorstellen hoe hij er uit ziet met een snor...sprekend José Marti (ok, misschien niet echt...maar toch). En je bent weer helemaal in Cuba. Oh ja...als je niet op schiet ga ik onze wedstrijd winnen! - Floor, Marian, Jeroen, ik ben blij, dat ik me bij jullie welkom kan voelen.

Sandra, dat brengt me bij jou. Sandra, ik zou een paar pagina's vol kunnen schrijven in dit dankwoord enkel gewijd aan jou...maar uiteindelijk is het samen te vatten in één woord: "Thee?"

Natuurlijk wil ik ook alle katten niet vergeten: Peper, Bollie, Moes, Jakje, en namens Sandra, Mogje, Carrie, Teun, Toby, Kasja en Jiska...en zeker niet op de minste plaats (namens ons allebei): Tommie.

Dan rest mij enkel nog één te bedanken: יהוה.

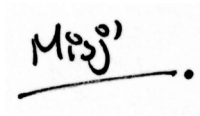

Misjaël N. Lebbink is geboren op 18 december 1977 om 6:24 te Arnhem...en zijn broer en zus kunnen getuigen, dat dat veel te vroeg was. Na de eerste jaren van zijn leven - waar hij uitzonderlijk veel interessante dingen heeft geleerd waar hij tot op de dag van vandaag nog veel aan heeft (inclusief lopen en praten natuurlijk) - is hij in Arnhem naar de middelbare school (het CLA) gegaan. Hier kreeg hij een MAVO advies, waar niemand zich iets van aangetrokken heeft, en heeft hij uiteindelijk zijn HAVO-diploma met een extra vak heeft gehaald. Vervolgens heeft hij ook nog zonder al te veel moeite zijn VWO afgerond (zodra je Frans kunt laten vallen wordt de wereld een stuk aangenamer moet ik zeggen) en is hij in 1997 naar de Katholieke Universiteit Nijmegen (nu Radboud Universiteit) gegaan om daar biologie te studeren, waarbij hij zich zou specialiseren in (medisch) biologische richtingen van cel- en moleculaire-biologie. Tijdens zijn studie heeft hij twee wetenschappelijke stages gelopen: de eerste in het Moleculaire Dierfysiologie-lab van prof. dr. Gerard Martens in Nijmegen, waar zijn onderzoek zich richtte zich op de ontwikkeling van plaques bij diabetes type II, en de tweede in het cellbiologie lab (Cell Microscopy Center) van prof. dr. Hans Geuze in Utrecht, waar hij voor het eerst van dichtbij in aanraking kwam met drie-dimensionale elektronen microscopie, en keek naar de structuur en organisatie van multilaminaire lysosomen in antigen presenterende cellen. Dit laatste onderzoek heeft hem in contact gebracht met prof. dr. Arie Verkleij en de vakgroep Cellular Architecture & Dynamics, waar hij zijn promotie-onderzoek startte aan de visualisatie van cellulaire structuren in het kader van het IOP project *electron tomography, an indispensable step between Genomics and Cellular dynamics (IGE03012)*, welke uiteindelijk zou leiden tot het boekje dat u hier in handen heeft.

Murk, J.L.A.N. · Lebbink, M.N. · Humbel, B.M. · Geerts, W.J.C. · Griffith, J.M. · Langenberg, D.M.L. · Verreck, F.A.W. · Verkleij, A.J. · Koster, A.J. · Geuze, H.J. · Kleijmeer, M.J. (2004)
3-D Structure of multilaminar lysosomes in antigen presenting cells reveals trapping of MHC II on the internal membranes. *Traffic* **5**:936-45

Lebbink, M.N. · Geerts, W.J.C. · van der Krift, T.P. · Bouwhuis, M. · Hertzberger, L.O. · Verkleij, A.J. · Koster, A.J. (2007)
Template matching as a tool for annotation of tomograms of stained biological structures. *Journal of structural biology* **158**:327-35

Yakushevska, A.E. · Lebbink, M.N. · Geerts, W.J.C. · Spek, L. · van Donselaar, E.G. · Jansen, K.A. · Humbel, B.M. · Post, J.A. · Verkleij, A.J. · Koster, A.J. (2007)
STEM tomography in cell biology. *Journal of structural biology* **159**:381-91

de Winter, D.A.M. · Schneijdenberg, C.T.W.M. · Lebbink, M.N. · Lich, B. · Verkleij, A.J. · Drury, M.R. · Humbel, B.M. (2009)
Tomography of insulating biological and geological materials using focused ion beam (FIB) sectioning and low-kV BSE imaging. *Journal of Microscopy* **233**:372-83

Lebbink, M.N. · van Donselaar, E.G. · Humbel, B.M. · Hertzberger, L.O. · Post, J.A. · Verkleij, A.J. (2009)
Induced membrane domains as visualized by electron tomography and template matching. *Journal of Structural Biology*. **166**:156-61

Hekking, L.H.P. · Lebbink, M.N. · de Winter, D.A.M. · Schneijdenberg, C.T.W.M. · Brand C.M. · Verkleij, A.J. · Post, J.A.
FIB-SEM: an in-depth study of atherosclerotic tissue. *submitted*

Lebbink, M.N. · Jiménez, N. · Vocking, K. · Hekking, L.H.P. · Verkleij, A.J. · Post, J.A.
Template matching reveals a spiral coating on the membranes of the caveolar system in endothelial cells. *in preparation*

Years from now, when you talk of this, and you will, be kind. Deborah Kerr to John Kerr. Tea and Sympathy , MGM 1958.

*Remington Steele*